UNIVERSITY OF CALGARY

Borehole Geophysical Methods for Near-Surface Characterization

by

Soo-Kyung Miong

A THESIS

SUBMITTED TO THE FACULTY OF GRADUATE STUDIES

IN PARTIAL FULFILMENT OF THE REQUIREMENTS FOR THE

DEGREE OF MASTER OF SCIENCE

DEPARTMENT OF GEOSCIENCE

CALGARY, ALBERTA

SEPTEMBER 2008

ABSTRACT

This thesis examines the application of VSP techniques for near-surface characterization. First analyzed are multi-offset VSP datasets which were acquired in August 2006, using geophone and hydrophone sensors over depths of 4 m to 40 m, in the West Castle River area of southern Alberta. The hydrophone VSP shows superior data quality compared to the geophone VSP. P-wave velocity models obtained from the VSP analysis give velocities that range from 670 m/s in the unconsolidated near-surface material to 3500 m/s in the deeper competent shales. The position of the seismic reflectors in the VSPCDP stack of the data agree reasonably well with position of the lithologic boundaries identified by the driller; especially the tops of three water-bearing gravel layers that are resolved by the VSPCDP stack.

A more extensive set of field tests was carried out in July 2007, near Priddis, Alberta. Shallow well logs, VSP, and 2D and 3D seismic reflection survey data were collected at the geophysical test site near the Rothney Astrophysical Observatory. According to well log analyses, a major fracture and four porous sandstone units were identified at depths of 28 m, 39 m, 50 m, 61 m, and 120 m with porosities ranging from 0.34 to 0.58. The respective P-wave velocities of clean sandstone and shale zones are 3200 m/s and 2300 m/s after calibrating the sonic velocities using the VSP data. Five zones of interest are interpreted in the VSP images and they correlate with the 3D and 2D seismic results; especially the fracture zone at 28 m — the largest source of groundwater in the test well — and the thick, possibly water-bearing, sandstone unit at 60 m. The correlation of the various borehole and seismic data demonstrate the efficacy of these techniques for near-surface characterization.

ACKNOWLEDGEMENTS

I would like to thank a number of people who have contributed immensely in completing this project.

- First of all, I thank my thesis supervisor, Dr. Robert R. Stewart for suggesting this thesis topic and his guidance throughout the project. He really opened my eyes in the geophysical world: From data acquisition to interpretation, he patiently explained the fundamentals involved in each step of the geophysical project and encouraged me to apply these concepts to characterize near-surface features. I thank Rob for being such an awesome supervisor and for being a great role model.

- I thank Joe Wong for his input in this thesis. He was always there to answer questions and eager to help in any way he can. All of the VSP data discussed in this thesis were acquired with help of Joe. With that note, I also thank Eric Gallant, and 2006 and 2007 undergraduate geophysics students for their assistance in acquiring much of the shallow VSP data.

- I thank Dr. Don Lawton and Dr. Larry Bentley for their valuable discussions on the geological and hydrological characteristics near Priddis.

- Hanxing Lu, Gabriela Suarez, and Khaled Al Dulaijan provided 3D and 2D surface seismic data that are correlated with the VSP data. I strongly believe that their input added more depth to the scope of this thesis.

- I thank Kevin Hall and Rolf Maier for providing all the technical support I needed to complete this project.

- I am truly grateful for so many special individuals I've met throughout my graduate study. Occasional lunches, dinners, pot-luck party, and activities that I shared with them made my graduate study more enjoyable and memorable.

- Last and most of all, I thank Jay, my husband, and my family for their endless love and support throughout the study. They always encouraged me to implement positive attitudes towards everything that life throws at me. I really couldn't have done it without them.

DEDICATION

To Jay, Mom, Dad, Kyung-Sook, Jin-Sub, Roh and Terry

TABLE OF CONTENTS

LIST OF FIGURES

LIST OF TABLES

LIST OF ABBREVIATIONS

AGC: Automatic gain control

CDP: Common depth point

f-k: frequency-wavenumber

GPR: Ground penetrating radar

GR: Gamma ray

NMO: Normal-moveout

P-wave: Primary-wave

RES: Resistivity

RMS: Root-mean-square

S-wave: Shear-wave

SP: Spontaneous potential

Sv: Shear-wave propagating in the vertical plane

VSP: Vertical seismic profiling

3-C: Three-component

2D: Two-dimensional

3D: Three-dimensional

Chapter 1: Introduction

1.1 Application of vertical seismic profiling (VSP) and the research objectives

Vertical seismic profiling provides insight into the nature of seismic wave propagation in the earth and can give estimates of rock properties such as interval velocities, impedance, anisotropy, and attenuation near the borehole (Sheriff and Geldart, 1995). VSP can also provide processing and interpretive assistance in the analysis of surface seismic data (Stewart, 2001). A VSP survey has the advantage of placing receivers below the overburden layer so that seismic reception is not complicated by the often attenuative and heterogeneous near-surface: Receivers are also close to the targets of interest. With VSP geometry, upgoing and downgoing seismic events can be identified at different points along their propagation path in both depth and time. Many wave propagation effects can also be observed: multiples (typical noise in VSP data) can be identified and removed; seismic attenuation can be measured by comparing the amplitude spectra of the downgoing wave field at different depth levels; and with offset VSP data, both reflected and transmitted mode-converted S-waves can be observed (Coulombe et al., 1996). VSP data are typically acquired using tools including hydrophones deployed in the borehole or three-component (3-C) geophones clamped to the borehole wall. Excellent overviews and case histories using VSP for subsurface characterization can be found in Coulombe et al. (1996); Stewart (2001); Gulati et al. (2001); and Gulati et al. (2004).

The near-surface can be characterized using various techniques including refraction and reflection surface seismic and ground penetrating radar (GPR). Cardimona et al. (1998) imaged a shallow aquifer using seismic reflection and ground-penetrating radar. Jefferson et al. (1998) monitored changes in soil-moisture content of unconsolidated material by observing variations in seismic attributes of the surface reflection data: higher amplitudes of reflection and refraction amplitudes were obtained under more saturated near-surface conditions. Kim et al. (1994) imaged shallow fracture zones in crystalline rocks existing at depth of 60-100 m using seismic reflection techniques. The shallow-reflection technique has been used in mapping bedrock beneath alluvium in the vicinity of hazardous waste sites, detecting abandoned coal mines, following the top of the saturated zone during a pump test in an alluvial aquifer, and in mapping shallow faults (Miller et al., 1989).

However, the surface seismic reflection method has inherent resolution limitations because seismic energy must propagate through the weathered layer, resulting in attenuation of the desired higher frequencies (Gochioco, 1998). Borehole geophysical methods have not been extensively used for near-surface characterization. Therefore, the objectives of this research were to test whether shallow borehole concepts can be used to overcome the limitations of surface seismic and to employ these techniques to characterize the groundwater resources as well as to better characterize the rock units that make up the aquifer system. If proven useful, the information from borehole analysis could have application to seismic statics, groundwater exploration, and geotechnical projects (building and dam design). The following section provides an outline of this thesis.

1.2 Introduction to the thesis

Various geophysical data were acquired from two survey areas located near West Castle River and Priddis, Alberta. In Chapter 2, VSP data from West Castle River area of southern Alberta are described. The quality of the hydrophone versus geophone is compared. Then, the VSP velocities extracted from two near- and far-offset VSP data are correlated. Some of the hydrophone VSP data is further processed to image prominent reflectors.

In Chapter 3, the hydrogeologic condition, soil properties and water resources of the second survey site near Priddis, Alberta, are investigated. A suite of well-logs and various VSP data were acquired from the same site. Using the VSP data, the sonic log was calibrated. Then, using the calibrated sonic and density logs, a synthetic seismogram was generated. In Chapter 4, processing flows for near- and far-offset VSP are introduced using the various field VSP data acquired from this site.

In Chapter 5, the open- and closed-hole well logs, synthetic seismogram, lithologic description, and processed 2D and 3D high-resolution surface seismics were correlated with the processed VSP data. Interpretation was then made based on the composite display of all geophysical analysis accomplished on this area.

Chapter 6 summarizes the conclusions derived from this research project. Future projects to improve the VSP velocity model and survey design are also suggested.

Water well drilling reports provided by Castle Mountain ski resort management, which were used for assigning seismic boundaries for P-wave velocity calculation, are shown in Appendix A. Principles of processing steps used in the field and synthetic VSP processing are explained in Appendix B.

1.3 Hardware and software used

The entire work presented in this thesis was accomplished using a standard PC connected to the CREWES Project network at the University of Calgary. Synthetic seismograms were generated using *MATLAB* software and the field VSP data processed using *VISTA* software. Ray-tracing required for the traveltime inversion was adapted from *'traceray' MATLAB* code provided from CREWES libraries. In addition, *Microsoft Word, Microsoft PowerPoint* and SnagIt software were used to assemble the text and images for this thesis.

Chapter 2: Hydrophone VSP analysis: Castle Mountain Experiment

2.1 Introduction

Vertical seismic profiling (VSP) is a form of seismic surveying that uses motion-sensing receivers in boreholes. Shots or vibrations are normally initiated on the surface, near the wellhead or offset laterally from it. The resultant vibrations are recorded at different depths within the borehole using special detectors either suspended in the well or clamped to the borehole wall. In VSP surveys, the detectors can be located in the immediate vicinity of the target zone, meaning the overall length of the reflected ray-path is shortened, reducing the effects of attenuation as well as the dimensions of the Fresnel zone (Sheriff and Geldart, 1995). Moreover, multiple detectors can be deployed in the borehole at the same time making the data acquisition more efficient.

VSP data are typically acquired using tools containing three-component (3-C) geophones clamped to the borehole wall. Coupling the geophone to the borehole wall is important for recording the true earth motion, but the procedure can be complicated and time-consuming (Gulati et al., 2001). A less expensive and rapid VSP acquisition technique is to use a hydrophone string. Hydrophones are pressure-sensitive detectors that can be suspended in a fluid-filled borehole without requiring clamping. They are relatively easy to deploy and a large number of them can be used simultaneously.

Previous experiments that evaluated the effectiveness of vertical hydrophone arrays on a land survey were carried out by Marzetta et al. (1988), Krohn and Chen (1992), and Gulati et al. (2001). To test the viability of this shallow VSP concept, both geophone and hydrophone VSP surveys were conducted at Castle Mountain, southern Alberta,. Therefore the objectives to be addressed in this chapter were to 1) compare the quality of geophone and hydrophone VSP data; 2) compute VSP velocities from two hydrophone VSP data; 3) design appropriate processing flows for field near-offset VSP data; and 4) interpret the processed VSP.

2.2 Location of the survey site

In August 2006, shallow hydrophone VSP data were collected from two wells (called the Lodge and Duplex wells) at the base of the Castle Mountain ski resort, which is located near the West Castle River of southern Alberta (Figure 2.1*a* and *b*). The area, in the front range of the Rocky Mountains, is highly structural and prospective for hydrocarbons. The British Columbia-Alberta border forms the western perimeter of the survey site, around townships 4-5, range 3-4, west of the 5th meridian.

The Lodge and Duplex wells are about 200 m apart and their depths are 43 m and 32 m, respectively (Figure 2.2). According to the water well drilling report provided by the Castle Mountain resort management, the survey sites are dominantly composed of unconsolidated sand and gravels, interbedded by water-bearing gravel (Figure 2.2). Competent shale is encountered in the Lodge well at depths greater than 40 m. The respective static water levels in these wells are about 6.6 m and 5 m below the surface. The wells are cased with steel pipe with their bottom sections screened for inflowing groundwater. The inner diameters are 20.3 cm for the casing, and 17.8 cm for the screen.

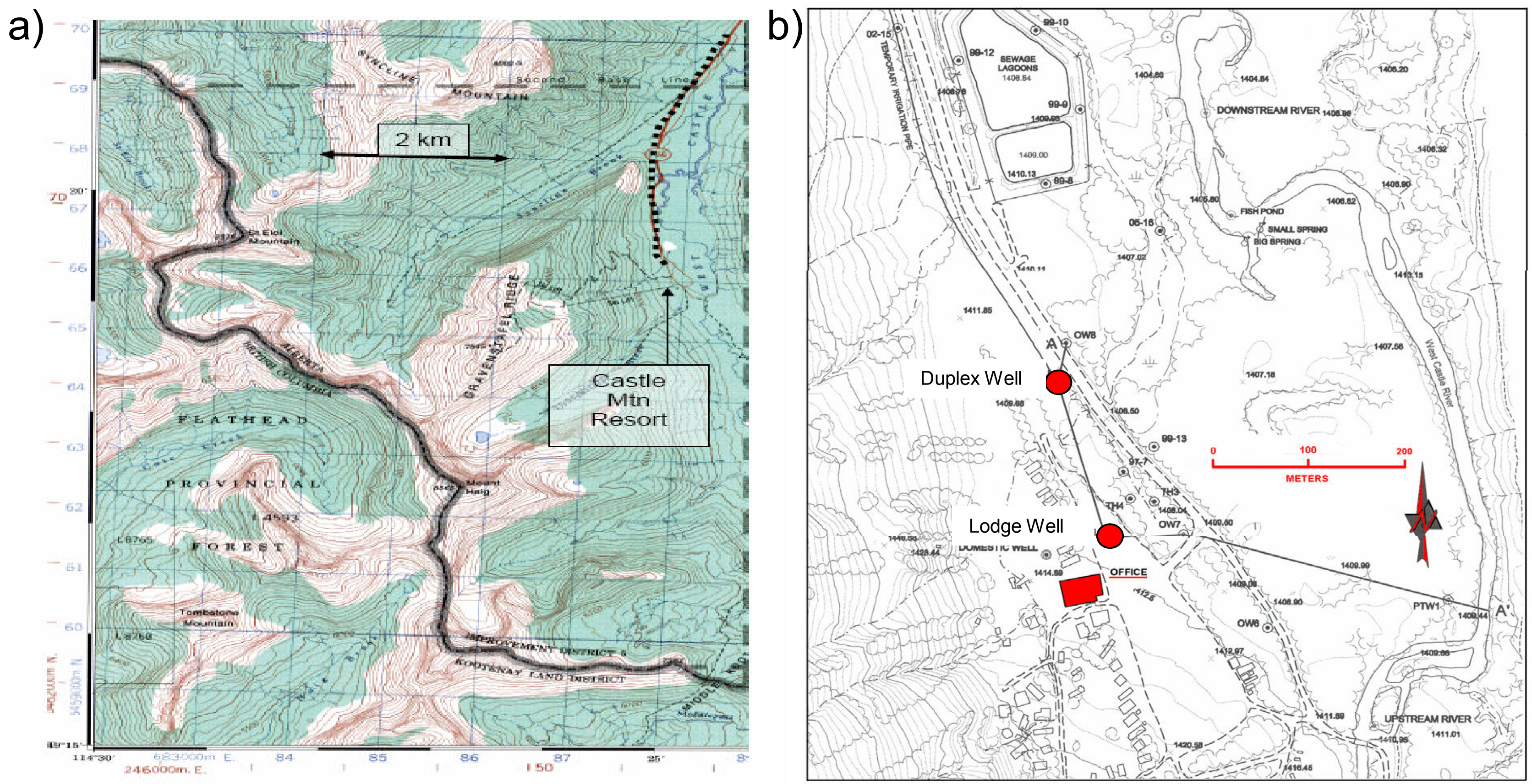

Figure 2.1. a) Location of the survey site ("Castle Mtn Resort") in Alberta. b) Location of Lodge and Duplex wells (shown by red circles) at the base of the Castle Mountain Resort, in southern Alberta.

2.3 Geophone and hydrophone acquisition

The seismic source for our surveys was a 7.4 kg sledgehammer striking a spiked aluminum cylinder set firmly on the surface at various offset distances (15 m offset for the Lodge well survey and 20 m for the Duplex well survey as shown in Figure 2.2) from the wellhead. The first detector was an eight-element hydrophone array placed below the water level and the receiver increment in the survey was 0.25 m for the Lodge survey and 1 m for the Duplex survey (Figure 2.2 *b* and *d*). The clamping 3-C geophones were also deployed in these wells with 1 m receiver increment. The total acquisition times to acquire the hydrophone and geophone VSP data were about 40 min and 1 hour, respectively (Figure 2.3); clamping the geophone to the borehole to achieve good coupling between the well and the sonde was more time consuming. Recording was done with a Geometrics R60 seismograph using a high-cut filter of 500 Hz, a sampling interval of 0.5 ms, and trace lengths of 512 ms. The raw hydrophone shot gathers in Figure 2.2 b) and d) were acquired from the two survey sites at source offsets of 15 m and 20 m. The wells impose difficult seismic conditions since the uncemented well casing and formation are poorly coupled and overburden layers (i.e. high-loss unconsolidated sand and gravel) are present.

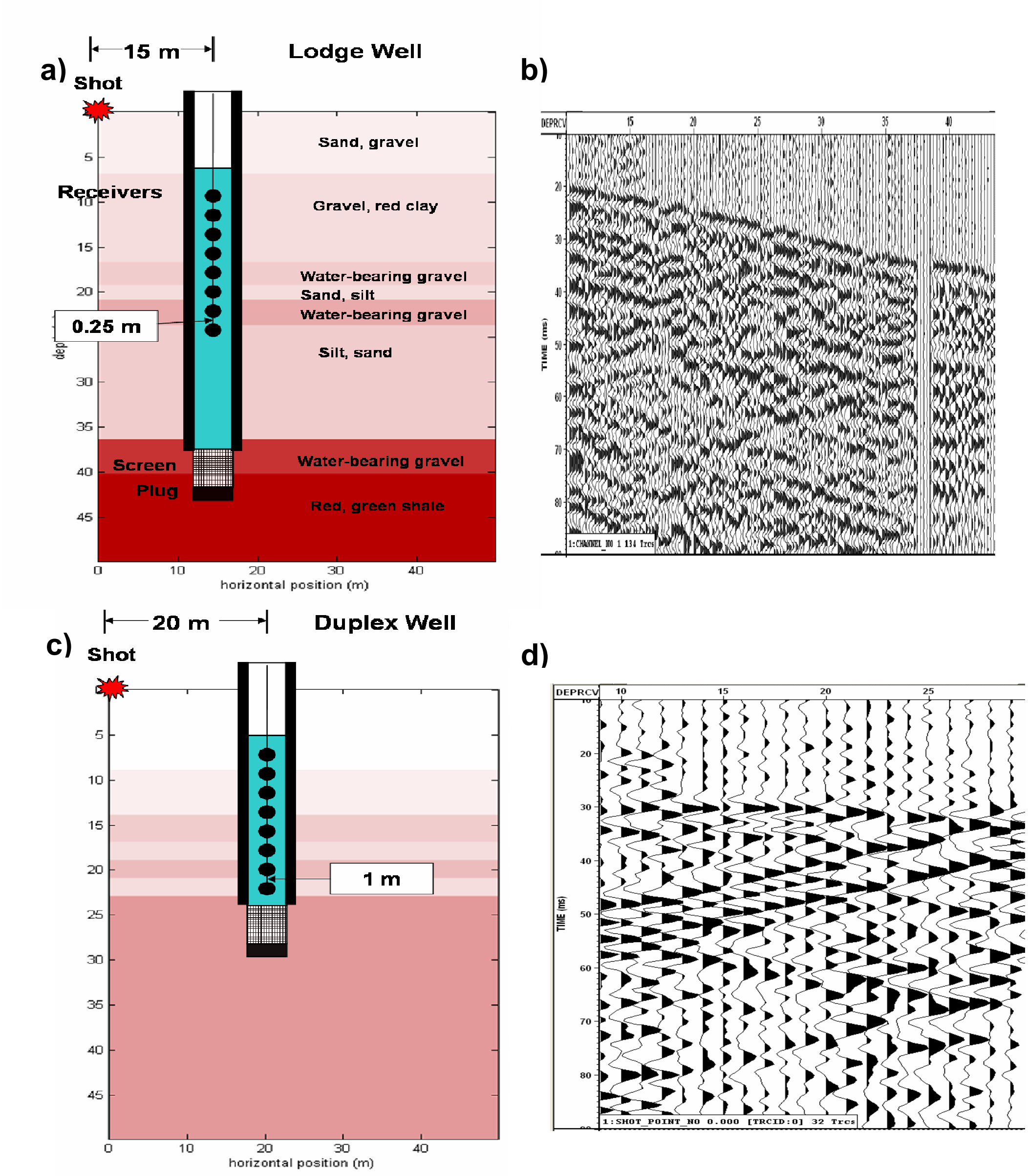

Figure 2.2. a) The hydrophone VSP geometry at the Lodge well, b) the 15-m offset Lodge VSP data, c) The hydrophone VSP geometry at the Duplex well, and d) the 20-m offset Duplex VSP data.

2.4 Comparison between the geophone and hydrophone data

The raw VSP shot-gathers recorded at a 15-m offset by 3-C geophone and hydrophone are shown in Figure 2.3. Compared to hydrophone VSPs, the 3-C geophone VSPs have lower frequencies, a lower signal-to-noise ratio, and show less trace-to-trace consistency (Wong et al., 2006). Picking first-breaks from the geophone data is difficult and hodogram analysis is required to pick the first-arrival times mostly accurately. Also each component of the geophone data is severely contaminated by other low-frequency noise (possibly ground roll). The quality of the geophone VSPs may have been adversely affected by poor coupling between the geophone and the test wells: The fairly long aluminum lever arms (~50 cm) on the geophones may not have effectively clamped to the test wells, which have a diameter of ~20 cm. Also the casing and well screen were not grouted. Although the upper cased section of the well was sealed by forcing a bentonite mixture down the outside of the casing, it is unclear if lower portions of the casing are fully bonded. Thus, it is thought that there is a poor coupling between the borehole wall and the geophone where permeable zones of coarse gravel occur, as is the case in the screened (unsealed) sections of the wells (Wong et al., 2006).

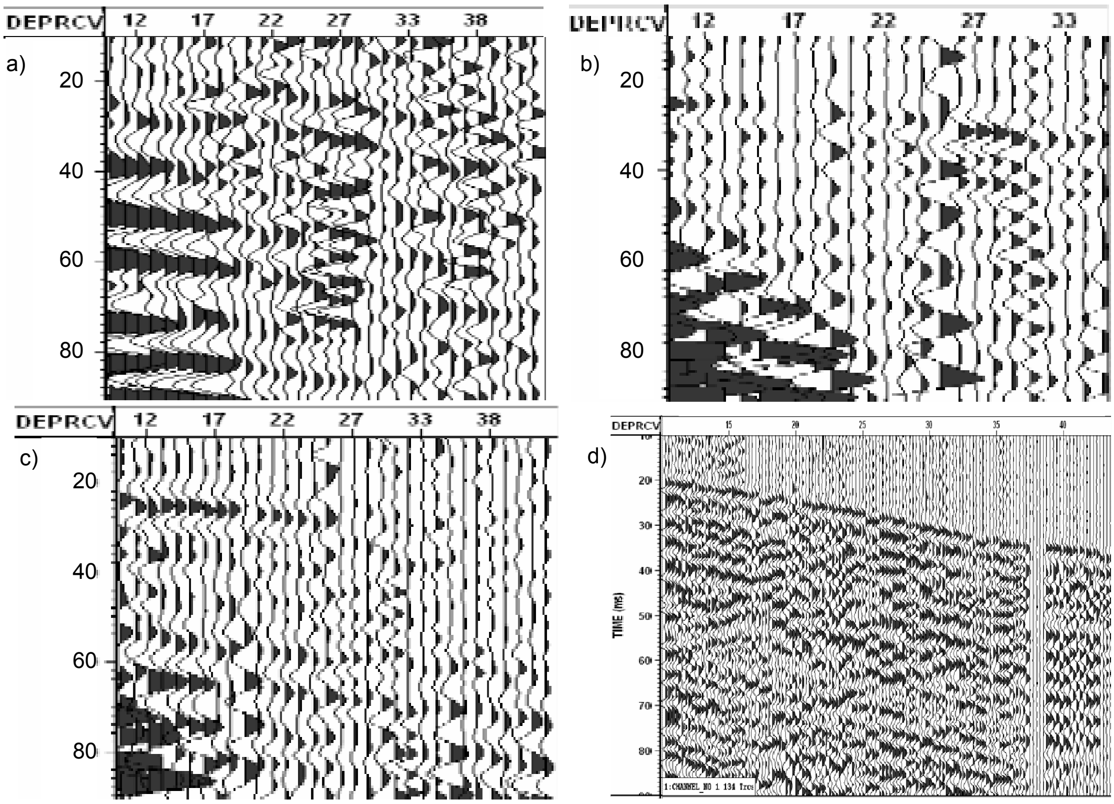

Figure 2.3. 15 m-offset VSP data recorded by the a) vertical, b) radial, and c) transverse components of a 3C-geophone, and d) hydrophone.

2.5 Velocity calculation for 15-m and 30-m offset VSP data

The P-wave velocity model is developed by modelling the observed first-arrival times using a refracting boundaries ray-tracing program (Wong et al., 2006). In the velocity model, depths of the seismic boundaries are assigned according to the lithology description outlined in the water well drilling report (see Appendix A). P-velocities are derived by tracing rays through a layered earth model and matching the observed first-arrival times while honoring Snell's Law on the boundaries between the velocity layers. The constant velocity value for each layer is modified until its estimated first-arrival time matches the observed first-arrival time with an error less than 1 ms (Figure 2.4).

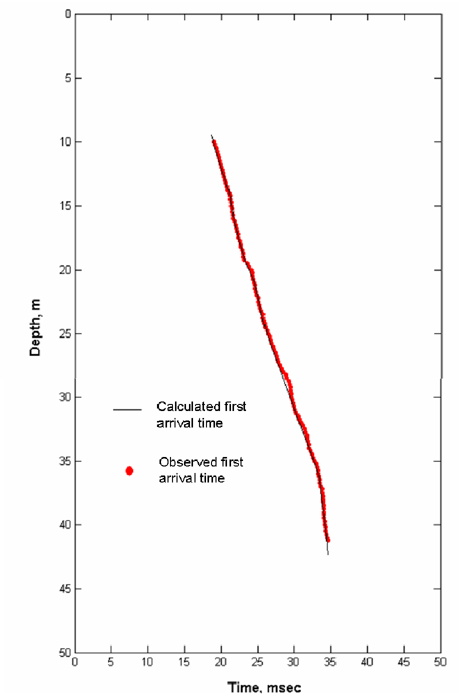

Figure 2.4: Comparison of the observed and calculated first-arrival times of the 15-m offset hydrophone VSP data for the Lodge Well.

Figure 2.5 shows the final velocity models for the Lodge and Duplex well sites. The velocity values at the Lodge well range from 910 m/s in the sand and gravel top layer to 3500 m/s in the competent shale layer. The Duplex velocity model has a similar range of velocity values except at the very top layer which is defined to be a very loosely unconsolidated sand fill (~670 m/s). The thickness and the sequence of subsequent high and low-velocity layers at the Duplex well correlate well with the Lodge well velocity values. For example, the low velocity sand and silt layer that is interbedded between the water-bearing gravels at the Lodge well site (depth of ~20 m) is also represented in the Duplex survey site (depth of ~22 m).

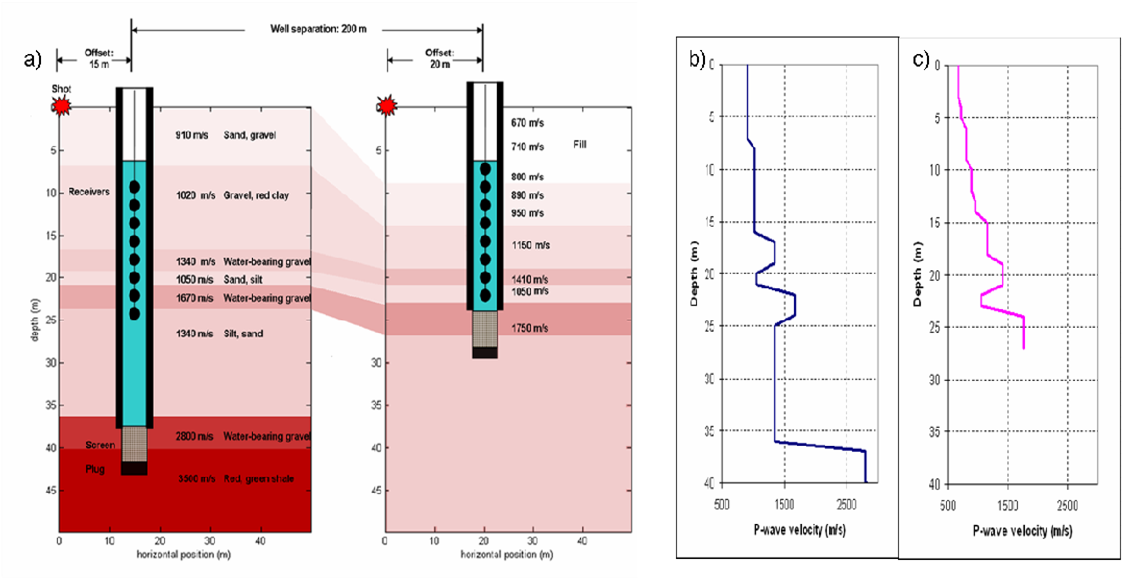

Figure 2.5. a) Configuration of the Lodge well (left) and Duplex well (right). P-wave velocity-depth curve for b) the Lodge well, and c) the Duplex well. The lithology and thicknesses were provided by a water-well drilling report. The P-wave velocities were estimated by ray-tracing.

2.6 Synthetic modelling

Using these two vertically varying velocity models, an acoustic finite-difference modelling algorithm was used to generate synthetic seismograms. This method was chosen since finite-difference modelling with an accurate free-surface representation can give insight into the relationship of the conventional reflections caused by the waves affected by boundaries, like first breaks and ground roll (Manning and Margrave, 2002). The finite-difference modelling algorithm was implemented in MATLAB as part of CREWES program package (Margrave, 2007). Figure 2.6 b) and d) show the synthetic VSP data generated using the two velocity models in Figure 2.5 with the correct offset-and-receiver assignment.

As shown in Figure 2.6 a) and b), the primary upgoing wavefields predicted by the synthetic data are also present in the raw Lodge well VSP data in similar positions (see red arrows). Tube waves are a common type of noise in VSP field data (Hardage, 1981) that can be generated when the surface waves from the source come in contact with the borehole fluids and become guided waves. The field VSP from the Lodge well data doesn't seem to suffer from tube waves. On the other hand, characteristics of tube waves with an apparent velocity of about 1150 m/s are observed from the field Duplex VSP data (Figure 2.6 *c*, highlighted zones). However, the synthetic VSP data for the Duplex well (Figure 2.6 *d*) suggests that there may be a velocity layer that has a comparable velocity to the tube waves. Considering that the first seven metres of the subsurface of the Duplex well survey area was a very loose, unconsolidated sand fill (with velocities as low as 670 m/s), which imposes difficult conditions for seismic wave propagation, both Lodge and Duplex hydrophone VSP data show surprisingly good first-arrivals.

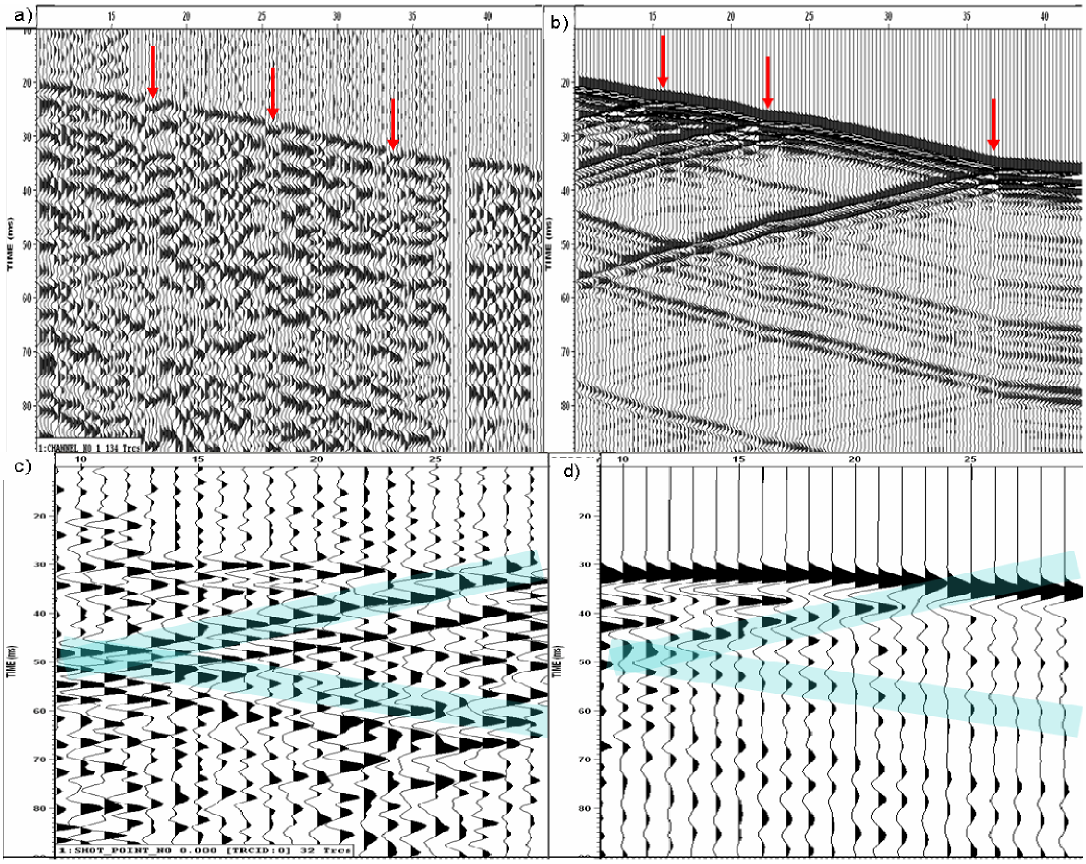

Figure 2.6. a) A shot gather of raw hydrophone VSP data from a 15-m source offset (Lodge well); b) Synthetic VSP generated from the Lodge velocity model (Figure 2.5a); c) A shot gather of raw hydrophone VSP data from a 20 m source offset (Duplex well); d) Synthetic VSP generated from the Duplex velocity model in Figure 2.5b). The x and y-axis represent depth of the receiver and field recording time in milli-seconds, respectively. The red arrows in a) and b) represent credible reflections from high velocity layers. Blue highlights indicated possible downgoing and reflected P-waves that may have comparable velocity as the tube-waves.

2.7 Processing flow testing using near-offset VSP

The raw Lodge Well VSP data was processed to observe whether the seismic reflectors can be imaged. The processing flow was revised and tested using the synthetic VSP data. No rotation is required with the hydrophone data and the effect of static corrections was negligible since there is a very small elevation difference between the shot point and the reference datum.

A flow chart for processing the near-surface hydrophone VSP data is provided in Figure 2.7. From the raw data, dead traces are discarded. First-arrival times are then picked from the raw data. Due to shot strength variation and near-surface geology changes, traces from raw field records may have wildly varying total power levels: Thus, each trace in the flattened raw data is equalized. After these pre-processing steps, the downgoing wavefields are enhanced using a 15-point-median velocity filter and these wavefields are subtracted from the pre-processed data to obtain residual upgoing waves plus any remnants of downgoing waves and tube waves (Figure 2.8). To evaluate the success of each processing step, these processing steps were applied on the synthetic seismogram.

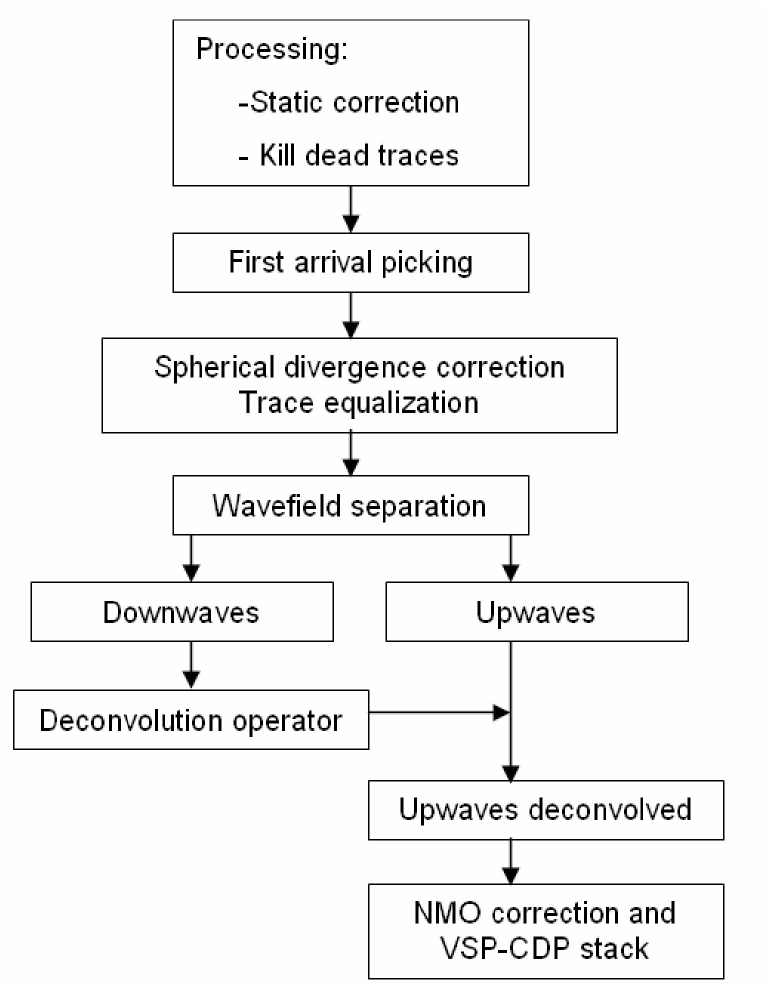

Figure 2.7. Shallow near-offset hydrophone VSP processing flow.

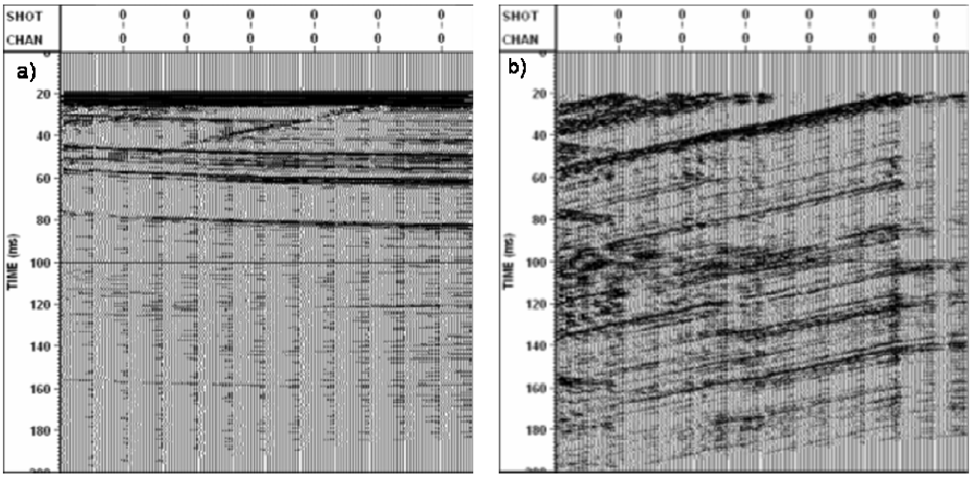

Figure 2.8. Wavefield separation using 15-point-median filter: a) Enhanced downgoing-P-wavefields and b) Upgoing P-wavefields. Not that both shot gathers are flattened to their first-arrival times.

The extracted upgoing wavefields were deconvolved (with the downgoing wave) to sharpen reflections and to suppress multiples. The selection of a good deconvolution operator window size is based on its ability to collapse the downgoing energy into a single, band-limited spike. The deconvolution design window was 150 ms with an operator length of 20 ms and 1% pre-whitening. Using the designed deconvolution operator, the upgoing and downgoing wavefields were deconvolved (for quality control). After the deconvolution, normal-moveout effect was corrected using the the root-mean-square velocity derived from the P-wave velocity model in Figure 2.5 a) (see Figure 2.9).

These images were then mapped into their true horizontal reflection point by a VSPCDP (common-depth-point) mapping procedure with a bin size of 10 cm (Figure 2.10) using VISTA processing software. As shown in Figure 2.10, the multiples, especially after 65 ms, are effectively removed from the upgoing wavefields and only the primary reflectors are imaged in the final CDP stack. Using the same deconvolution operator, a VSPCDP stack of the real Lodge well VSP data is generated (Figure 2.11 *b*). For a comparison, the synthetic VSPCDP stack (Figure 2.10) is plotted beside the real stack. The step-by-step processing flow and its application on the field VSP data are extensively explained in Chapter 4.

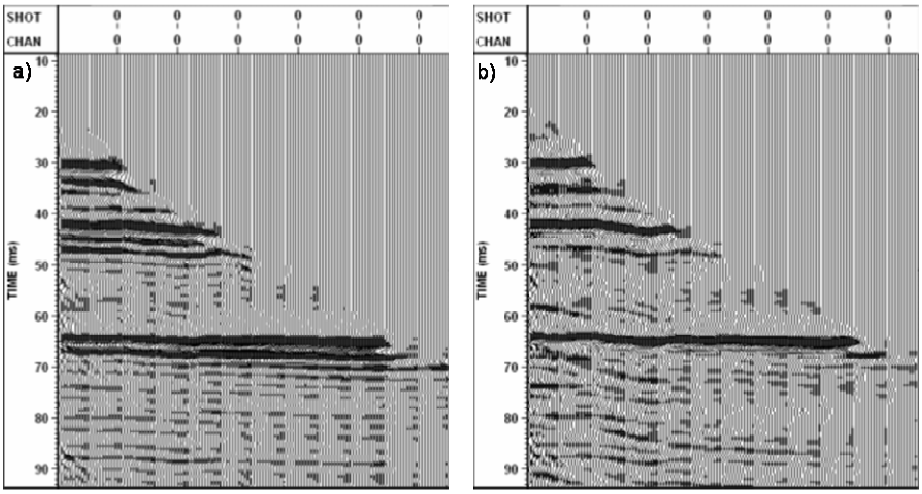

Figure 2.9. Normal-moveout corrected synthetic Lodge VSP data: a) before deconvolution; b) after deconvolution.

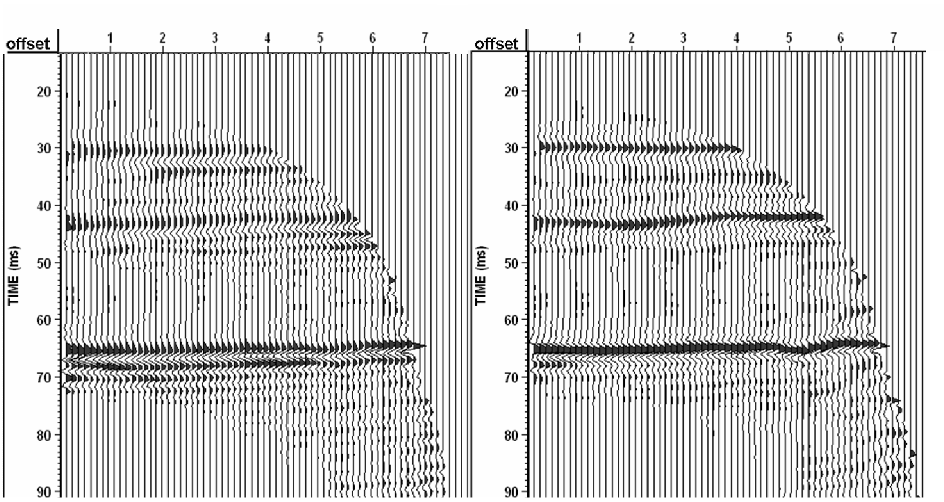

Figure 2.10. VSPCDP stack of synthetic Lodge VSP data: a) before deconvolution; b) after deconvolution.

2.8 Processed near-offset VSP and its interpretation

The velocity model obtained from ray-tracing is converted into two-way traveltime (TWT) and plotted beside the field VSPCDP map to observe whether the seismic boundaries in the velocity model are resolved. The positions of the seismic boundaries in the P-wave velocity model match reasonably well with the horizontal reflection events in the field CDP map. As indicated by the dotted line in Figure 2.11, the three seismic boundaries (at 28 ms, 43 ms and 65 ms) that are associated with the three water-bearing gravel layers are resolved along with other major reflectors. The slight disagreement of the reflector depths may be a result of an inaccurate assignment of the velocity layer’s thickness which was solely dependent on the water well drilling report. Also errors in velocity estimation using the ray-tracing method may have contributed to the displacement of the reflectors. The discontinuation of reflector toward the far-offset (> 3 m) may be due to the remnant of downgoing or tube waves interfering with the upgoing wavefields.

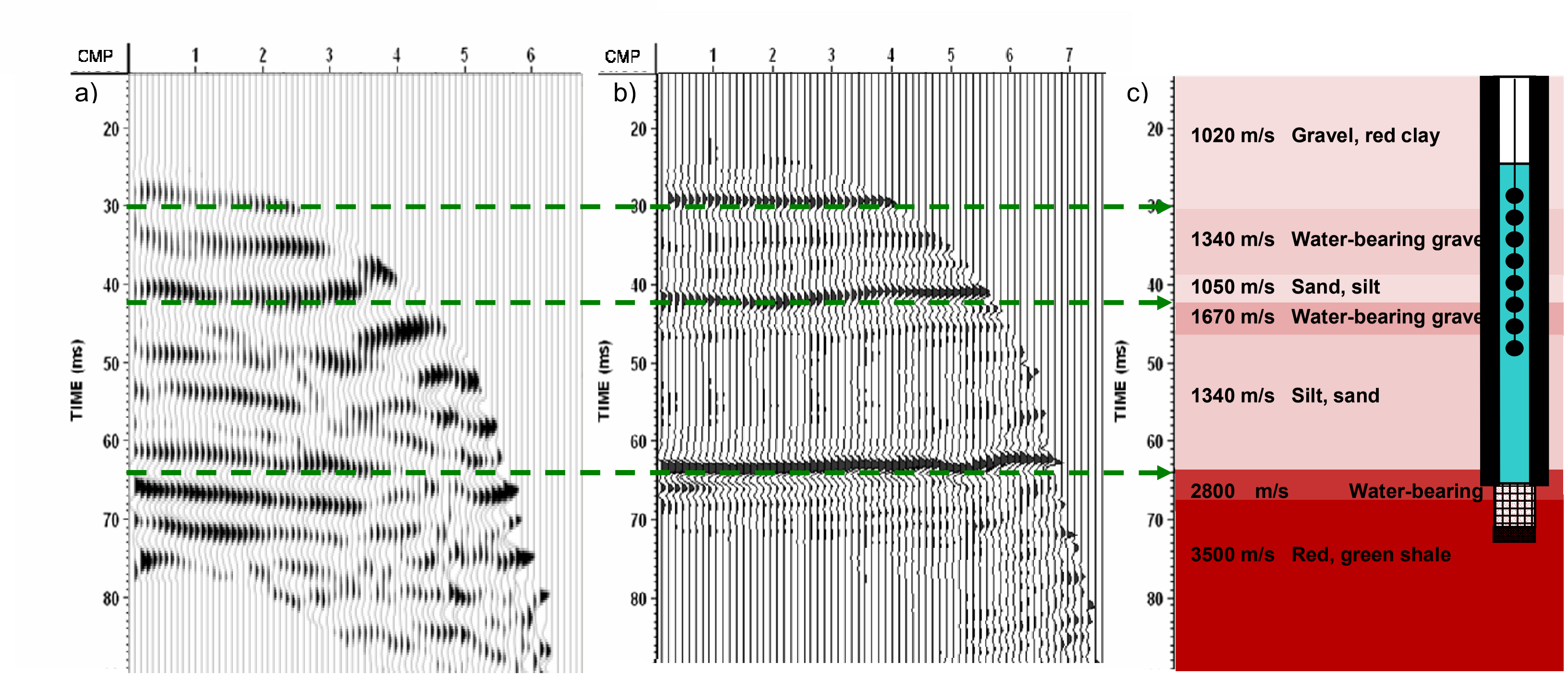

Figure 2.11. VSPCDP map results of deconvolved a) 15-m offset VSP field data and b) synthetic data, and c) P-wave velocity model for the Lodge well in two-way traveltimes.

2.9 Conclusion

Various shallow, multi-offset VSP datasets were acquired in the West Castle River area of southern Alberta, using both geophone and hydrophone. These VSP data were rapidly and inexpensively collected and the hydrophone VSP show superior data quality compared to the geophone VSP. A P-wave velocity model, obtained by traveltime inversion, indicates velocities ranging from 670 m/s in the unconsolidated fills to 3500 m/s in the deeper competent shales. The two velocity models estimated for the Lodge and Duplex wells correlate quite well.

A synthetic VSP seismogram, generated based on the P-wave velocity model, showed reflections that resembled the positions and characteristics of the reflections observed in the field VSP data. The synthetic seismogram was used as a guide for evaluating processing flow for the near-offset hydrophone VSP data. The two-way traveltimes of the seismic reflectors in the VSPCDP stack of the observed VSP data agree reasonably well with positions of the seismic reflector as suggested by the velocity model; especially the tops of the three water-bearing gravel layers (32 ms, 42 ms and 65 ms in two-way-traveltime) that are resolved by the VSPCDP stack. The velocity information and imaging quality of the hydrophone VSP data provide considerable promise for the technique's use in near-surface characterization (e.g., for groundwater exploration) and statics determination for related seismic processing.

Chapter 3: 3C-VSP analysis: Priddis Experiment

3.1 Introduction

Shallow VSP and well logs were acquired from a site at the Rothney Astrophysical Observatory near Priddis, Alberta, about 30 km southwest of the University of Calgary (Figure 3.1). The survey area overlies the Paskapoo Formation, which is the largest single source of groundwater in the Canadian Prairies (Grasby, 2006). The objectives of this survey were to further test whether borehole analysis can be used to help near-surface imaging and whether these techniques could also be used to characterize groundwater resources. In this chapter, the soil properties and hydrogeologic conditions in the Paskapoo Formation the survey area are investigated. Also, the quality of well logs and VSP data acquired from the test site are discussed. In Chapter 4, processing flows for the acquired near- and far-offset VSP data are introduced. In Chapter 5, the well-logs, surface seismics, and VSP data are assembled for interpretation.

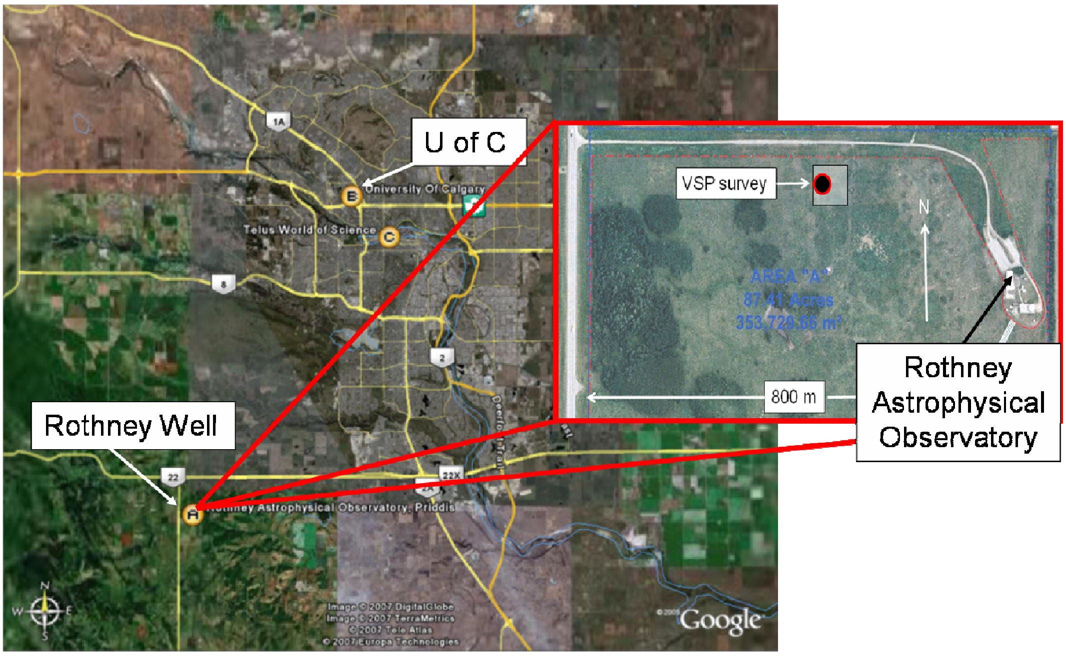

Figure 3.1: Location of the test well near Priddis, Alberta.

3.1.1 Rothney test well

In mid-August, 2007, a 137-m test well was drilled at Priddis for the research purposes of CREWES and the University of Calgary's undergraduate geophysics field school. Aaron Water Well Drilling Company of Dewinton, Alberta, drilled the test well using an air-rotary rig. The open-hole diameter of the test well was 156 mm. The well was completed by inserting steel casing to a depth of 5.5 m with a projection of 0.61 m above ground level. To prevent long-term collapse of the well, a quarter-inch-thick (6.35 mm), 4.0-inch (102 mm) PVC casing was inserted to a depth of 127 m. There was a one-day delay between the drilling and the insertion of the PVC casing, so that open-hole geophysical logging could be done. During this delay, rock detritus washed out of fracture zones fell to the well bottom and caused the loss of 10 m of well depth. Because the well was not intended to produce water for domestic or commercial use, there is no well screen, and the PVC casing is closed off at the bottom and not perforated (Wong et al., 2008). Logging and VSP analysis results from the well will be discussed later in this chapter.

3.2 Geology and hydrogeology of the survey site

The survey site is located at the eastern edge of the Rocky Mountain foothills overlying a structure called a “triangle zone” (Lawton et al., 1994). The area typically consists of a few metres of unconsolidated sediment, mostly tills, glaciolacustrine deposits and alluvium that overlay sandstone and shale of the Tertiary Paskapoo Formation (Figure 3.2). Bedrock consists of fine- to medium-grained fluvial sandstone and shale of Paleocene age. The stratigraphy of the unconsolidated deposits is complex and sometimes unpredictable, by virtue of the complexity of the mainly glacial environments that produced them (Osborn and Rajewicz, 1998). As mentioned previously, the Paskapoo Formation is the largest single source of groundwater in the Canadian Prairies with over 100,000 wells out of 600,000 wells in Canadian Prairies (Grasby, 2006).

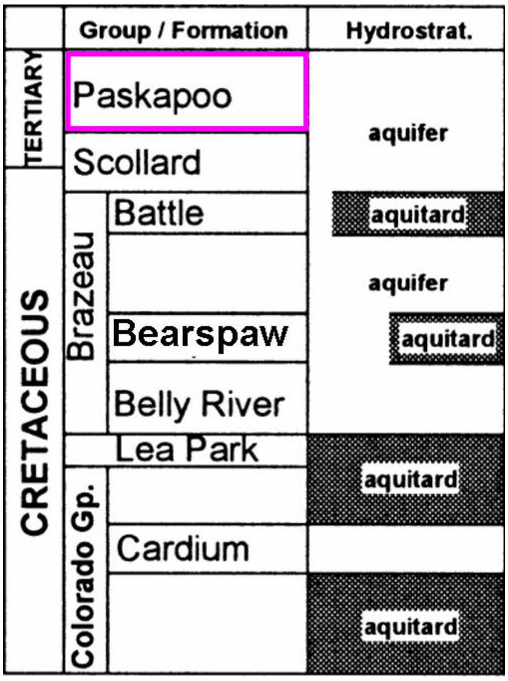

Figure 3.2: Stratigraphic sequence of Paskapoo Formation in Central Alberta (from Osborn and Rajewicz, 1998).

3.2.1 Structural geology at the survey site

Figure 3.3 shows a plan view of the geology of the Alberta Basin (Jerzykiewicz, 1997). Geological cross-sections near the survey site are indicated by the blue arrow. The term 'triangle zone' was introduced by Gordy et al. (1977) to describe structures found along the eastern margin of the Rocky Mountain thrust and fold belt (Figure 3.4). Eastward-dipping Upper Cretaceous and Tertiary strata are juxtaposed against westward dipping, thrusted rocks of Paleozoic to Tertiary age, forming two sides of a triangle. Triangle zones in the Rocky Mountain Foothills have since been discussed by Jones (1982), Teal (1983), McMechan (1985), Price (1986), and Charlesworth et al. (1987).

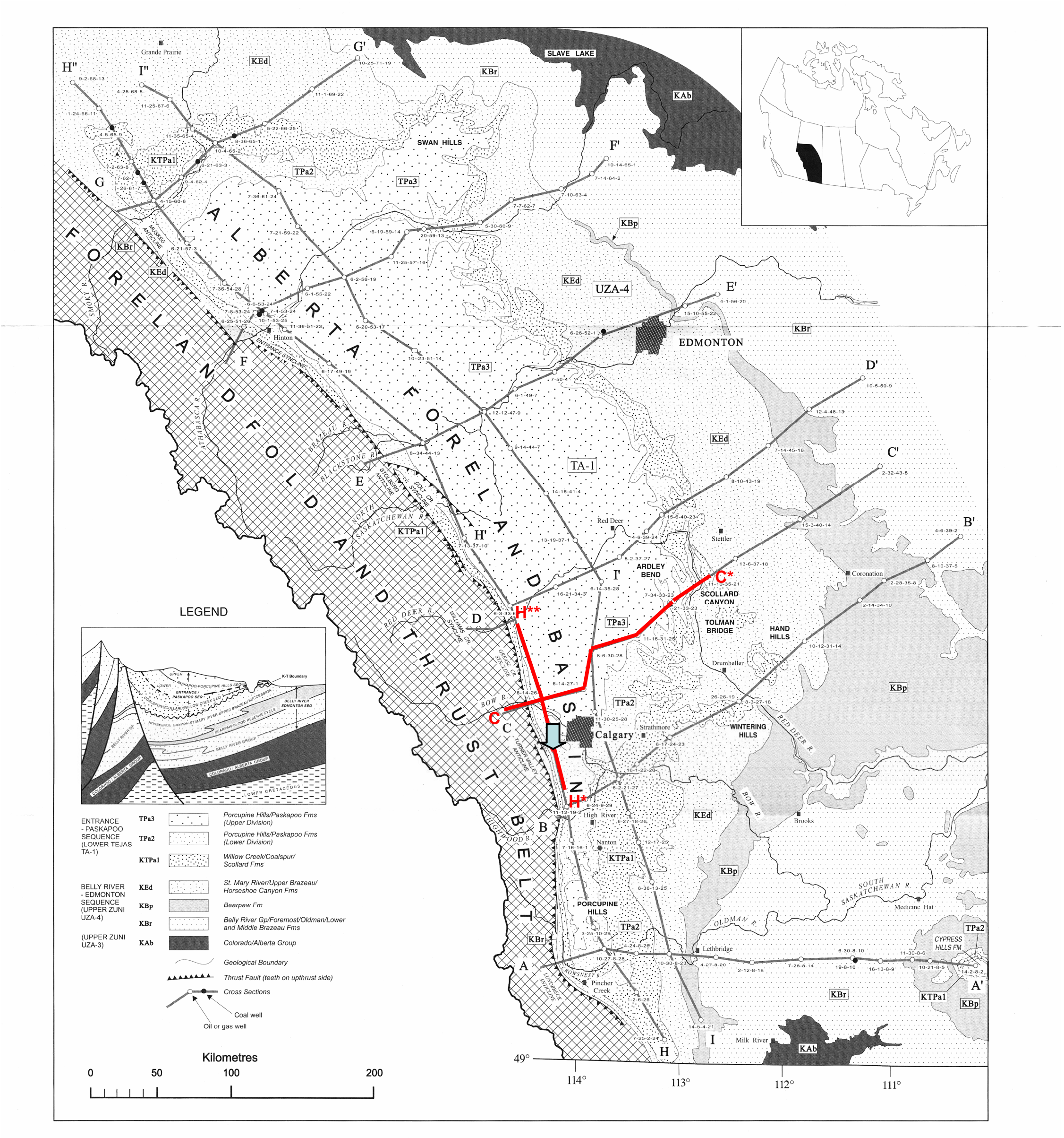

Figure 3.3: Geological map of the Alberta Basin. The survey location is indicated by the blue arrow. Geological cross-section for profiles C-C* and H*-H** are provided in Figure 3.4 and Figure 3.5. (Jerzykiewicz, 1997).

a)

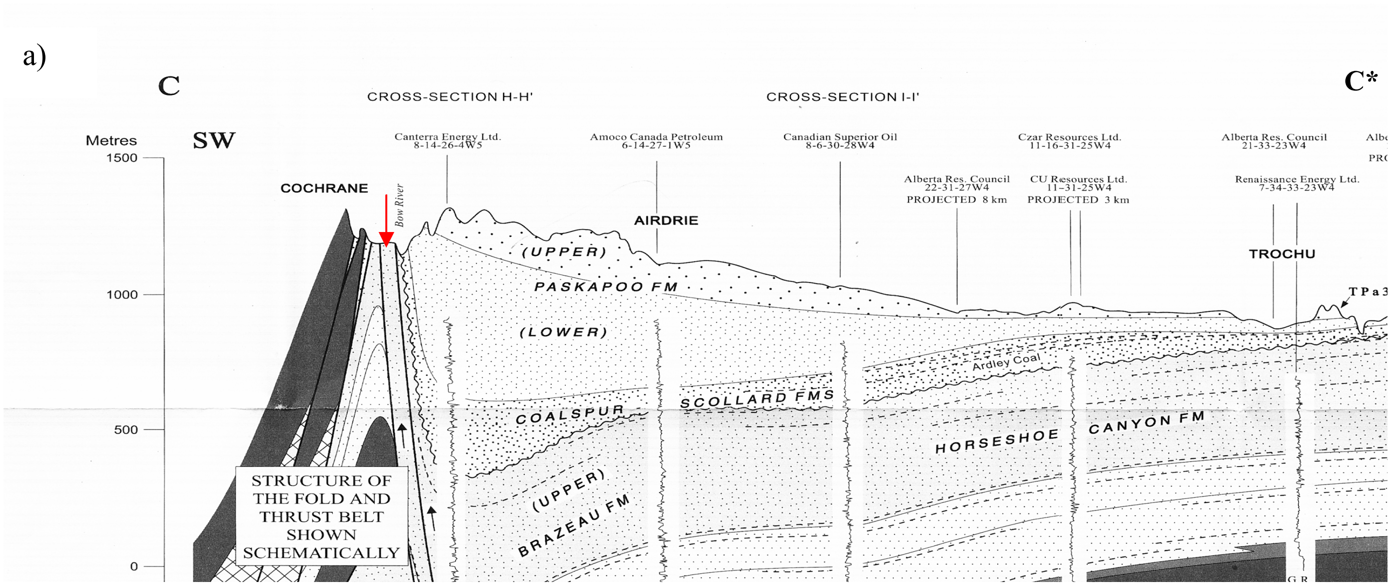

b)

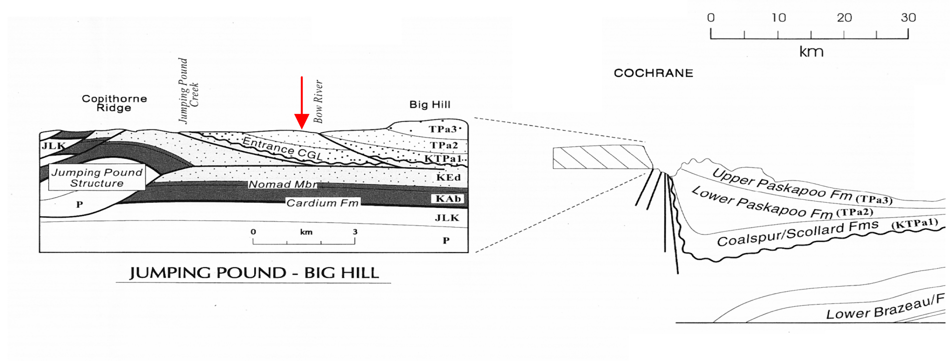

Figure 3.4: a) Geological cross-section of the Alberta Basin (C-C* on Figure 3.3). b) Supplementary to cross-section C-C*, sketches of stratigraphic and structural relations in the deformed belt of the triangle zone near the Jumping Pound area (Jerzykiewicz, 1997). The red arrows indicate the location of the survey area.

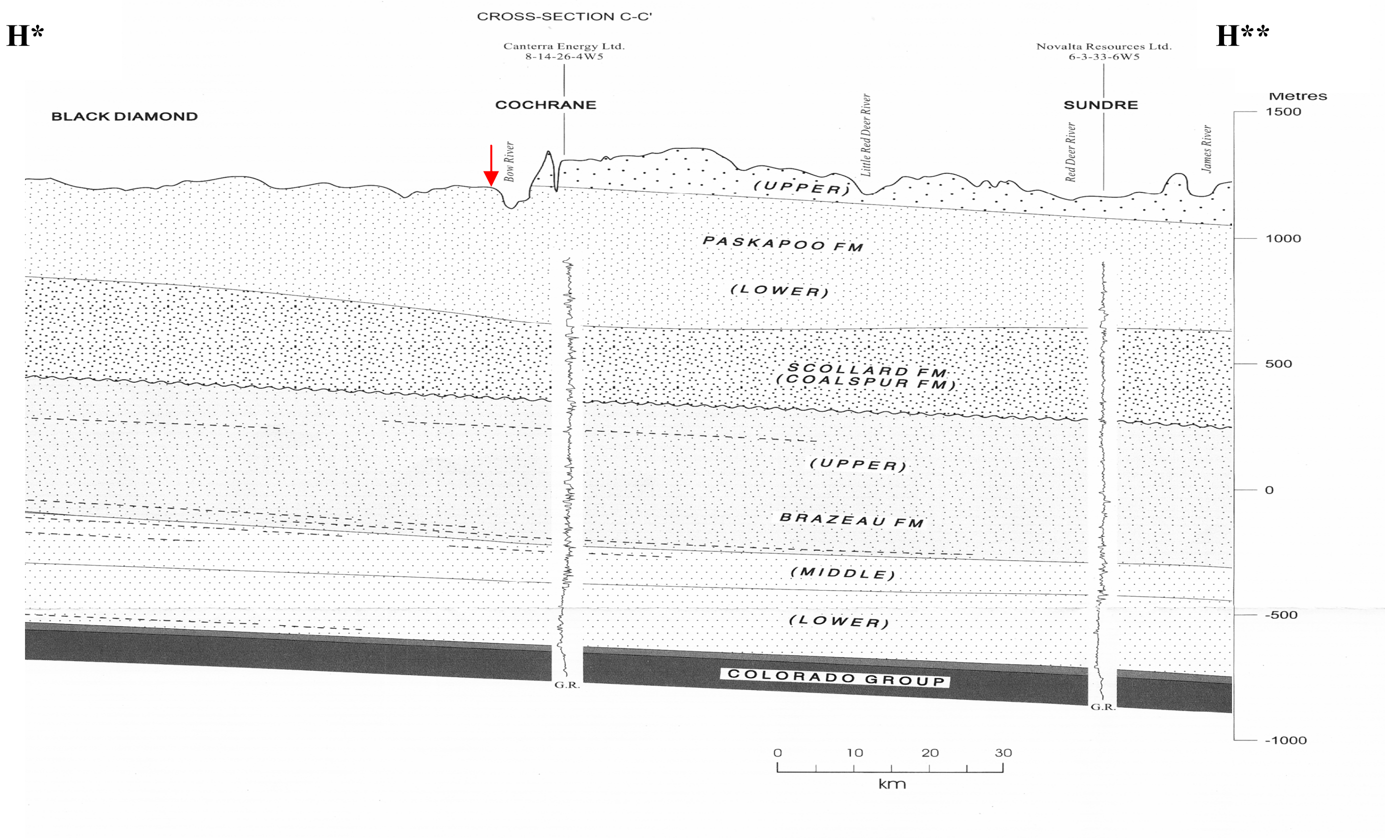

Figure 3.5: Geological cross-section parallel to the axis of the Alberta Basin (H*-H** on Figure 3.3) (Jerzykiewicz, 1997). The red arrow indicates the location of the survey area.

3.2.2 Soil properties

The sediments overlying the Paskapoo Formation are classified as Quaternary deposits of glacial and glaciolacustrine origin. Moran (1986) describes the material as pebble loam till, silts and sands. The thickness of the till normally ranges from 2 m to 30 m. According to the soil description shown in Table 3.1, it is reasonable to assume that the Paskapoo Formation bedrock near the Rothney well is identified from the depths below ~4 m (Al Dulaijan and Stewart, 2007).

Osborn and Rajewicz (1998) describe the Paskapoo Formation as a grey to greenish grey, thick-bedded, calcareous, cherty sandstone; grey and green siltstone and mudstone; and minor conglomerates, thin limestone, coal and tuff beds of non–marine origin. This formation is believed to have been deposited on the floodplain east of the foothills. This formation generally thickens from north-east to south-west in Alberta (Figure 3.4) and near the Priddis area, it may extend to a thickness of 500 m (Grasby et al., 2007, see Figure 3.5).

The Paskapoo Formation is often given the misnomer ‘sandstone’ due to the appearance of sand channels in outcrop. Hamblin (2004) suggests that the Formation is mudstone dominated with a series of sand channels that can form isolated aquifer units (see Figure 3.6 *a* and *b*). The characteristic channel sandstones range up to 15 m, but are typically 5-10 m thick. Sand channels are lenticular and pinch out laterally over short distances (100-150 m or more) (Figure 3.6 *c*). However, basal sand units can develop laterally to form more extensive sheet sands. These sandstone permeabilities are typically very low (average 10^{-14} m^2) with the exception of basal coarse-grained sand units (~10^{-12} m^2).The small amount of measured paleocurrent data suggests a general north-eastward trend, which might indicate that aquifer units within the Paskapoo have greater continuity along that orientation (Hamblin, 2004). Coarse sand and high-porosity sand channels can form locally productive aquifer units.

The fine-grained mudstone or sandy siltstone form intervals several to several tens of metres thick between the major sandstone horizons (Jerzykiewicz, 1997) and likely act as effective aquitards except where connected through fractured systems. Figure 3.7 a) shows an example of fracture system that could develop at shallow depths of Paskapoo Formation. Grasby et al. (2007) suggest that there is a strong relationship between the fracture density and the bed thickness of sand channels (Figure 3.7 *b*). In their study, the thinner the sand channel, the higher the density of fractures was observed. This behaviour is observed because fractures are more easily produced at the boundary between a thinner sand channel and mudstone than within the thick sand channel unit itself.

Table 3.1: Soil descriptions from Rothney well drill cuttings (Al Dulaijan and Stewart, 2007).

Depth (m)	Sample Description
0-4.0	**70% Till, sand, pebble:** Transparent, translucent in part, very fine to medium, sub-angular to sub-rounded, moderately sorted, very loose. **30% Clay**: Tan to brown, friable, and calcareous.
4.0-18.0	**100% Sandstone:** Mainly translucent, transparent and white in part, very fine to coarse, angular to sub-rounded, moderately sorted, moderately compacted, and low porosity.
18.0-22.0	**100% Shale**: Gray, blocky, sub-fissile in part, moderately indurated, and highly calcareous.
22-23.2	**80% Sandstone:** Transparent, tan, very fine to medium, angular, moderately sorted, well compacted with calcareous cement in part, and low porosity. **20% Shale**: Gray, blocky to sub-blocky, and well-indurated.

23.2-23.8	**100% Shale**: Gray, blocky, well indurated, and calcareous.
23.8-28.3	**100 % Siltstone:** light gray, tan in part, blocky, moderately indurated, slightly calcareous.
28.3-31.1	**100 % Siltstone:** light gray, tan in part, blocky, moderately to well indurated, calcareous.

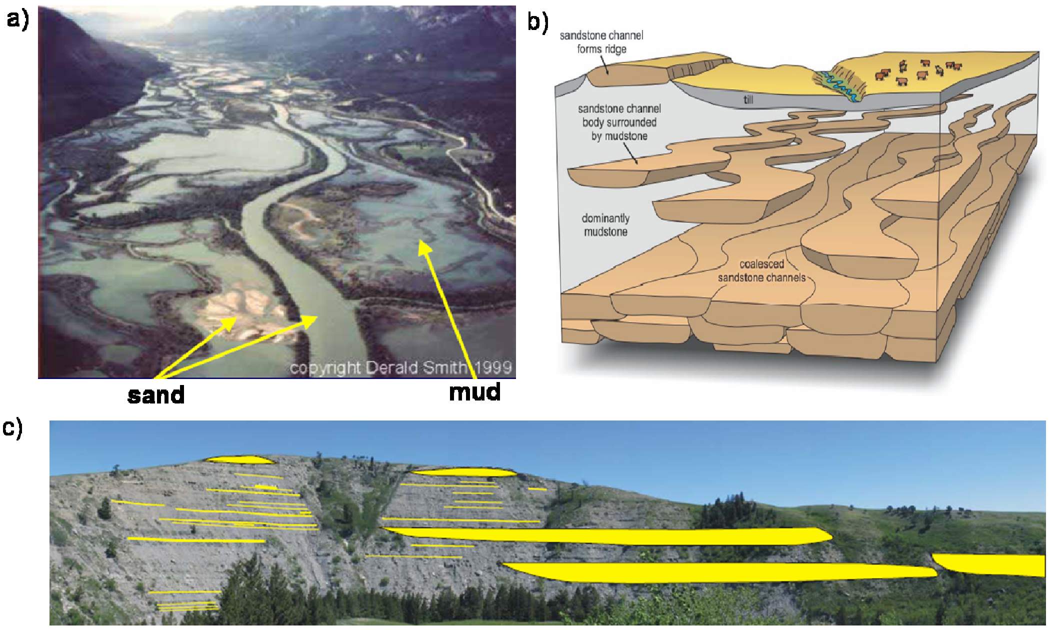

Figure 3.6: Complicated sand channel systems in Paskapoo Formation. a) Example of sand channels near the Bow River, Alberta. b) Schematic sketch of sand channels developed as fluvial deposit. c) Example of sand channel outcrops (yellow) in the Paskapoo Formation area. (from Grasby et al., 2007).

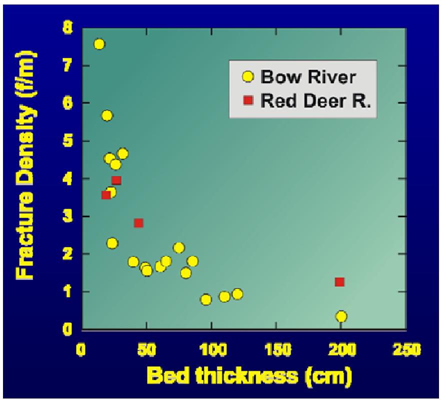

Figure 3.7: Relationship between fracture spacing and sand channel thickness. a) Fractures developed at shallow depths. b) Bed thickness versus the fracture density measured from samples from Bow River (Grasby et al. 2007).

3.3 Aquifer in the Paskapoo Formation

The Paskapoo Aquifer in the Calgary area is described as a confined aquifer and its source is considered to form the interbedded sandstone channels of the Paskapoo Formation. The sandstones have low transmissivity: wells founded in them are adequate for domestic use in rural areas around the city, but they are not sufficiently productive to be useful in a large-scale water-supply system. Water wells completed in the Paskapoo Aquifer are expected to yield approximately 33 m^3/day to 164 m^3/day (Ozoray and Barnes, 1977). The driller's report for the Rothney well shows that a water flow rate of 81.8 m^3/day was measured from the near-surface aquifer at depths of 24 m to 28 m: This zone is speculated to be the largest source of groundwater in this well.

3.3.1 Water Quality

The groundwater in the Paskapoo aquifer is generally chemically hard and high in dissolved iron: As water infiltrates into the ground it dissolves soluble materials. The most soluble minerals are dissolved first and as time progresses the less soluble materials come into solution (Ozoray and Barnes, 1977).

The Paskapoo Formation is dominated by a sodium-bicarbonate or sodium-sulphate type waters. The TDS (total dissolved solids) concentrations in the Paskapoo Formation range from less than 500 mg/L to more than 3,000 mg/L. As depth increases, the TDS concentration generally increases (Agriculture and Agri-Foods Canada, 2002). The actual amount of TDS of the water extracted from Rothney well was 300 ppm (part-per-million). Considering that the TDS for tap water normally ranges from 140 to 400 ppm (www.waterfiltersonline.com), the untreated water from the near-surface aquifer is of excellent quality.

3.3.2 Regional water usage

The Alberta Environment – Groundwater Information Centre (AE-GIC) was reviewed for records of water wells located near the survey site and within the watershed. Water wells that are located within 3 km radius from the watershed boundary are summarised on Table 3.2. The groundwater is mostly used for domestic purposes and there are approximately 636 water wells in the area for domestic use in the watershed.

Table 3.2: Water wells in the Paskapoo aquifer.

	Domestic	Industrial	Stock	Unknown	Multiple Classifications	Total
Wells completed in the Paskapoo Aquifer	636	5	19	24	25	709

3.4 Well logs and 3C-geophone VSP data acquisition

3.4.1 Well-logs

A suite of well log measurements including gamma-ray, 16-inch resistivity, neutron-porosity, density, caliper, spontaneous-potential, and temperature logs was acquired by Roke Oil Enterprise Limited (Figure 3.8 *a* and Figure 3.9) in the open-hole before the 15.6 cm diameter well was cased with PVC (Figure 3.8 *b*). The full-wave form sonic log (Figure 3.8 *c* and Figure 3.10), was acquired after the well was cased. At the time when the open-hole logs were taken, the static water level was 30 m.

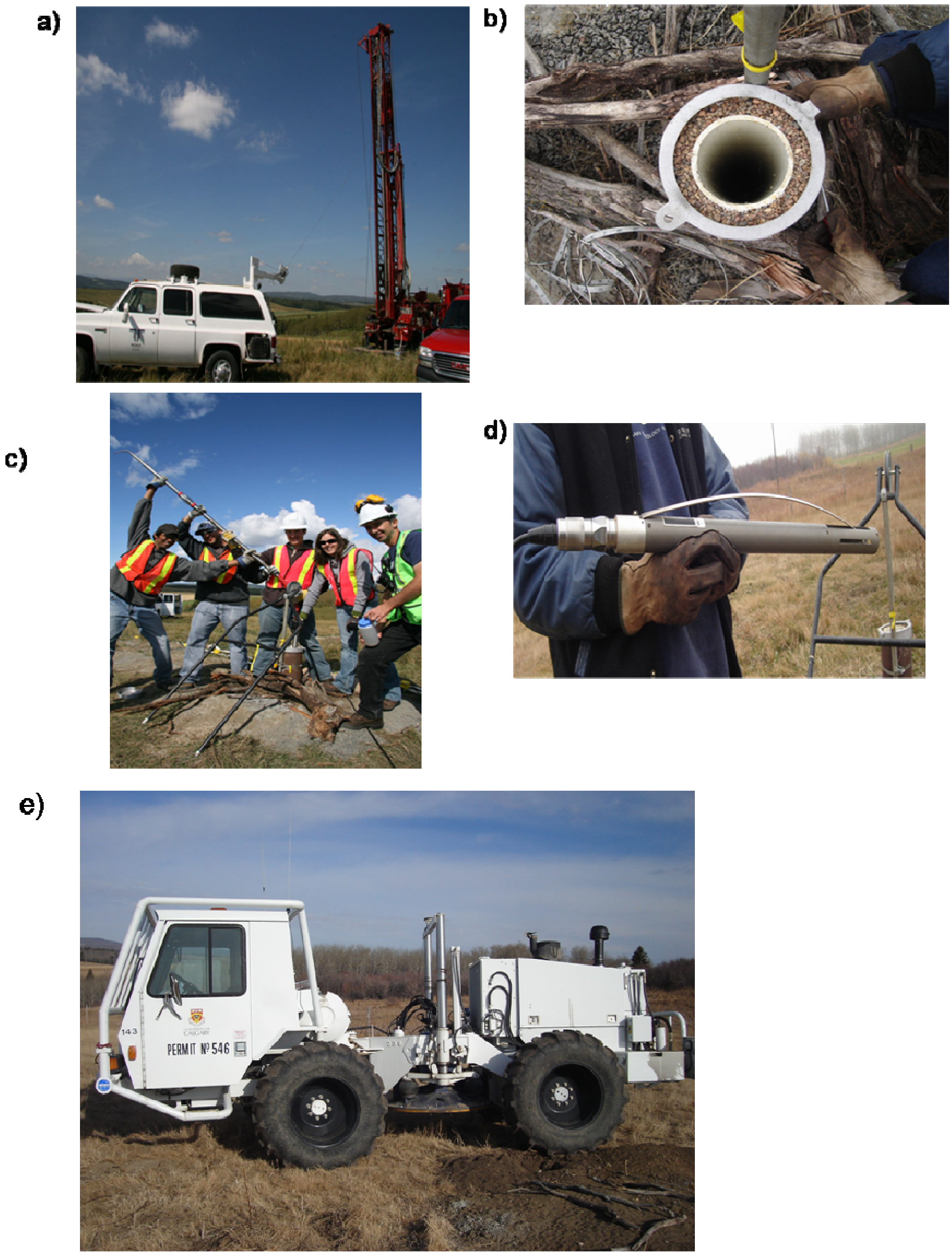

Figure 3.8: a) Roke Well logging company's logging unit; b) 4.5 inch inner-diameter of the test well; c) undergraduate geophysics students and CREWES staff deploying full-waveform sonic log tool; d) multi-component clamping-geophone used for VSP survey; e) 18 000 lb Enviro Vibe source. (Photos a) and c) were taken in August 2007 during U of C geophysics field school by R.R. Stewart, Photos b), d) and e) were taken in March 2008 by S. Miong).

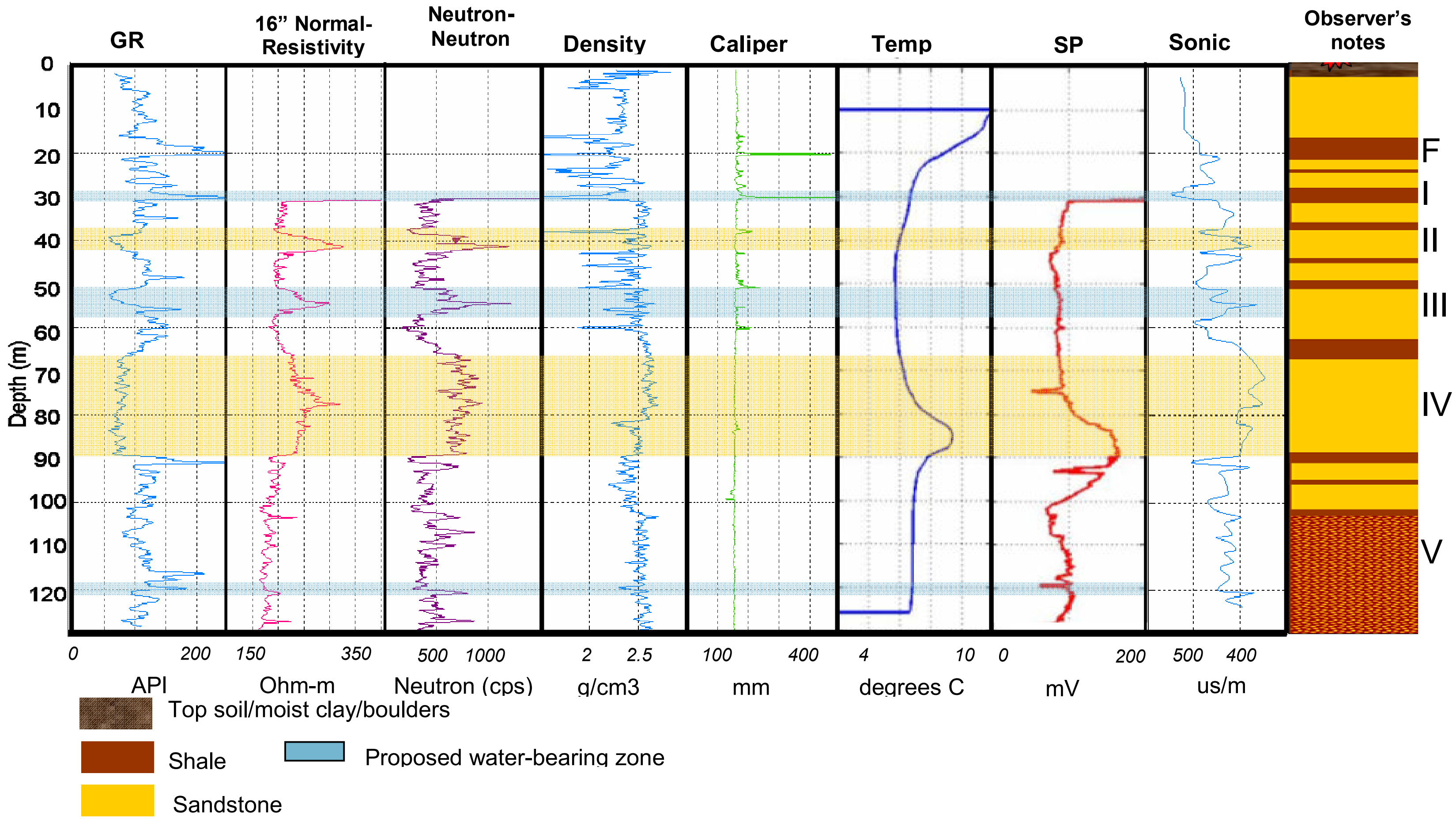

Figure 3.9: Open-hole well logs (GR, resistivity, neutron-porosity, density, caliper, temperature, and spontaneous-potential) and case-hole log (sonic) with formation log description recorded by the driller. "F" denotes shallowest fracture, and the Roman letters I to V denote zones of interest.

In 2007, CREWES purchased a Mount Sopris Instruments Matrix II geophysical logging system, which was tested in the Rothney well. The system hardware includes natural gamma-ray, single-point resistance, spontaneous potential, and full-waveform sonic tools (Wong et al., 2008). Because this particular well was cased with PVC, only the natural gamma-ray and the full-waveform sonic tools were used.

The full-waveform sonic tool consists of a small piezoelectric transmitter near the bottom of the tool; three piezoelectric receivers (Rx-1, Rx-2, and Rx-3) are located 0.914 m, 1.22 m, and 1.52 m above the transmitter. In recording full waveforms, the transmitter was driven by a pulse with dominant frequency of about 15 kHz. For each of the three receivers, the seismograms were acquired with 525 digital points with 4 sec sampling at depth intervals of 10 cm. Figure 3.10 shows a gamma ray log and full-wave form sonic logs acquired from the cased test well (Wong et al., 2008).

The sonic log used in the VSP analysis (Figure 3.9) was obtained by traveltime inversions of first-arrival times recorded by the three piezoelectric receivers and by taking the average of the resultant slownesses (Wong et al., 2008). Although applying automatic gain control on the raw full-waveform sonic logs facilitated more accurate first-arrival picking, it was very difficult to pick first-arrivals at depths above 20 m. The poor signal amplitudes at these depths indicate poor coupling between the formation rocks and the well casing, possibly due to uneven sealing by the bentonite pellets (Wong et al., 2008). Comparing the velocity profiles with the natural gamma-ray log on the left-hand side of the Figure 3.9, the lower velocity (2000 to 2200 m/s) zones coincide with high gamma-ray activity associated with shales. Higher velocities (2500 to 3000 m/s) coincide with low gamma-ray activity associated with sandstones.

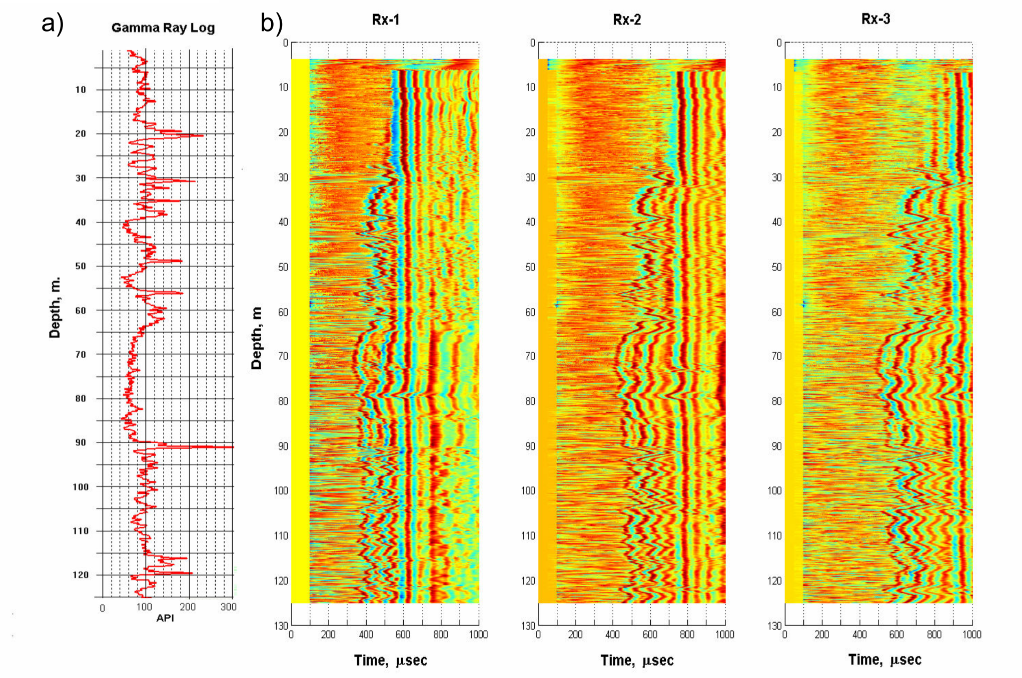

Figure 3.10: Cased-hole well logs a) Gamma-ray, b) full-wave form sonic logs for receivers Rx-1, Rx-2, and Rx-3 after automatic gain control (AGC) to enhance the clarity of the first breaks. The AGC facilitates interactive and automatic time picking (Wong et al., 2008).

3.4.2 3C-geophone VSP

As part of the field school exercise, a 1.5 m-offset VSP dataset was acquired by striking a spiked aluminum cylinder with a 7.5 kg sledgehammer as a seismic source and a 3C downhole sonde (Figure 3.8 *d*) spaced at 0.5 m. The depth coverage of the VSP survey is 4 m to 63 m (Figure 3.11 *a*). In March 2008, additional 15 m and 30 m offset VSP data were acquired with 0.5 m receiver spacing using an 18,000 lb EnviroVibe sweeping (Figure 3.8 *e*) over 15 to 250 Hz range (Figure 3.11 *b* and *c*). The data were acquired up to a depth of 90 m. These data were acquired rapidly: the data acquisition time, for the 1.5-m VSP data was about an hour, whereas it took about three hours to acquire each of the 15-m and 30-m VSP data.

The vibroseis-source VSP yielded superior quality data to that of the hammer source: The downgoing first-arrival and the reflected upgoing P-wave signatures are easily identified from the vibroseis-source data (see blue arrows in Figure 3.11). On the other hand, the hammer-source data are severely contaminated with tube-waves and a poor trace-to-trace wave consistency is observed. Strong tube-waves are observed from this data because the source was placed only 1.5 m away from the test well. Also, the inconsistency of the traces are the result of the sledgehammer striking the ground with varying force. The vibroseis-source data show credible reflections at depths of ~30 m, 50 m, and 80 m and some seismic wave mode conversion (Sv-wave) (Figure 3.11 *b* and *c*).

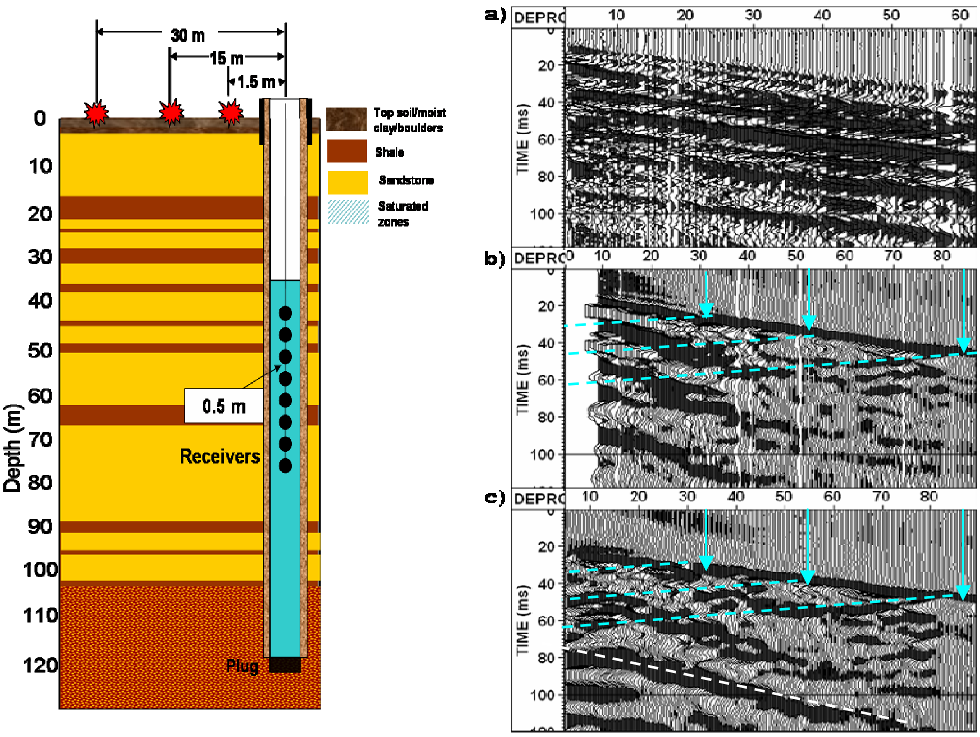

Figure 3.11. Geometry of VSP survey at shot offsets of 1.5 m, 15 m, and 30 m. Raw shallow VSP data (vertical component) at offsets of a) 1.5m, b) 15 m, and c) 30m; Receiver depth (x-axis) is plotted against the field recording times (y-axis). Blue and white lines indicate credible P-wave reflections and a converted S-wave, respectively.

3.5 Well-log analysis: Stratigraphic characterization

3.5.1 Qualitative well log analysis

As shown in Figure 3.9, various well logs show variations that follow closely the beds of sandstones and shales within the Paskapoo Formation that were identified by the driller (see Appendix A): The sandstone unit is usually characterized by low gamma-ray activity, high resistivity, high sonic velocities and vice versa for the shale or mudstone units. The density and caliper logs (Figure 3.9) indicate significant fracturing in the upper 60 m of the well. At these shallow depths, the thickness of the sandstone units are relatively small (<10 m) and these relatively thin beds are probably related to the higher density of fractures occurring at shallow depths as suggested by Grasby et al.'s (2007) study (see Figure 3.7).

The SP and temperature logs on Figure 3.9 appear to behave rather oddly. Both logs show broad maxima occurring at depths between 80 m and 90 m – in the middle of a 20 m thick sandstone unit. Usually, SP logs follow variations in lithology, permeability, and salinity of the formation water: SP highs are associated with shales and SP lows are associated with sandstones. However, opposite log signatures are observed in this case and the SP log doesn't seem to isolate the sandstone and shale units effectively. Therefore, any interpretation from SP was neglected.

Temperature logs can provide useful information on the movement of water through a borehole, including the location of depth intervals that produce or accept water; thus they can provide information related to permeability distribution (Keys, 1989). In this case, the temperature log shows a general decrease from the surface to the depths above the static water level of 30 m. At depths greater than 30 m, the temperature increases by approximately 1 degree C over a 60 m depth interval. Typical geothermal gradients range between 0.47 and 0.6 degree C per 30 m of depth (Keys, 1989) and the observed general temperature increase could be associated with the increasing geothermal temperature with depth.

A temperature anomaly is observed at 85 m, near the base of the large sandstone unit that extends from approximately 63 m to 90 m (*i.e.* zone IV). Majorowicz et al. (2006) suggests that a possible cause for such changes in the temperature with depth is due to downward flowing groundwater which is dependent on recharge rates, depth and time. This anomaly in the temperature log correlates with an anomaly on the caliper log which may indicate a small fracture that provides a possible pathway enabling the groundwater flow. Also, a slight decrease in sonic velocity, density, and resistivity values is observed which may indicate a change in rock properties at the base of the thick sandstone unit due to the groundwater inflow. The deeper shale unit at 90 m may be acting as an aquitard inhibiting downward water flow.

According to the driller's observations, there are three water-bearing zones at depths of approximately 30 m (zone I), 50 m (zone III), and 120 m (zone V). As shown in Figure 3.9, the depths of the stratigraphic interface and lithologies from both the formation description and the well logs like gamma-ray, caliper and the resistivity logs match reasonably well; however, there is a noticeable discrepancy between the lithological description and the well log information at zones II and III. Only zone III is identified as a water-bearing zone although the resistivity, sonic and gamma-ray values for zone II are quite similar to zone III. Also zone IV, the thick sandstone unit, was not identified as water-bearing. It was speculated that the zone II and IV may also be water-bearing zones but the driller might have missed recording this zone. Therefore, all zones of interest were regarded as potentially water-bearing zones in the following analysis.

3.5.2 Quantitative well log analysis

Based on the sonic log, a shale-corrected total porosity (ϕ_{sc}) for five porous zones was calculated while correcting for volume of shale (V_{sh}) present within the sandstone units using the gamma-ray log (Equation 3.1 to 3.4 also see Table 3.3). The typical slowness values for sandstone matrix (Δt_{ma}), shale (Δt_{sh}), and water (Δt_{w}) were used (from Asquith and Krygowski, 2004) for calculating the porosity. The value, Δt, was picked directly from the P-sonic log.

$$\phi_{sc} = \phi - V_{sh}(\phi_{sh}) \qquad 3.1)$$

$$\phi_{sh} = \frac{\Delta t_{sh} - \Delta t_{ma}}{\Delta t_{w} - \Delta t_{ma}} \qquad 3.2)$$

$$\phi = \frac{\Delta t - \Delta t_{ma}}{\Delta t_{w} - \Delta t_{ma}} \qquad 3.3)$$

$$V_{sh} = \frac{GR - GR_{0}}{GR_{100} - GR_{0}} \qquad 3.4)$$

The zone I, which is positioned in the shale-to-sandstone transition zone, shows unrealistically high porosity value. This is likely because there is a fracture occurring within this zone (as indicated by the large value of caliper measurement) and the slowness of sandstone matrix used in the porosity calculation may be inappropriate for this zone.

Table 3.3: Typical P-slowness values for sandstone matrix, water and shale.

$\Delta t_{ma}\ (\mu s/m)$	182
$\Delta t_{w}\ (\mu s/m)$	656
$\Delta t_{sh}\ (\mu s/m)$	280

Assuming that all porous zones are saturated with water, the water saturation of each zone was estimated using Archie's equation (Archie, 1942). Since the water resistivity varies with borehole temperature, the water resistivity was calibrated according to its formation temperature given resistivity of water (Rw) at 20°C (Rw@TRw=15.4 ohm-m at TRw=20°C; see Equation 3.5). Using the typical electric constants [*i.e.* tortuosity factor (a), cementation exponent (m) and saturation exponent (n)], the shale-corrected sonic porosity (ϕ_{sc}), and the resistivity (R_t) from the log, the water saturation (S_w) is estimated (Equation 3.6; also see Table 3.). The typical tortuosity factor (*a*) and saturation exponent (*n*) for clean sandstone units were used for all five zones and they are 0.62 and 2, respectively. The cementation factors (m) for fractured zone (zone I) and rest of the porous zones are 1.7 and 2.15, respectively.

$$RW@FT = \frac{RW@TRW \cdot (TRW + KT1)}{(FT + KT1)}, \quad \text{KT1=21.5 C} \qquad 3.5)$$

$$S_w = \left(\frac{a \cdot R_w}{R_t \cdot \phi^m} \right)^{\frac{1}{n}} \qquad 3.6)$$

Table 3.4: Porosities and saturation estimated for five porous zones.

Porous Zones	Vsh	ϕ	FT (C)	RESD (Ohm-m)	Rw (Ohm-m)	Sw
I	0.29	0.58	6.7	2500.0	1607.9	0.12
II	0.00	0.42	6.0	300.0	74.1	0.56
III	0.00	0.50	5.8	325.0	69.3	0.44
IV	0.07	0.34	6.8	273.0	43.2	0.72
V	0.21	0.36	6.9	203.0	36.1	0.79

As shown in Table 3.4, the saturation value ranges from 0.12 in zone I to 0.79 in zone V. We expected a water saturation value of ~1 from zones I, III and V as they were specified as water-bearing zones by the driller. The inaccurate water saturation estimation maybe due to the following reasons: (1) The length of the fracture in zone I is greater than the maximum depth of electric current penetration; (2) The electric constants used for the water saturation calculation may have been inappropriate as they are typical values for sandstone units at greater depths (thousands of metres): Appropriate electrical constants for an overburden layer should be investigated; (3) Limitations to Archie's equation as it tends to give unrealistically large values of water saturation in shale formations (Asquith and Krygowski, 2004).

3.6 Sonic calibration and synthetic seismogram generation

3.6.1 Sonic Calibration

Using the observed first-arrival times picked from the three VSP gathers (Figure 3.11) and their geometry, interval velocities were calculated (Figure 3.12). The generally higher interval velocities with increasing VSP offset may be due to strong local anisotropy (L. Bentley, personal communication, 2008) or a somewhat limited velocity inversion procedure. Despite these velocity discrepancies, all three velocity models show similar high and low velocity zones occurring at depths of 30 m, 45 m, and 62 m and these depths also agree with the depths of the major seismic interfaces identified from the well logs (Figure 3.11).

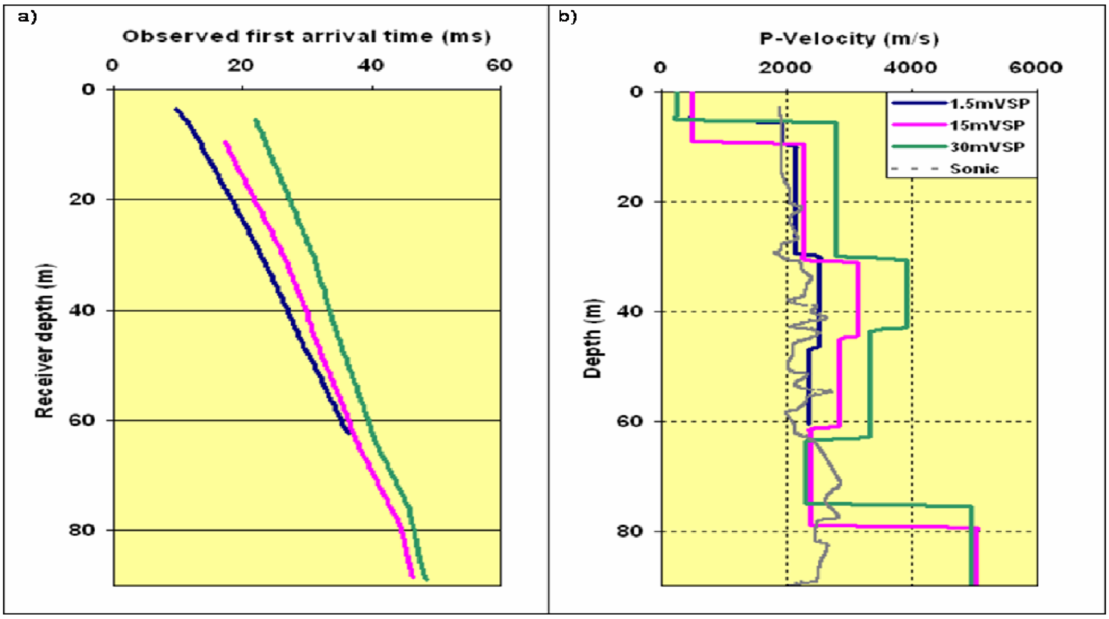

Figure 3.12: a) Observed normal-moveout corrected (NMO) first-arrival times versus the position of the receiver depths; b) Interval velocities calculated from the three shot gathers in Figure 3.11 at offsets of 1.5 m, 15 m, and 30 m.

The P-wave sonic log was calibrated using the observed first-arrival times from the 15 m-offset VSP data. As shown in Figure 3.13 a), sonic traveltime becomes longer than VSP traveltime with increasing depth. Although sonic times are often expected to be shorter than the VSP traveltime at greater depths due to their higher source frequency (Stewart et al., 1984), there are cases where the sonic traveltimes are larger than VSP times at shallow depths (Goetz et al., 1979, also see Figure 3.14). In this case, the delayed sonic traveltimes may be due to anisotropy (as mentioned before), overly simplified ray-tracing, lateral variations away from the well, or variable effect of fractures. This discrepancy could bear further investigation. The respective P-wave velocities of clean sandstone and shale zones are 2500 m/s-3200 m/s and 1900 m/s-2300 m/s after calibrating the P-wave sonic log using the VSP data (see Figure 3.13 *b* and Figure 3.15).

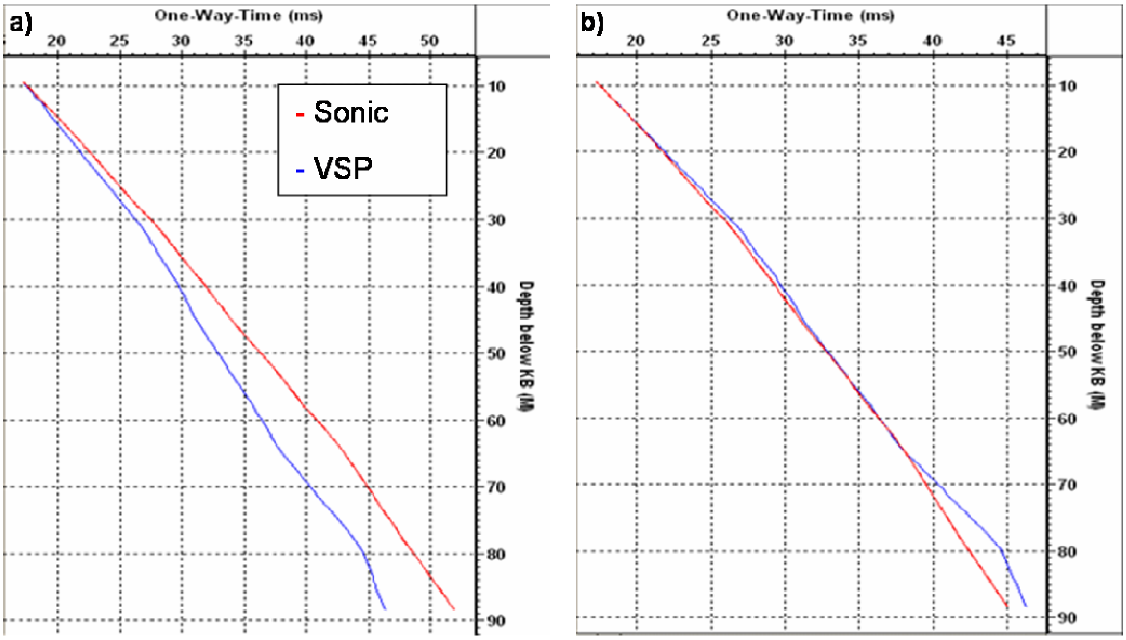

Figure 3.13: Comparison of the observed first-arrival times picked from 15 m VSP shot gather (blue) with traveltimes computed from the a) un-calibrated and b) calibrated P-wave sonic velocities (red).

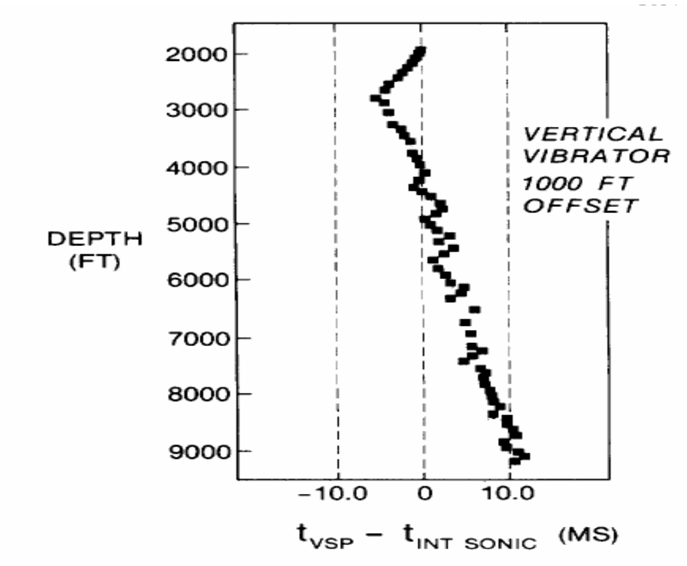

Figure 3.14: Typical example of a drift curve. The seismic traveltime from source to receiver (reduced to the vertical using cosine correction) minus the integrated sonic time to the receiver's depth is plotted against depth (Stewart et al., 1984)

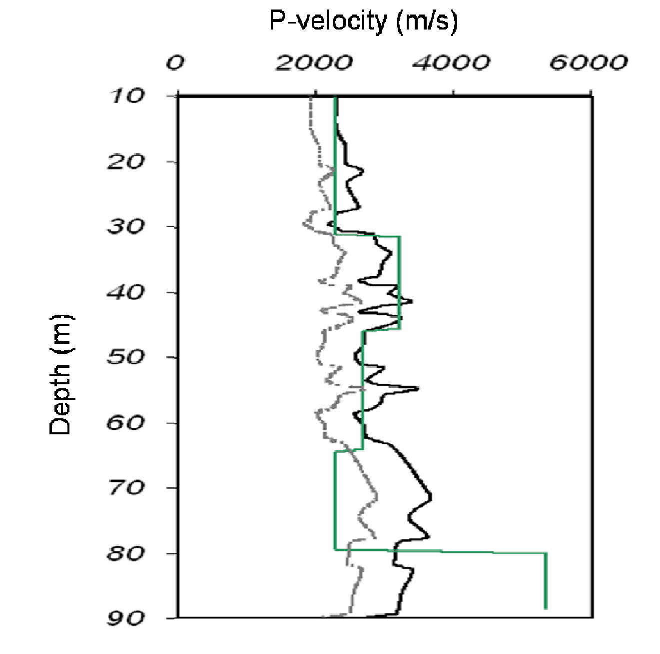

Figure 3.15: P-wave sonic log before (grey) and after (black) the calibration. The green curve represents the interval velocities calculated from the observed first-arrival times of 15-m offset VSP data.

3.6.2 Synthetic seismogram generation

A synthetic seismogram was generated for VSP interpretation. Using the simulated vibroseis sweep of 15 Hz to 250 Hz over 11 seconds, a zero-phase wavelet was designed (Figure 3.16 *a* and *b*). From the calibrated sonic and density logs, the P-wave impedance (Equation 3.7) and reflectivity (Equation 3.8) at each depth z_i were calculated:

$$I_i = \rho_i * V_i \qquad 3.7)$$

$$R_i = (I_{i+1} - I_i) / (I_{i+1} + I_i) \qquad 3.8)$$

Here, ρ_i and V_i are the density and velocity values at depth z_i. The reflectivity function and the designed wavelet were then convolved to generate a 1-D synthetic seismogram in two-way traveltime. Applying the velocity log information, this synthetic seismogram can be mapped to depth (Figure 3.16 *c*). Since no sonic velocity values were measured at shallow depths (*i.e.* less than 4 m), an overburden velocity of 520 m/s was estimated from the first-arrival time of the shallowest VSP receiver depth.

In the transition from shale to sandstone units, the increasing velocity on the sonic log (as well as density) results in a positive reflection coefficient. The corresponding event on the synthetic seismogram is a peak (in Figure 3.16 c an example can be seen at 31 m). On the other hand, the transition from sandstone to shale units is characterized by a decrease in velocity and density, thus resulting in a negative reflection coefficient. The event is identified as a trough on the synthetic seismogram (in Figure 3.16 *b* an example can be seen at 60 m).

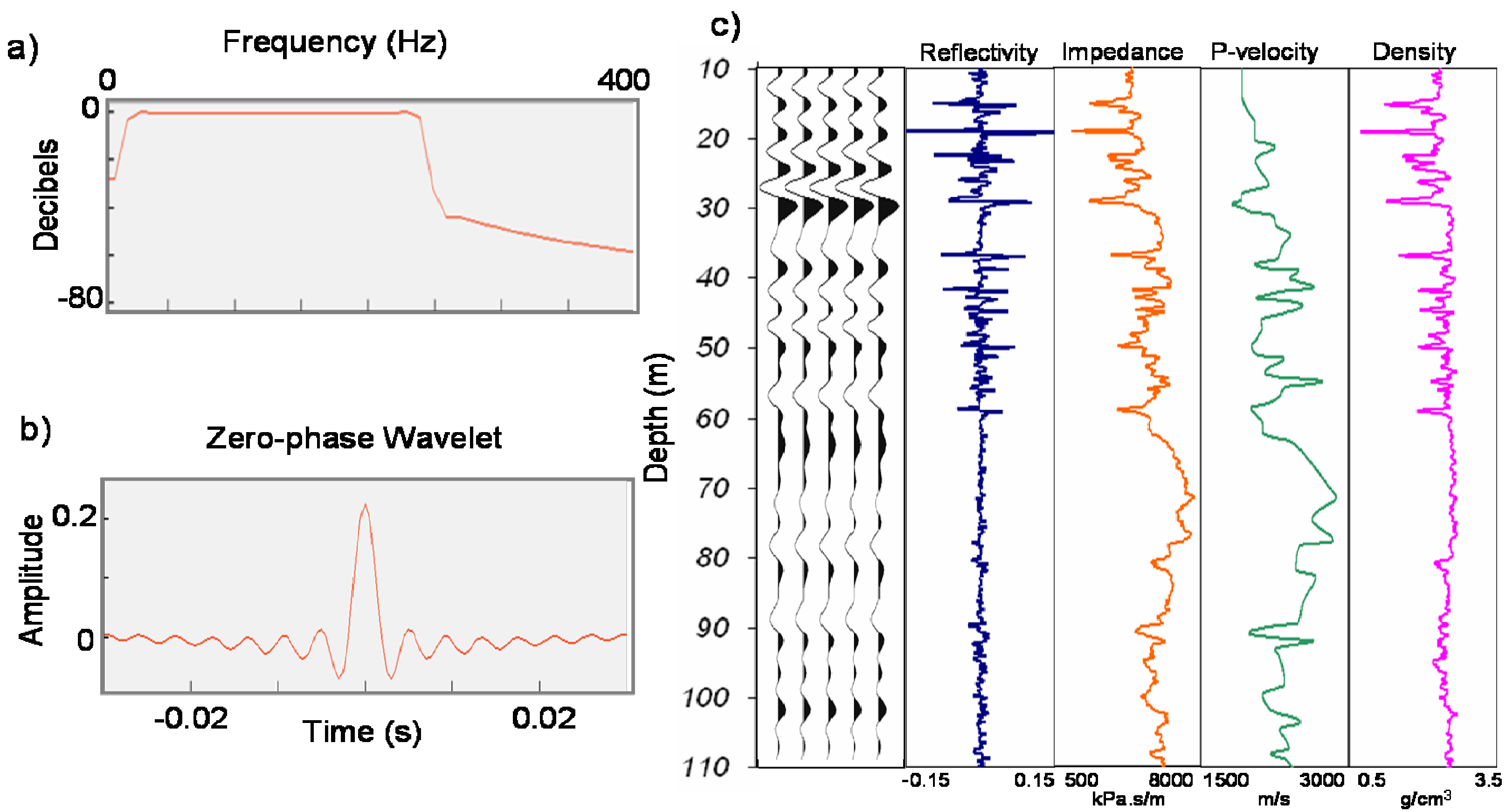

Figure 3.16: Synthetic seismogram generation. a) Simulated vibroseis sweep of 15-250 Hz, b) Designed zero-phase wavelet and c) Synthetic seismogram plotted in depth.

Chapter 4: Interpretive VSP processing: Priddis Experiment

In this chapter, the basic processing steps used to analyze the Priddis VSP data (acquired at various offsets) are shown. The flow of the processing is similar whether the offset is small or large (Figure 4.1 *a* and *b*). Therefore, only the unique processing steps for near- and far-offset VSP data will be discussed. The fundamentals of wavefield separation, sensor orientation, deconvolution, and VSP corridor-stack are reviewed in Appendix B. Table 4.1 provides the geometry and source type of the three VSP datasets acquired at the Priddis survey site (which were processed and shown in this chapter).

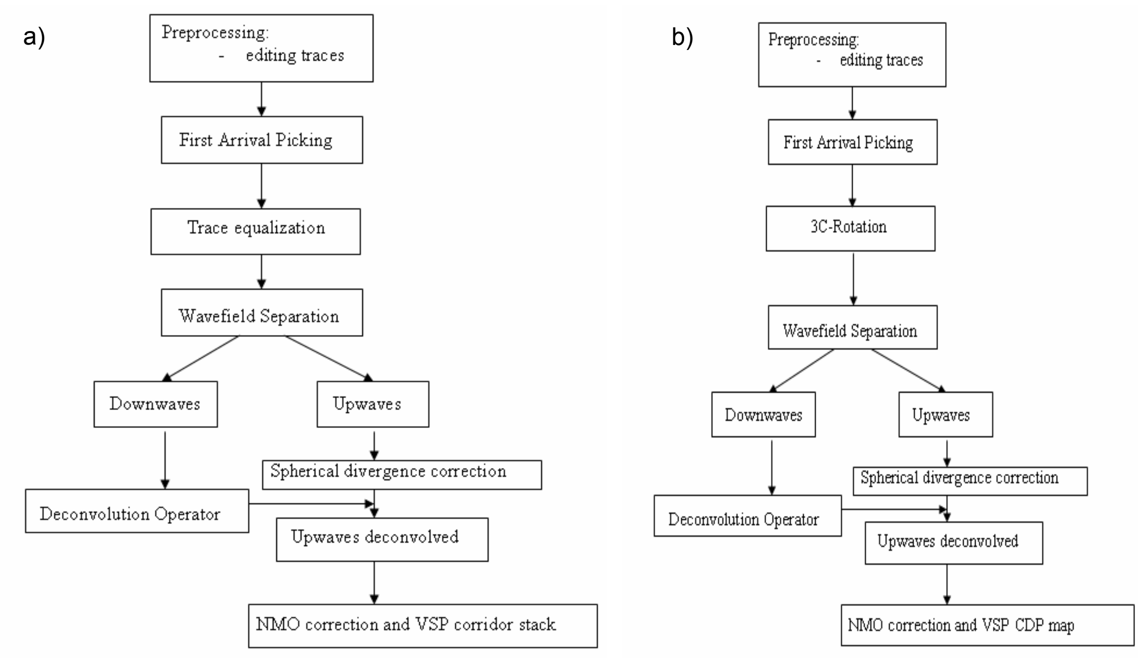

Figure 4.1. Processing flows for a) near-offset VSP and b) far-offset VSP.

Table 4.1: Geometry and source type of the three VSP datasets acquired from the Priddis survey site (also see Figure 3.11).

	Zero-offset VSP	**Near-offset VSP**	**Far-offset VSP**
Source offset	1.5 m	15 m	30 m
Source type	7.5 kg sledge hammer	18 000 lb Vibroseis	18 000 lb Vibroseis
Receiver spacing	0.5 m	0.5 m	0.5 m
Depth coverage	4 m-63 m	9 m-90 m	7 m-90 m

For all of the VSP processing, the geometry of the VSP needs to be implemented and noisy traces should be edited prior to processing. The first-arrival time (the traveltime for the fastest - usually direct - seismic wave to travel from a source to a receiver) is picked from the edited data. Also the shot strength variations and near-surface geology changes should be taken into account as the traces from raw field records may have varying power levels.

4.1 Near-offset (or 15 m-offset) VSP processing: Methods of wavefield separation

The types of waves that we expect to observe in VSP data include: (1) the downgoing P-wave first-arrivals, (2) upgoing P-wave reflections, (3) the downgoing and upgoing S-waves (dependent on the source offset), and (4) the downgoing and upgoing tube-waves, which are the typical type of noise in VSP data; the tube-waves travel at about 1500 m/s and can be generated from surface waves inducing vibrations in the fluid-filled borehole. It is the upgoing primary wavefield that provides reflectivity information about the subsurface; consequently, an important part of VSP processing is to separate the upcoming wavefield from the downgoing wavefield (DiSiena et al., 1984).

The common techniques that are used to separated wavefields include, median filtering (Stewart, 1984), Karhunen-Loeve (K-L) filtering (Hinds et al., 1996), Fourier transform (f-k) filtering, and t-p filtering (Kappus et al., 1990). Most of the conventional methods (*i.e.* f-k filtering and median filtering) use the different apparent velocities exhibited by the wavefields across the receiver array to separate the waves: In VSP records, downgoing waves exhibit positive apparent velocities and upgoing waves exhibit negative apparent velocities. Hence, the median filtering and f-k filtering techniques were used for separation of up- and down-going wavefields on 15 m-offset VSP data and their outputs were compared.

4.1.1 Wave separation using f-k filtering

The separation of VSP wave modes by *f-k* filtering is accomplished by transforming data (recorded in the time-space domain) to the frequency-wavenumber domain, by forward Fourier transform. It takes advantage of the apparent velocity exhibited by different wave modes and works in the frequency domain. Excellent overviews of *f-k* domain processing are presented in Yilmaz (1987) and Hardage (1992).

A series of *f-k* filters were designed to attenuate downgoing P, up- and down-going tube-waves, and downgoing Sv waves. The *f-k* filter designing process involves using interactive screen processing to compare the input and outputs of the *f-k* filtering step, evaluating the success of the single step of processing, and modifying the *f-k* filtering parameters until processing artifacts are minimized.

First, downgoing P waves were attenuated by defining a pie-slice reject zone in the *f-k* environment. As shown in Figure 4.2 a), the red zone represents the strong amplitude of the first-arrivals. After this zone has been rejected, the downgoing P waves are attenuated (Figure 4.2 *b*). As mentioned earlier, downgoing waves exhibit positive apparent velocities and the *f-k* placed them in the negative wavenumber half-plane.

A polygonal rejection zone (Figure 4.2 *c*) was further designed to attenuate downgoing Sv waves (shown in Figure 4.2 *b*): The Sv waves occur at a greater slope than the downgoing P-waves (Figure 4.2 *d*). Downgoing tube-waves are defined near a -0.05 m^{-1} wavenumber and 25 Hz (Figure 4.2 *e*) and they are successfully attenuated after the polygonal rejection (Figure 4.2 *f*). The upgoing tube-waves are characterized by same wavenumber and frequency, but are placed in the positive wavenumber quadrant (Figure 4.2 *g*). The upgoing tube-wave attenuated data is shown in Figure 4.2 h).

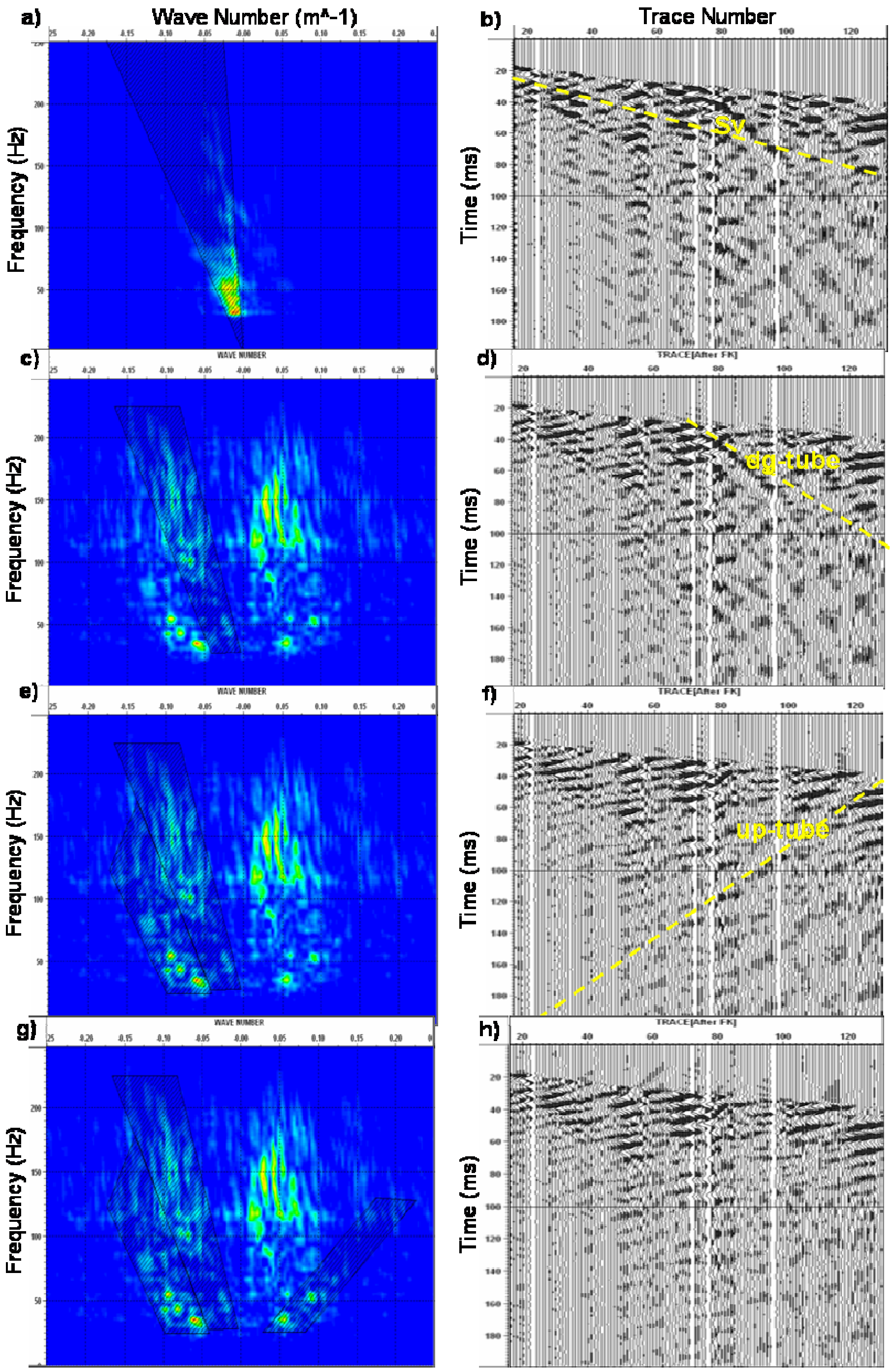

Figure 4.2: f-k filter design: a) downgoing P-wave; b) Z panel after downgoing P-wave removal; c) downgoing Sv-wave; d) Z panel after downgoing Sv-wave removal; e) downgoing tube-wave; f) Z panel after downgoing tube-wave removal; g) upgoing tube-wave; h) Z panel after upgoing tube-wave removal.

4.1.2 Wave separation using median filtering technique

A series of median filters were applied to separate downgoing P, up- and downgoing tube waves, and downgoing Sv waves (Figure 4.3). To extract downgoing P waves, the downgoing wavefield is first aligned at a constant time of 30 ms by shifting each trace by the negative of the first-arrival time. A 15-point median filter length was used in this case. The downgoing wavefield is then subtracted from the input total wavefield to yield the residual component which contains the upgoing P-waves and noise (see Figure 4.3 *a, b, c,* respectively). After the downgoing P-wave separation, stronger upgoing wavefields are observed; but it also enhanced the presence of the upgoing and downgoing tube-waves (see red line in Figure 4.3 *c* and *e*).

By picking arrival times of the tube-waves, aligning them at a constant time, and applying median filter, downgoing (Figure 4.3 *d* and *e*) and upgoing (Figure 4.3 *f* and *g*) tube-waves are extracted and they are respectively subtracted from the residual components shown in Figure 4.3 c) and e). Using the same procedure, another downgoing event, which is believed to be a downgoing vertical-shear wave, is attenuated. For these noise attenuations, a shorter 7-point median filter was applied. Since high-frequency fine steps or spikes are often generated as a result of the median filtering, a high-cut frequency filter of 230 Hz was applied to the final panel (Figure 4.3 *i*).

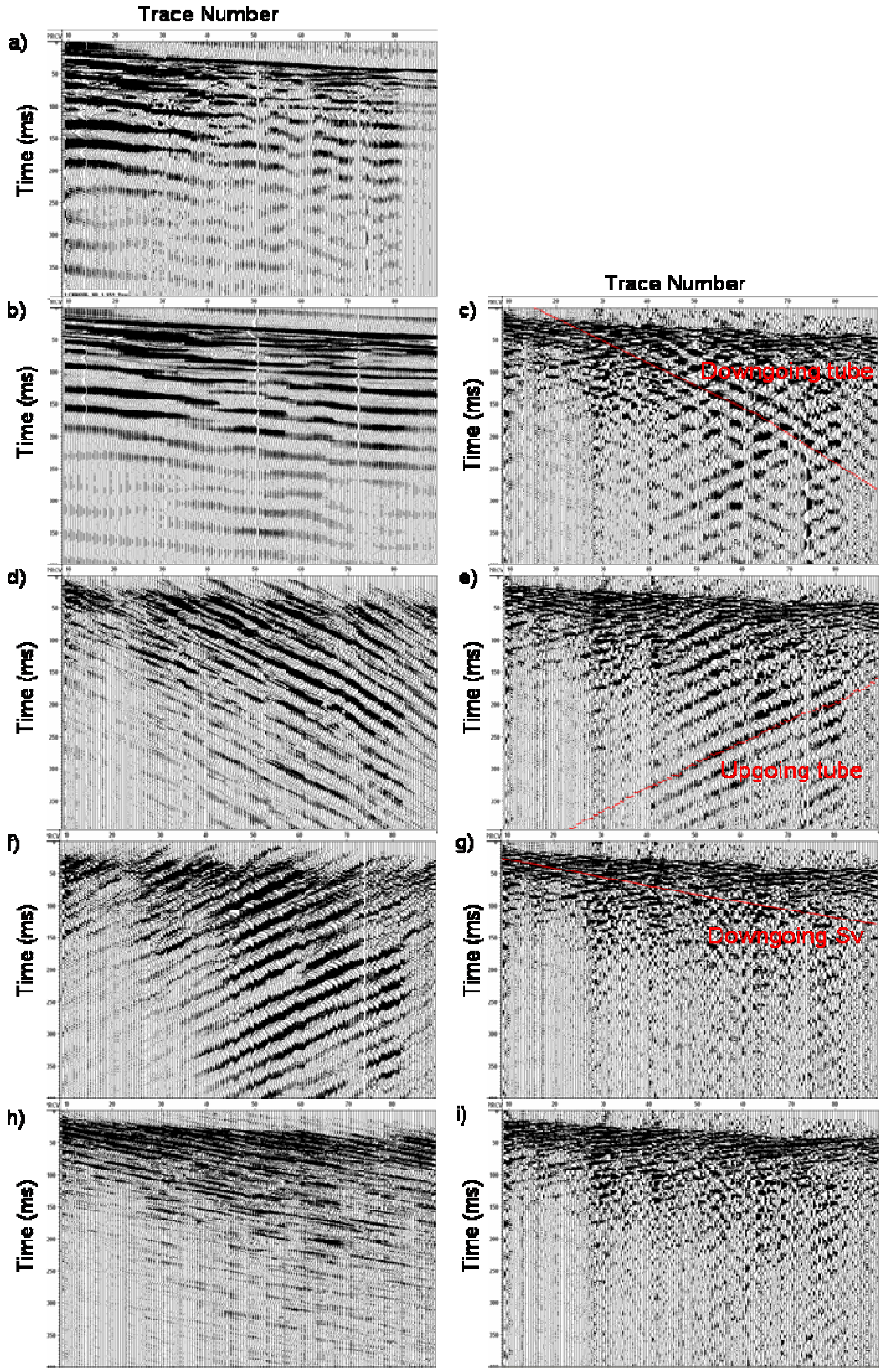

Figure 4.3: Wave separation using median filters: a) vertical component of the 15 m-offset raw VSP data; b) extracted downgoing P-wave; c) residual data after subtracting panel *b* from *a*; d) downgoing tube-wave; e) secondary residual after subtracting panel *d* from *c*; f) upgoing tube-wave; g) tertiary residual after subtracting panel *f* from *e*; h) downgoing Sv-wave; i) upgoing wavefields after noise attenuation.

4.1.3 Result comparison

Figure 4.4, compares the final upgoing P-wavefields extracted using the *f-k* and median filter techniques. Due to the relatively short length of the median filter for noise attenuation, remnants of upgoing tube-waves emerging at 9 m at a field-recording time of 120 ms are observed (Figure 4.4 *b*). Although the *f-k* filtering seems to have attenuated upgoing tube-waves effectively, some reflected P-waves might have also been rejected during its removal process. As a result, the amplitudes of the reflected waves seem smaller and inconsistent compared to the median-filtered result. This observation is more evident at greater receiver depths (>60 m) and longer field-recording times (40 ms). Hence, it was decided that the upgoing waves extracted by the median filtering technique would be used for further processing.

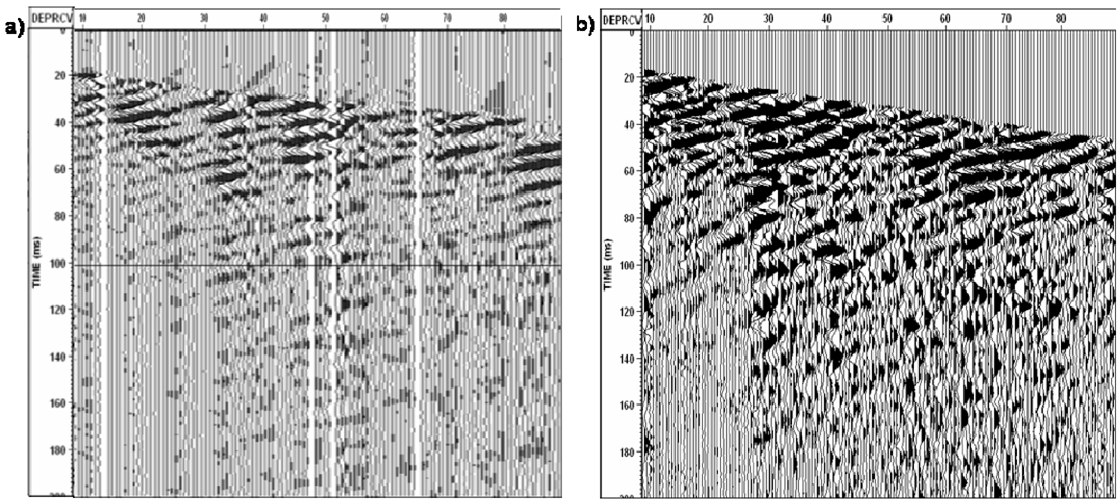

Figure 4.4: Extracted upgoing wavefields using a) an f-k filter and b) a median filter.

4.1.4 VSP corridor stack

Following the conventional processing flow for near-offset VSP data introduced in Figure 4.1, a VSP corridor stack is produced for the 15-m offset VSP field data (since it was considered as a near-offset VSP). A corridor with a width of 8 ms is defined for the NMO-corrected 15-m offset VSP field data (Figure 4.5 *a*) and its stack is repeated five times (Figure 4.5 *b*). For the NMO correction, a P-wave velocity model obtained from the traveltime inversion of the first-arrival times picked from the 15-m offset VSP data was used. A corridor stack for the 1.5-m offset VSP, which was acquired using a sledgehammer as a source, was obtained following the same processing flow and is shown in Figure 4.5 *c*. To correlate the 1.5-m offset VSP with the 15-m offset VSP, the polarity of the 1.5-moffset VSP was reversed and a 4 ms static shift was applied.

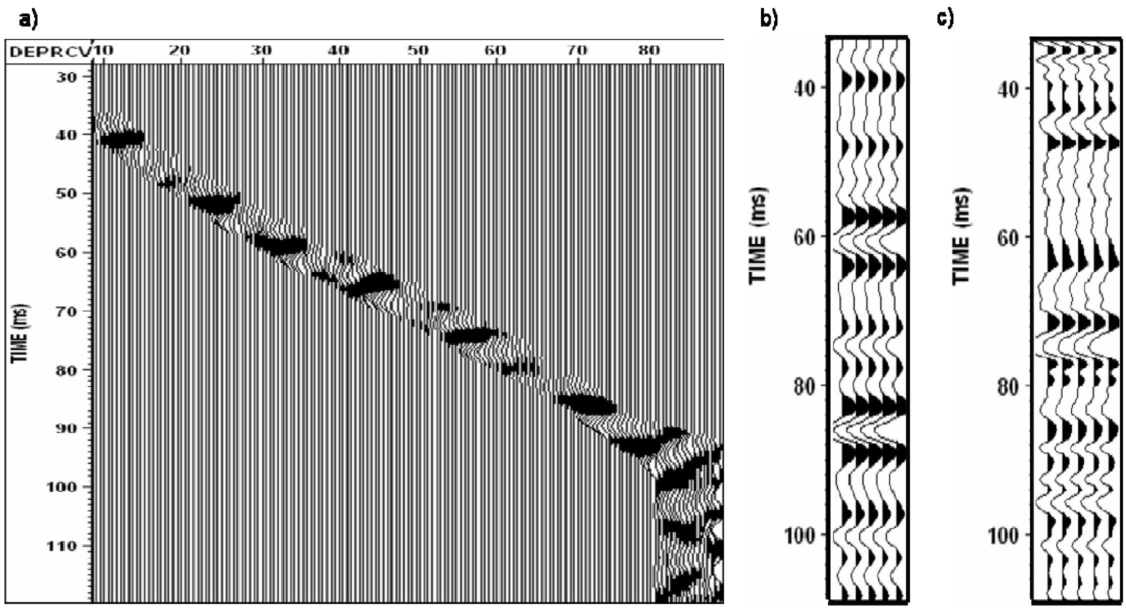

Figure 4.5: a) Corridor mute of NMO corrected 15-m offset VSP data and b) its corridor stack repeated five times, c) 1.5-m offset VSP corridor stack.

4.2 Far-offset (or 30-m offset) VSP processing

4.2.1 Geophone orientation: Hodogram analysis

As the offset between the shot and borehole increases, more energy from the shot is recorded on not only the vertical component but also on the horizontal and transverse channels. This implies that the incident angle of rays will not be a normal angle anymore and shear energy will be recorded in addition to the P-waves. Therefore, a unique step in processing the far-offset VSP data is that it involves P- and S-wave separation via sensor orientation. For the near-offset VSP, with a vertical source, usually no or little shear wave is recorded and most of the P-wave energy is recorded in the vertical component.

Figure 4.6 shows input and output for each sensor orientation processes. Three essential data are obtained from these sensor orientations. These are: (1) the maximized downgoing P-waves in Hmax' which can be used for designing the deconvolution operator, (2) the downgoing Sv-waves in Z' which can provide shear-wave velocities via traveltime inversion, and (3) enhanced upgoing P-waves in Z''up which can be used for imaging reflectors. The sensor orientation concept was applied to the 30 m-offset VSP data.

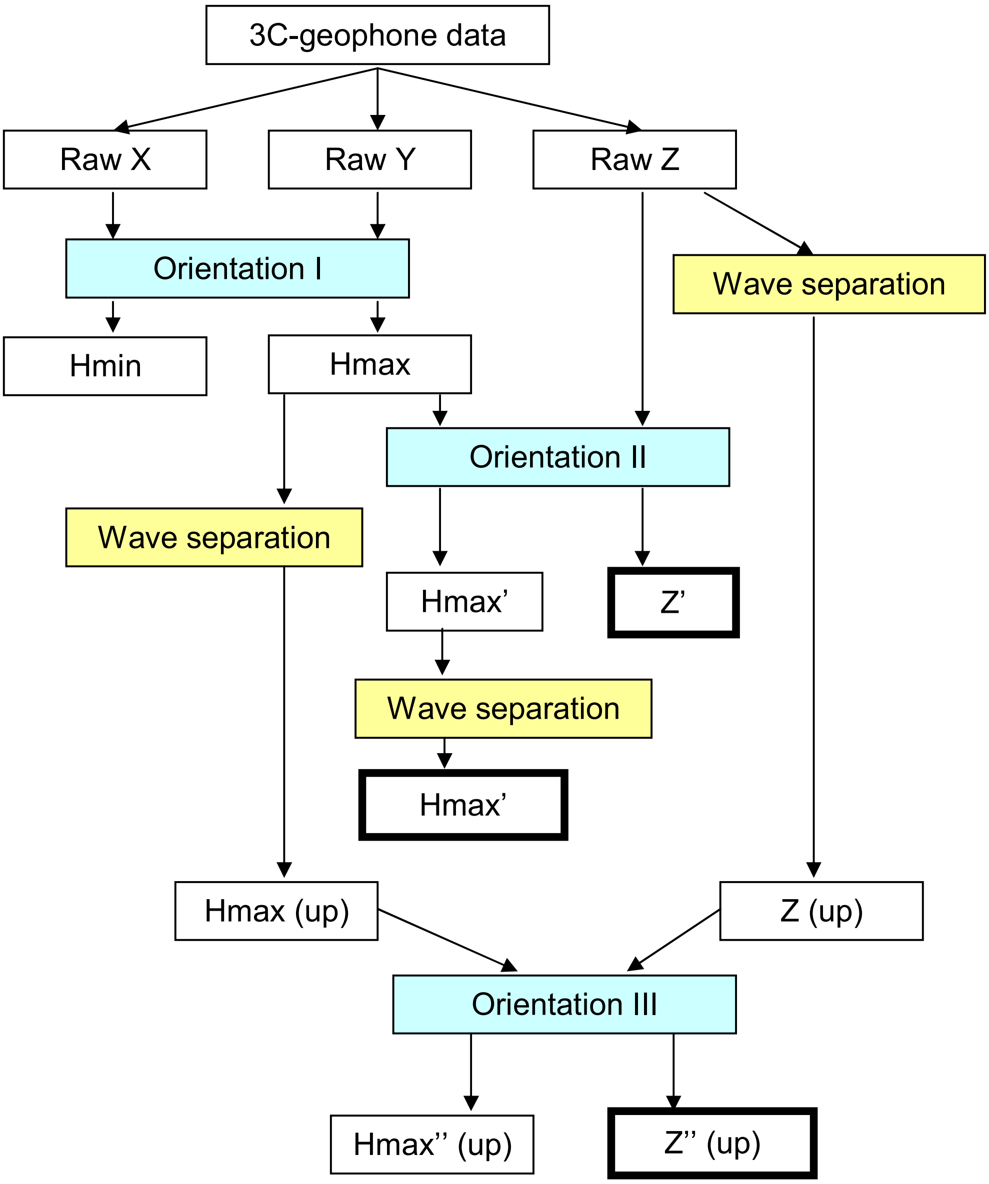

Figure 4.6: Flow chart for sensor orientation of far-offset VSP data.

4.2.1.1 Geophone orientation I and II: Time-invariant rotation

The rotation angle (θ) of the geophone for each orientation process is determined via hodogram analysis. Within the time window specified around the first-break wavelets in channels Y and X (Figure 4.7 *a* and *b*, respectively), their amplitudes are cross-plotted with line colouring changing as a function of time (Figure 4.7 *c*). The black line is the slope of the cross-plot of the two input signals, where the required polarization angle (θ) is determined so that one component is pointing toward the source (Hmax, Figure 4.7 *d*) and the other component is pointing 90 degrees from the maximum signal (Hmin, Figure 4.7).

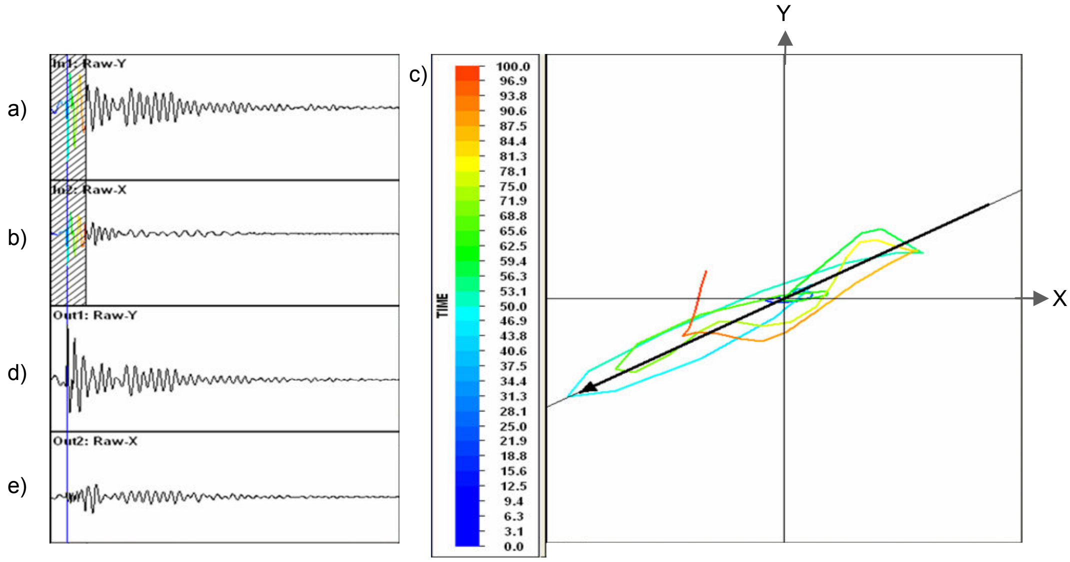

Figure 4.7: Application of hodogram analysis on the 30m-offset VSP data.

Figure 4.8 shows the horizontal channels before and after the first sensor orientation. The abrupt polarity reversal of the first break occurring at depths greater than 48 m in channel Y is corrected on Hmax. Figure 4.9 shows the result of secondary sensor orientation using Hmax and Z data as input. After the orientation, the downgoing P-wave energy is maximized on Hmax' and downgoing Sv energy is maximized on Z'. The first breaks are picked from Hmax' data to increase accuracy in first break picking and Hmax' is also used for designing the deconvolution operator (see section 4.2.2).

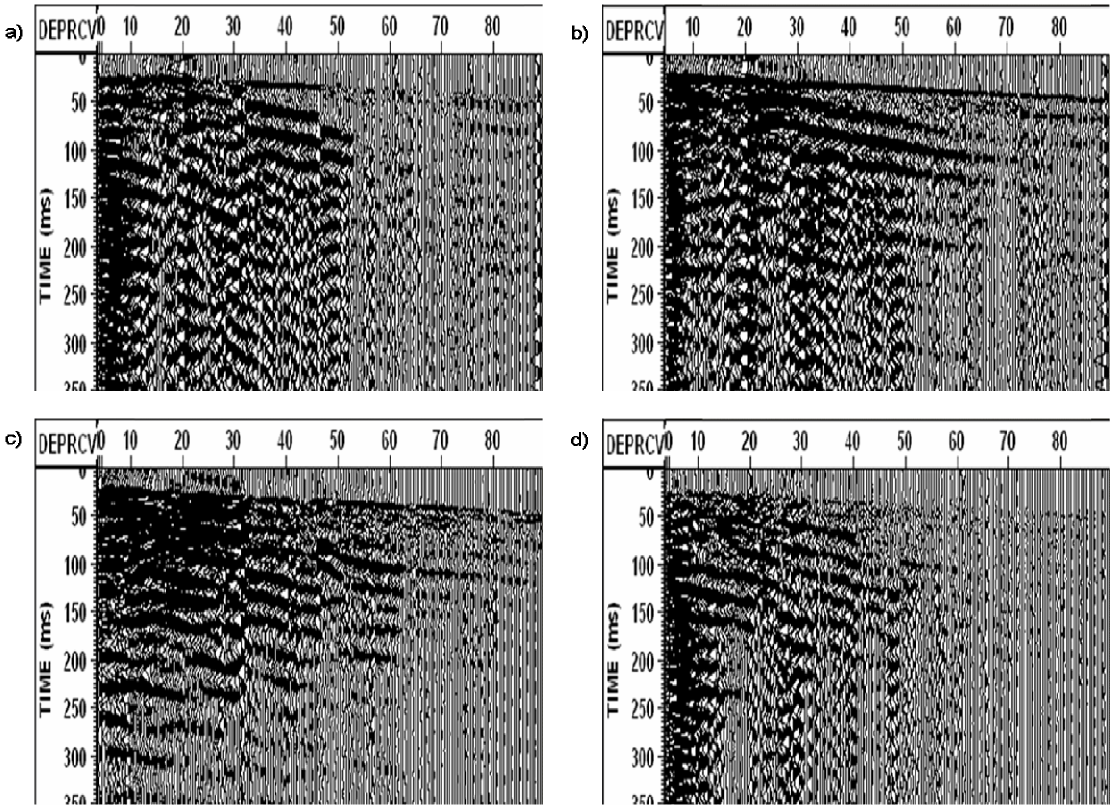

Figure 4.8: Horizontal components of 30-m offset VSP data before and after the first sensor orientation: a) input Y; b) output Hmax; c) input X; and d) output Hmin.

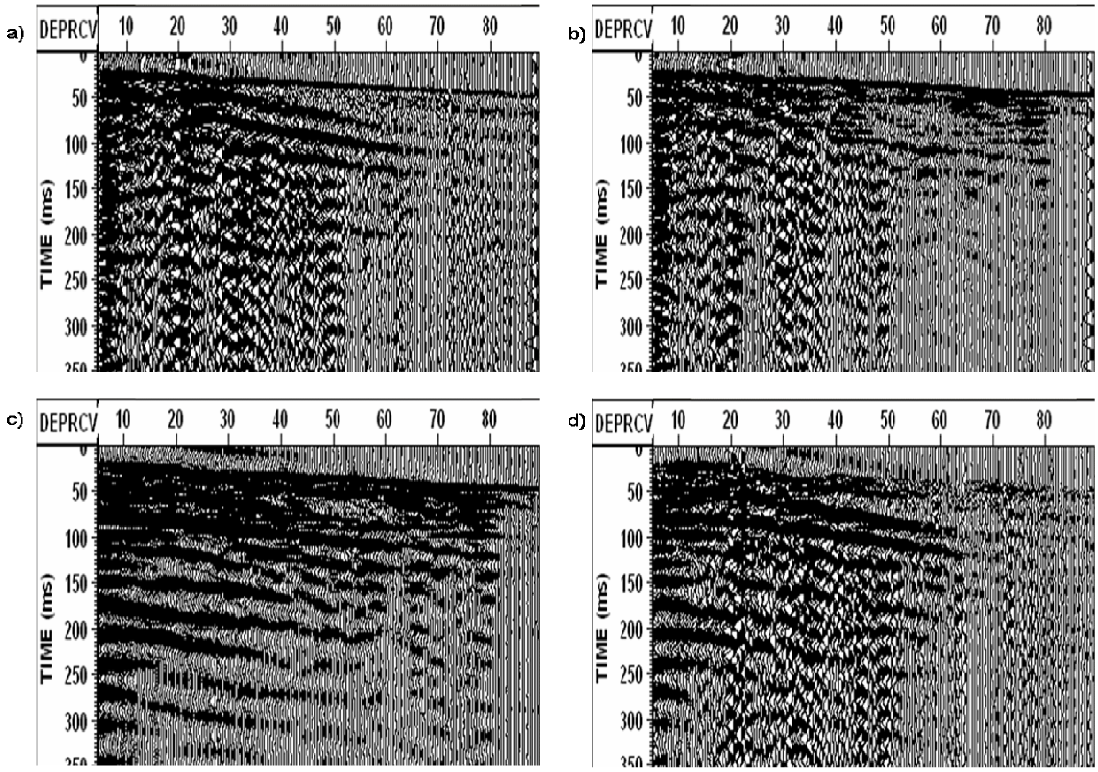

Figure 4.9: Maximization of downgoing P-wave via hodogram analysis: a) input Hmax; b) output Hmax'; c) input Z; d) output Z'.

4.2.1.2 Geophone Orientation III: Time-variant rotation

Using the survey geometry and the near-offset VSP velocity model, rays were traced to determine the time-variant polarization angle which provided the basis for rotating the Z and Hmax upgoing wavefields so that upgoing P- and Sv-waves can be separated. Prior to applying the time-variant rotation, the upgoing wavefields in Hmax and Z were extracted using the median filtering technique adapted from section 4.1.2. As shown in Figure 4.10, the two major upgoing wavefields extracted from the Hmax (Figure 4.10 *a*) and Z (Figure 4.10 *c*) are characterized by different slopes (*i.e.* events in Hmax have greater slope) suggesting that the upgoing events in Hmax indeed represent upgoing Sv waves. Since Hmax barely had any trace of the upgoing P-waves (*i.e.* events with smaller slope), applying time-variant rotation didn't make major improvements to our data (Figure 4.10 *b* and *d*).

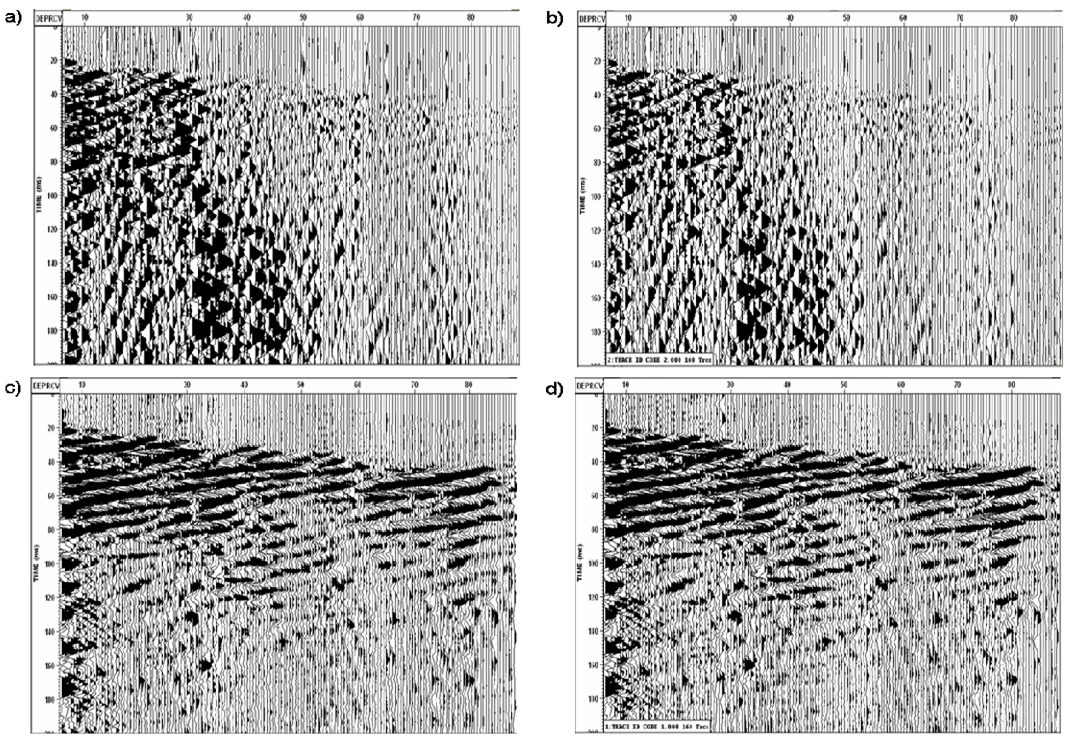

Figure 4.10: Time-variant rotation to separate upgoing P- and Sv-waves. Upgoing Hmax component a) before and b) after the time-variant rotation. Upgoing Z component c) before and d) after the time-variant rotation.

4.2.2 Deconvolution

A primary objective of VSP processing is to enhance primary reflections as an estimate of reflection coefficients. In VSP processing, the downgoing wave deconvolution is routinely used to enhance the primary reflections and it is used to transform the wavelets from the field data to zero-phase wavelets while suppressing the multiple reflections.

Figure 4.11 shows time-variant rotated upgoing-P wavefields before and after applying the deconvolution. Through interactive screen processing to compare the input and outputs of the deconvolution step, evaluating the success of the deconvolution and modifying the deconvolution parameters until processing artifacts are minimized, it was determined that a window size of 100 ms, a filter length of 70 ms and 0.5% pre-whitening seemed be the most optimal deconvolution parameters. The upgoing P-waves generally look sharper and are more continuous after the deconvolution. Figure 4.12 shows a wavelet picked at a depth of 10 m before and after the deconvolution: The minimum-phase first break is successfully transformed into zero-phase and the decreasing amplitude at the higher frequencies (>120 Hz) events are amplified after the deconvolution.

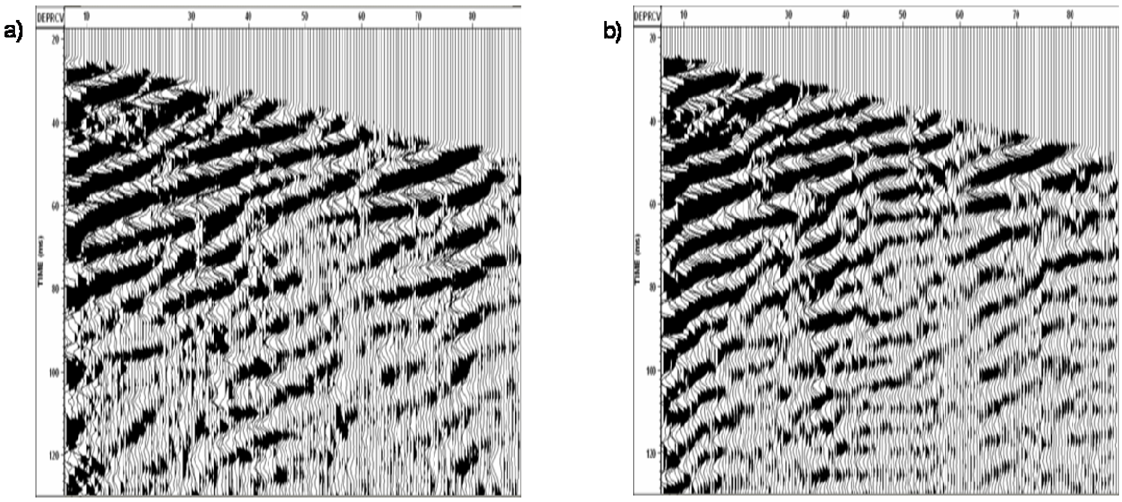

Figure 4.11: Upgoing P-wavefields a) before and b) after the deconvolution.

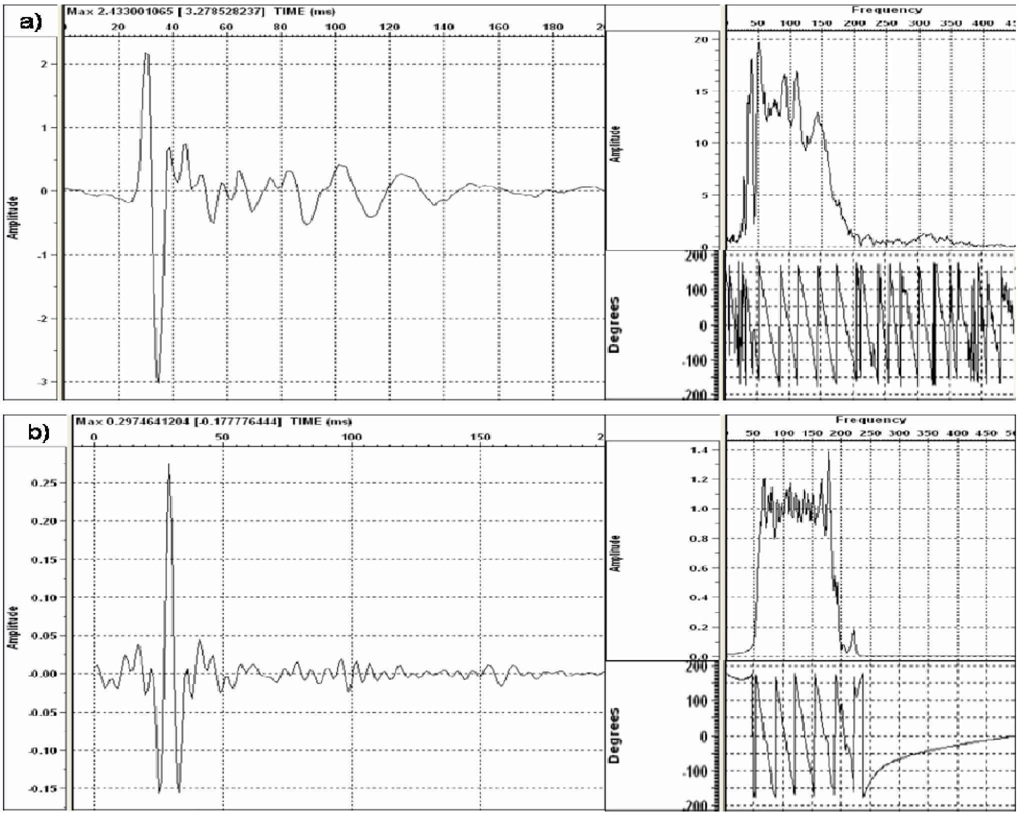

Figure 4.12: A trace at a depth of 10 m with its amplitude and phase a) before and b) after the deconvolution.

4.2.3 Spherical divergence correction

Several physical processes effect the amplitude of a propagating seismic wavelet. The most important is spherical divergence, where the amplitude decreases with depth. By analyzing the rate of decay exhibited by the first-break amplitudes, an exponential gain function can be computed and applied. It consists of multiplying each time sample's amplitude by a scalar T^{α}, where T is the recording time and α is a constant coefficient. In our case, α value of 1.1 seemed to account for the spherical divergence reasonably well (Figure 4.13).

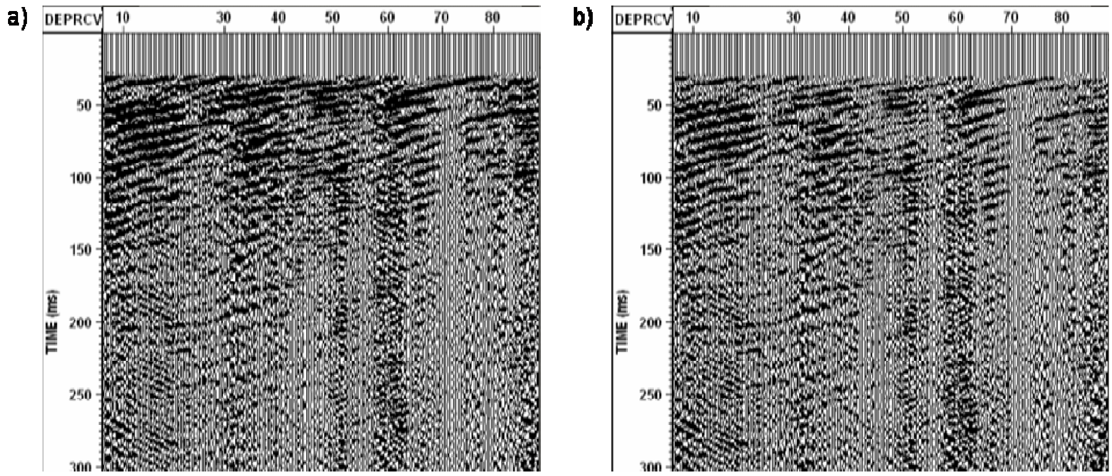

Figure 4.13: Deconvolved upgoing P-waves a) before and b) after the spherical divergence correction. The times are flattened at 30 ms.

4.2.4 Normal-moveout correction

Unlike surface recorded signals, the locus of reflection points for each source-receiver pair in VSP surveys depends on reflector depth. It tends towards the source-receiver midpoint with increasing depth in a horizontally layered earth (see Dillon and Thomson (1984) for excellent examples). Therefore, VSP data cannot be sorted simply in the CMP domain as in surface seismic surveys. Also, the RMS velocity for reflected signals in the VSP geometry changes with the receiver depths/locations, which implies that to use the inherent data redundancy, VSP data needs to be sorted in the receiver domain for implementation of a NMO correction method similar to the one used in surface seismic surveys.

After the vertical component data are sorted into the receiver domain, Equation 4.1, where x is the offset of the source from each receiver and $\bar{v}$ is the rms velocity, is used on the first-break picks to get the zero-offset time of the direct arrivals (t_{0d}).

$$t^2 = t_{0d}^2 + \frac{x^2}{(\bar{v})^2} \qquad 4.1)$$

Further, amplitude semblance analysis (see Taner and Koehler (1969) for details) of the reflected arrivals based on Equation 4.2 gives the zero-offset time (t_{0r}) for each of the reflected arrivals in the sorted data.

$$t^2 = t_{0r}^2 + \frac{x^2}{(\bar{v})^2} \qquad 4.2)$$

The quantities t_{0d} and t_{0r} are then added to obtain the normal incidence time of the reflected arrivals. The v_{rms} used for the NMO correction is calculated from the 15m-offset VSP since the velocity model derived from far-offset VSP data can be misleading as the first-arrival events occasionally interfere with the refracted waves. Figure 4.14 shows the field data before and after the NMO correction: the upgoing P-wavefields are mostly flattened after the NMO correction. Note that Figure 4.14 a) is plotted in the field-recording time and Figure 4.14 b) is recorded in two-way traveltime.

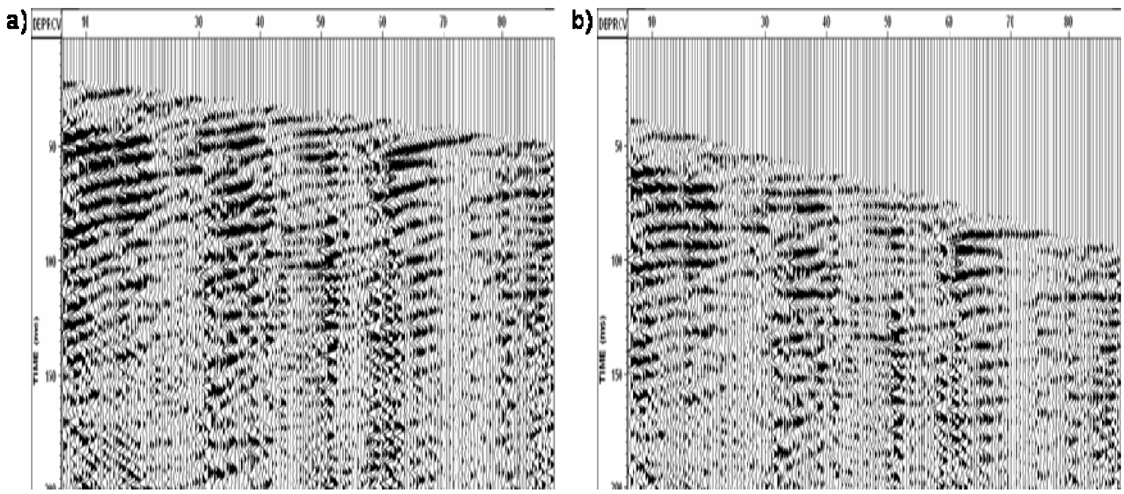

Figure 4.14: 30-m offset VSP data a) before and b) after applying NMO correction.

4.2.5 *VSPCDP mapping*

To properly position the reflection points away from the well, a VSP common-depth-point (CDP) map is used. This VSPCDP map is produced by stretching the recorded traces along their reflection point locus curve. After the stretching, the data are trace-resampled.

The standard procedure for VSPCDP mapping involves raytracing through a P-wave velocity model to map the spatial locations of reflections. Approximate mapping methods such as in Stewart (1985) and Stewart (1991) are easily adapted to serve the above purpose and are shown in the following section.

The offset x_B of the reflection point from the well for a P-wave arrival over a homogeneous single-layered earth is given in Stewart (1985) as

$$x_B = \frac{x}{2}\left[\frac{vt_v - 2z}{vt_v - z}\right] \qquad 4.3)$$

where x, v, t_v, z, are the source-receiver offset, constant velocity of the homogeneous single-layered medium, normal incidence time of reflection and depth of the receiver respectively. Although this equation is valid for a single-layered earth, it can be adapted to a multilayered earth simply by substituting the stacking velocity $\bar{v}$ (assumed equal to RMS velocity) in place of the constant velocity v (Gulati, 1998).

The final CDP map of 30 m-offset VSP data is shown in Figure 4.15 b) with a bin size of 1.5 m. Because the 15-m offset VSP data has a considerable offset to yield lateral coverage of 7.5 m, a CDP map (as well as the VSP stack: see section 4.1.4) was also produced for this data (Figure 4.15 *a*). For the 15- and 30-m offset CDP map correlation, a static shift of 4 ms was applied to the 30-m offset CDP map (see Chapter 5 for the interpretation).

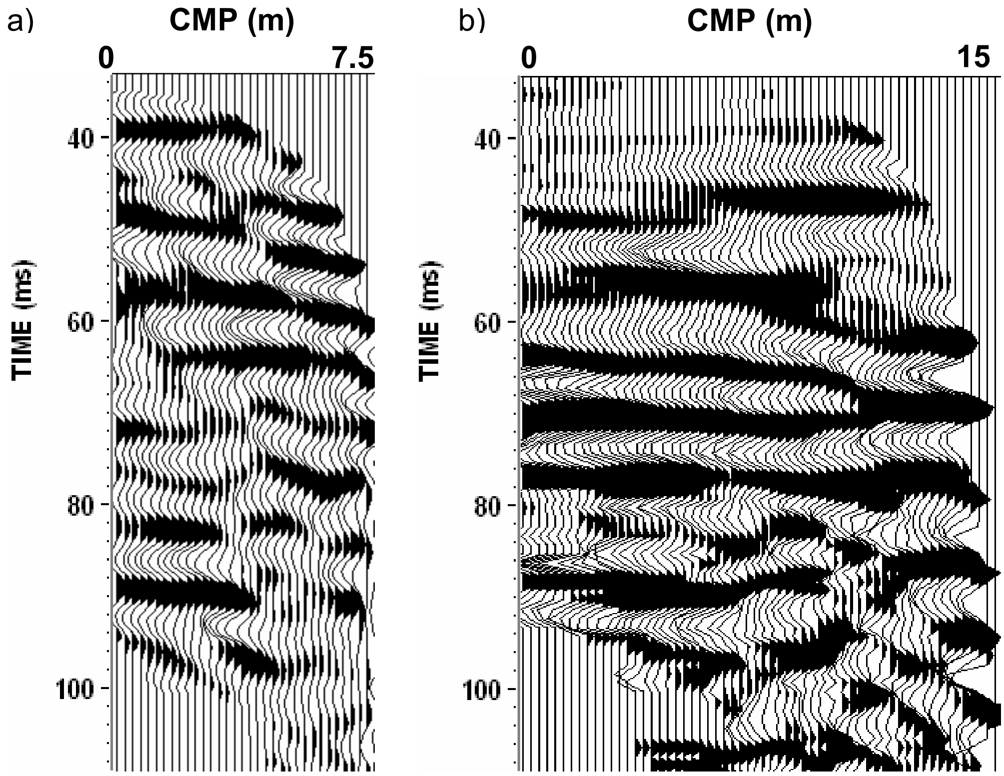

Figure 4.15: VSPCDP maps for a) 15-m offset VSP and b) 30-m offset VSP data.

Chapter 5: Integrative Interpretation

5.1 VSP, synthetic seismogram and well-log correlation

A composite plot of the 15-m offset VSP corridor stack, the synthetic seismogram, and the sonic log is shown in Figure 5.1: The gamma ray and sonic logs are in depth (10-90 m) as is the horizontal scale of the VSP. The VSP however, is also in two-way time on the vertical axis. This allows a direct correlation of surface seismic data as well as synthetic data to the well logs in depth (Stewart, 2001).

The previously outlined porous zones, I to IV, at depths 28 m, 39 m, 50 m and 60 m are identified in the synthetic and the 15-m offset VSP near the respective two-way traveltimes of 48 ms, 57 ms, 63 ms and 72 ms. In addition, strong reflections are observed for the shallow fracture at 18 m (or 38 ms, marked as F) and the possible water inflow zone at 80 m (or 83 ms, marked as IV') within the thick sandstone zone, IV.

The dotted lines on the composite plot indicate correlations between sonic-log character and seismic signatures. The top of sandstone units (*i.e.* zone II-IV) is revealed as an increase in velocity on the sonic log (as well as density), resulting in a positive reflection coefficient. The corresponding event on the 15-m offset VSP is a peak. On the other hand, zone I lies on the sandstone to shale boundary. This event shows a decrease in velocity on the sonic log, thus resulting in a negative reflection coefficient. The same event is identified as a trough on the 15-m offset VSP.

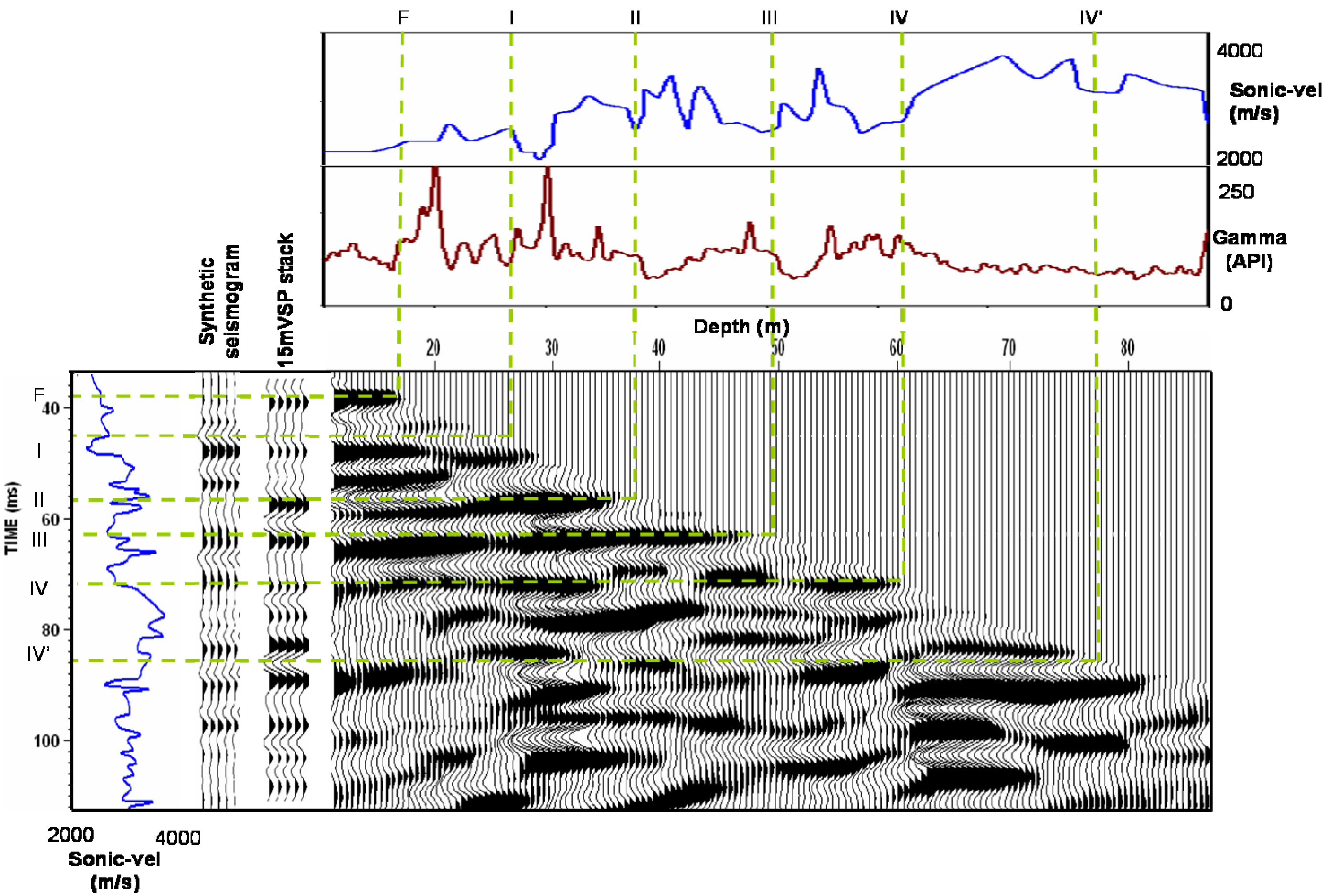

Figure 5.1: Integrated composite L-plot display plotted in two-way traveltimes. From left to right: Calibrated sonic-velocity; synthetic seismogram; deconvolved corridor stack of 15-m offset VSP; NMO-corrected upgoing primary wavefields of 15-m VSP data with sonic and gamma-ray logs in depth on top panels. The zones of interest (I-IV) and a shallow fracture are indicated by the dotted green lines.

Figure 5.2 shows correlation of 15-m offset VSP corridor stack, 15- and 30-m offset CDP maps. As explained in section 4.2.5, the CDP maps are produced to investigate whether there are laterally dipping structures or anomalies near the test well. The position of the reflectors imaged on the two CDP maps match reasonably well (see Figure 5.2 b) with, and show reasonable continuity along, the north-to-south oriented horizontal distance.

The zones of interest, the fracture at depth of 18 m (F), zones I to IV, and IV' are indicated in both the 15- and 30-m offset CDP maps. These reflectors are mostly flattened after the NMO correction, but there are still a few southerly dipping structures displayed in the two CDP maps even after the NMO correction: These dipping reflectors at two-way traveltimes of 58 ms and 64 ms correspond to the reflections from zone II and zone III. These two zones represent the cleanest sandstone units within the depths of the test well that shared almost identical well log signatures in resistivity, gamma, neutron-porosity, and sonic logs (see section 3.5.1).

The discrepancies that are observed between the synthetic seismogram, 15- and 30-m offset CDP maps can be anticipated because of their differences in geometry, trace signal-to-noise ratios and instrument timing errors (Gochioco, 1998).

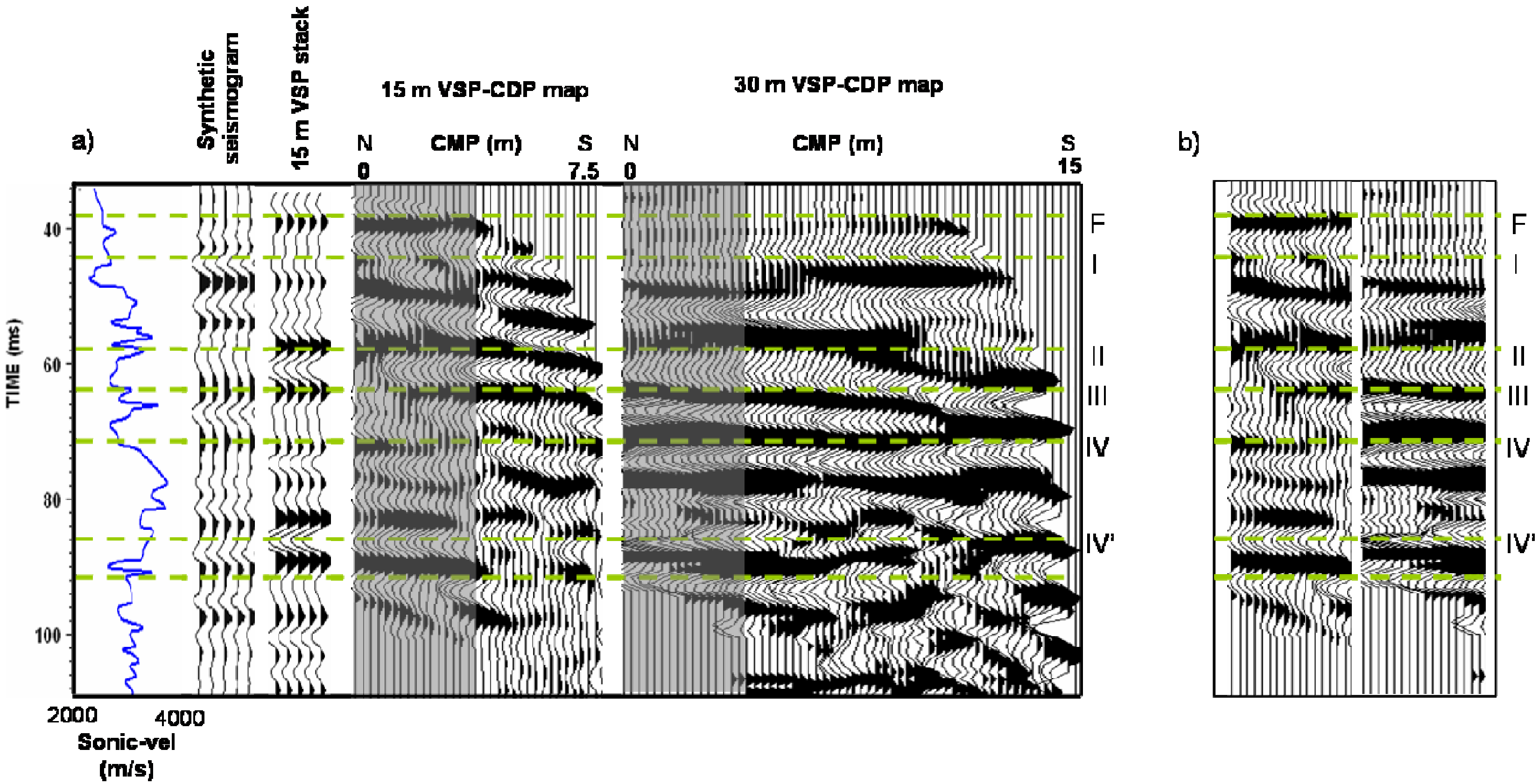

Figure 5.2: a) VSP integrated interpretive display. From left to right: Calibrated sonic-velocity; synthetic seismogram; corridor stack of 15-m offset VSP and CDP maps of 15- and 30-m offset VSP data; b) correlation of the 15- and 30-m offset VDP CDP maps within 3.5 m of the test well (side-by-side correlation of the shaded area in Figure 5.2a).

The corridor stacks of 1.5 m and 15 m VSP data are compared in Figure 5.3. The position and seismic signature of the major reflectors do not correlate very well. Since the 1.5 m and 15 m VSP data were acquired with a seven month time gap, seasonal variations in near-surface soil and moisture conditions may have caused the changes in the seismic signature characteristics (Jefferson et al., 1998). But the poor correlation of the two corridor stacks are more likely due to the poor quality of the 1.5-m offset VSP, which was acquired using the 7.5 kg sledgehammer as the seismic source. The 15-m offset VSP was acquired using a vibroseis unit as the seismic source and the information obtained from this data is expected to be more reliable.

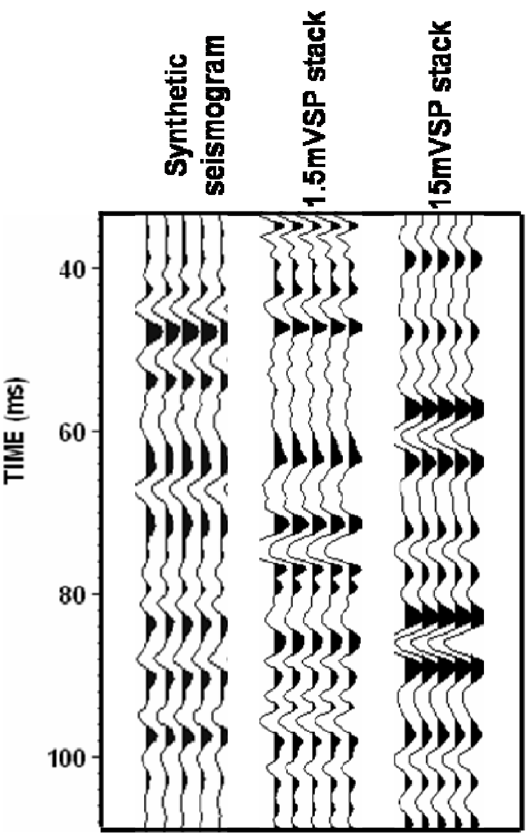

Figure 5.3: Comparison of the 1.5-m offset VSP (acquired with 7.5 kg sledgehammer source) and the 15-m offset VSP (acquired with vibroseis source).

5.2 VSP and surface seismic correlation

In addition to the VSP surveys, near-surface seismic refraction and reflection surveys were acquired near Priddis, Alberta. The Priddis survey was completed in two parts. The first part was undertaken during the 2007 University of Calgary's geoscience field school and included well logging (open-hole and cased-hole), 1.5-m offset VSP, high-resolution 2D seismic refraction and a 3D seismic survey (Figure 5.4). The second part was completed in March 2008, and included a multi-component 2D line, and 15-m and 30-m offset VSP surveys.

Data from the refraction survey was used for surface-wave analysis to estimate S-wave velocity in the area. The 2D and 3D surface seismic and VSP datasets were processed to obtain stacked sections, which are then correlated together.

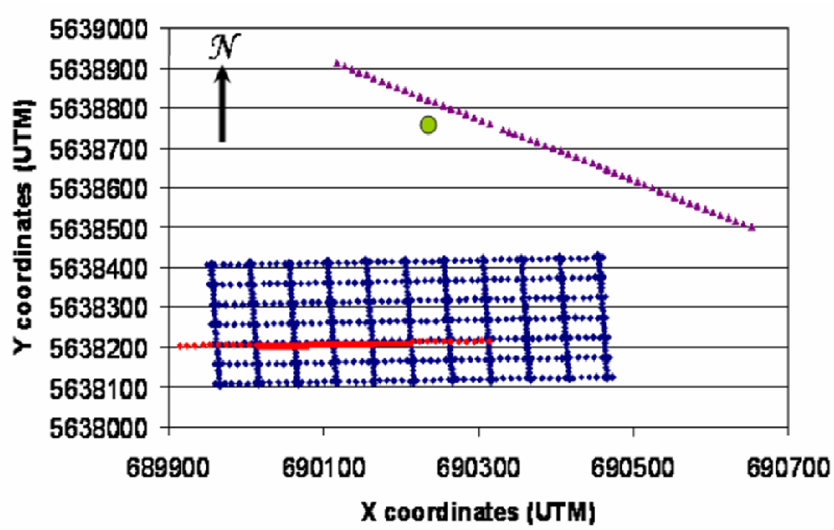

Figure 5.4: Location of the test well (green circle) and various surface seismic survey configurations at the Priddis site: Conventional 2D (red line), 3D (blue grid) and 2D refraction (purple triangles).

5.2.1 Seismic refraction analysis

A northwest-southeast oriented seismic refraction survey with a profile length of 403 m took place near the test well. Surface-wave analysis in the Priddis site involved recording Rayleigh waves on vertical-component geophones, estimating phase-velocity dispersion curves for Rayleigh waves, and inverting these dispersion curves to estimate S-wave velocity as a function of depth (Xia et al., 1999). The 2D refraction profile consisted of a fixed array with a 180-m spread and 72 receivers. The receiver and source spacing were 2.5 m and 12.5 m, respectively. The source used for this 2D seismic line was a five-pound sledgehammer. The record length was 600 ms with 0.125 ms sampling rate (Al Dulaijan and Stewart, 2007).

Figure 5.5 shows the P-wave velocity model obtained from the 15-m offset VSP data and gamma ray log overlain on top of the S-wave velocity profile obtained from the dispersion curve inversion (Al Dulaijan and Stewart, 2007). The general increase in P-wave velocity up to a depth of 36 m agrees with the gradual increase in the S-wave velocity profile. The high velocity arising from the clean sandstone unit (*i.e.* zone II, see Figure 3.9) at depths ranging from 36 m to 42 m is shown on both the P- and S-wave velocity models.

The S-wave velocity profile suggests that the sand-to-shale transitional boundary at 18 m is relatively flat around the test well. This flat structure is also resolved by the VSPCDP maps in Figure 5.2 at a two-way traveltime of 38 ms. The S-wave velocity profile shows lateral velocity variation occurring near the test well at depths greater than 30 m. These heterogeneous structures at greater depths correlates with the southerly dipping structures at two-way traveltimes of 58 ms and 64 ms as shown in the two field VSPCDP maps (Figure 5.2).

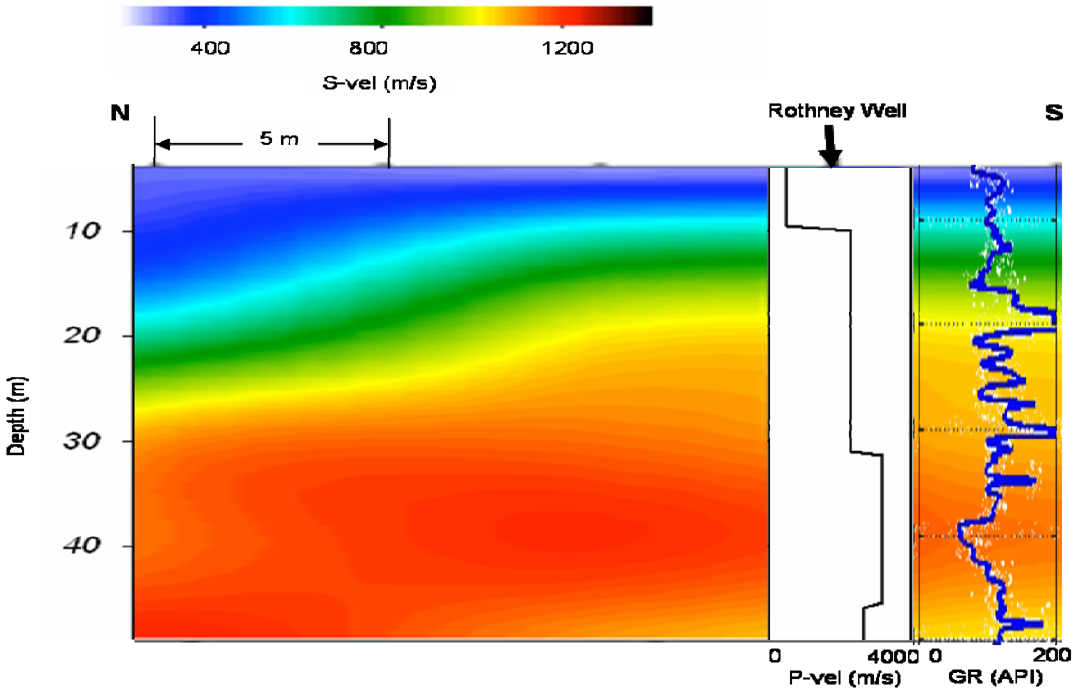

Figure 5.5. S-wave velocity profile obtained from seismic refraction at Priddis (Al Dulaijan and Stewart, 2007) and P-wave velocity obtained from the 15-m offset VSP data. Gamma ray log (blue curve) is also plotted to indicate lithology variation.

5.2.2 3D high-resolution seismic reflection analysis

A high-resolution 3D seismic survey was undertaken to map shallow stratigraphy (depth range of 100-500 m) near the test well. The survey was 500 m x 300 m in area, with shot and receiver lines in an orthogonal geometry using 50 m line separation (Figure 5.6). Shots and geophones were spaced at 5-m intervals along source and receiver lines, respectively. The surface source used was an 18,000 lb EnviroVibe sweeping over a 10 Hz to 180 Hz range. Crossline profile #20 and inline profile #58 were selected for the correlation with 2D reflection and VSP data.

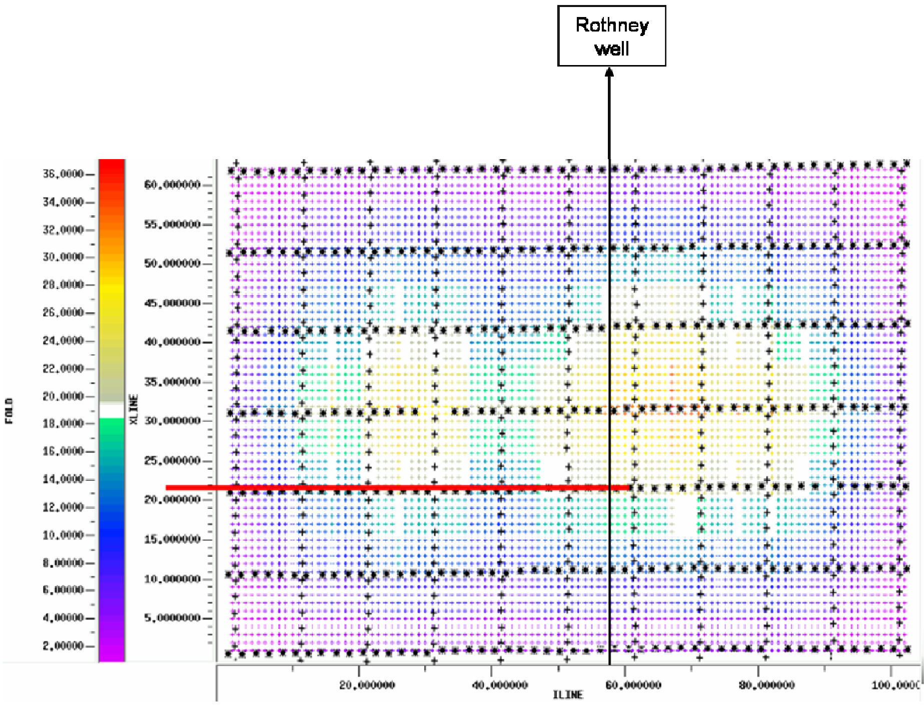

Figure 5.6: Geometry and fold plots for Priddis high-resolution 3D survey. Red line indicates the length and position of the conventional 2D survey (Courtesy of Lu, 2008).

Generally, similar seismic characteristics of major subsurface features are shown in various horizontal (crossline) and transverse (inline) profiles (Figure 5.7 and Figure 5.8). The survey yielded excellent reflections with a dominant frequency of 50 Hz. High-amplitude east-dipping reflections, occurring between two-way traveltimes of 270 ms and 430 ms, were mapped over the survey area (Lawton et al., 2008). The easterly dipping horizon at 270 ms in Figure 5.7 and Figure 5.8 (see yellow lines), is interpreted as the top of the Coalspur Formation (*a.k.a.* Scollard Formation) of Tertiary-Cretaceous age. The lower easterly dipping events at 430 ms (see green lines in Figure 5.7 and Figure 5.8) may correspond to a reflection from Brazeau group in upper Cretaceous time.

The seismic fold for the increasing crossline numbers generally increases away from the test well (Figure 5.6) in this 3D survey. Thus, the amplitude characteristics of the dipping structures as well as some shallow structures (see red lines) are not entirely coherent or consistent from one crossline to another (Figure 5.7). Looking toward the test well in a N-S direction, the inline profiles shown in Figure 5.8 had similar ranges of seismic fold and therefore the major reflections at shallow and greater depths are more coherent from one inline profile to another. The previously interpreted dipping structures are also resolved at the same two-way traveltimes, 270 ms and 430 ms, but looking in N-S direction these structures appear flat.

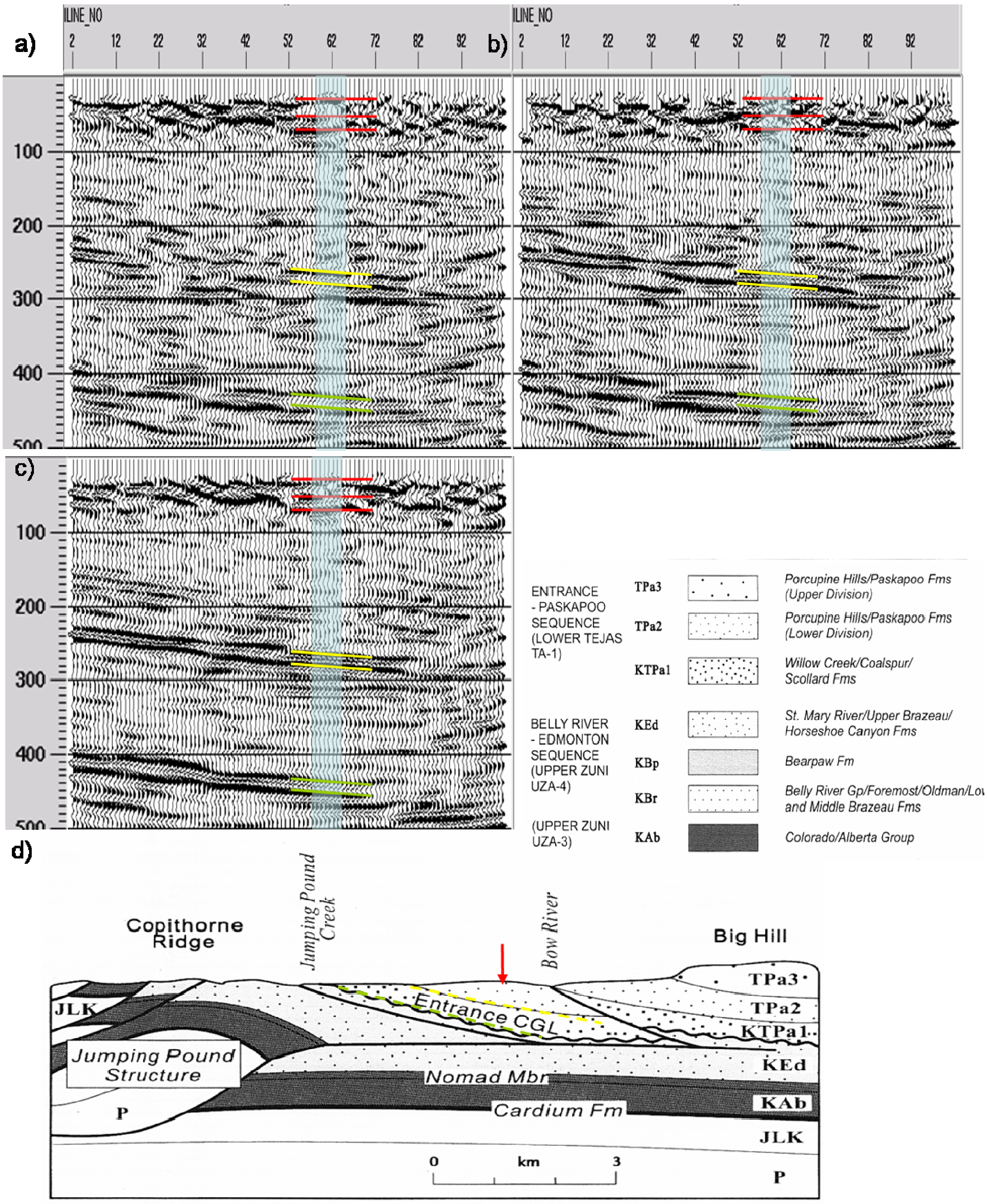

Figure 5.7: Crosslines a) 55, b) 50, c) and 45 with increasing fold (see Figure 5.6), and d) a geological cross-section of the triangle zone (Jerzykiewicz, 1997) near the survey site. The Inline number increases from west to east. The highlighted area in a)-c) represents where the test well is location along the profile. Colour key: red line: major shallow structures within the Paskapoo Formation; Yellow line: Top of the Coalspur Formation; Green line: Top of the Brazeau Group.

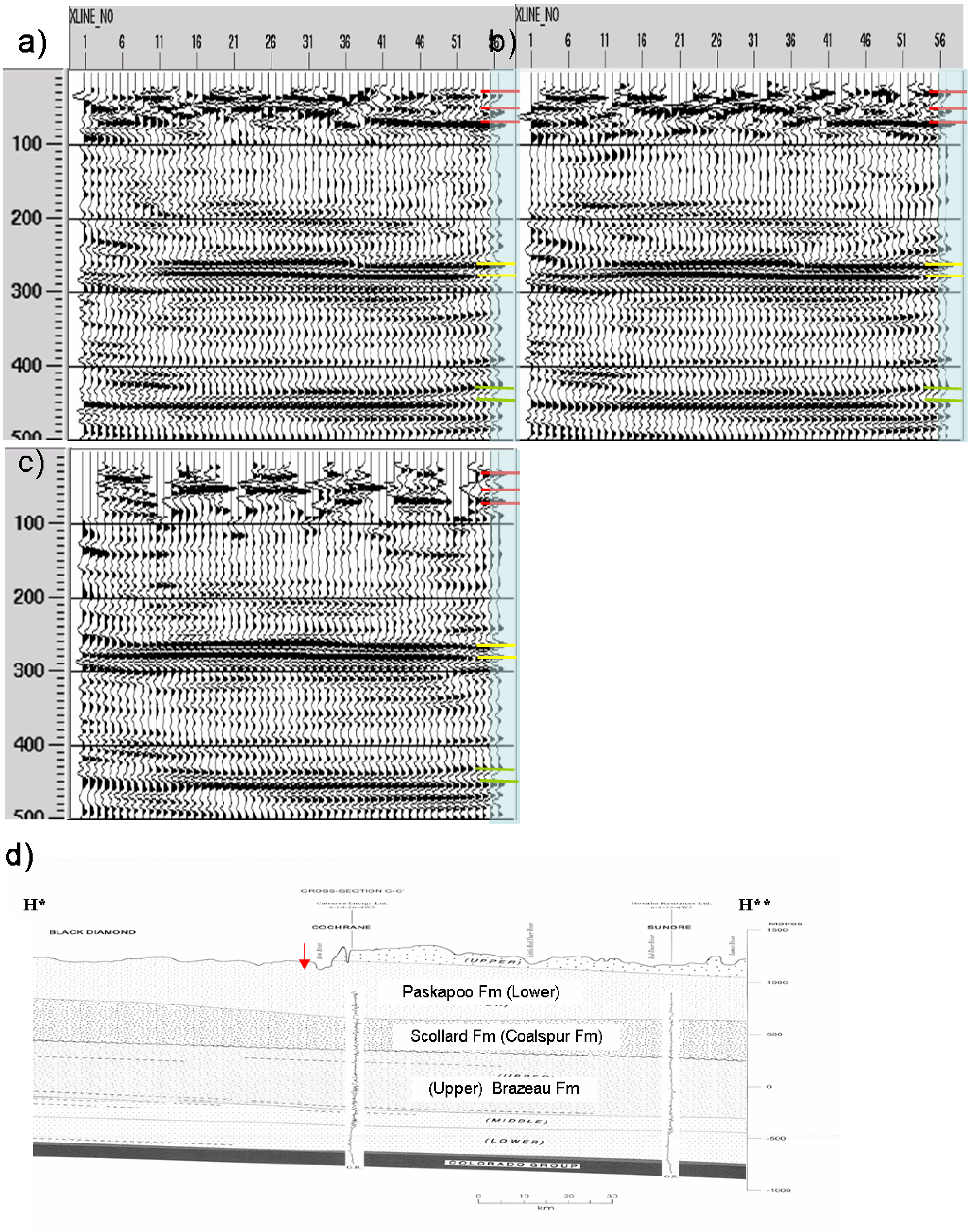

Figure 5.8: Inlines a) 58, b) 60, and c) 62 (see Figure 5.6), and d) a geological cross-section of profile (Jerzykiewicz, 1997) H*-H** in Figure 3.3. The xline number increases from south to north.

Since the offset-VSP data were acquired in a N-S direction, the VSPCDP and VSP stack are correlated with inline profile #58 (Figure 5.9) at the location nearest to the test well (*i.e.* at crossline #57). To match the frequency bandwidth of VSP data with the 3D data, an Ormsby filter with a bandwidth of 10-15-100-110 Hz was applied to the VSP data. Correlating the bandpass-filtered VSP data with the original VSP data, the major reflectors at shallow depths were identified. The red lines in Figure 5.9 represent shallow zones of interest identified previously from the well-logs and VSP stacks (Figure 5.1).

The three major shallow reflectors at times 32 ms, 57 ms, and 72 ms, which are identified in many of the crosslines and inlines (see red lines in Figure 5.7 and Figure 5.8), may correspond to: 1) the boundary between the overburden and bedrock (at depths of <9 m); 2) fracture at 30 m (*i.e.* zone I); and 3) a thick sandstone layer at 60 m (*i.e.* zone IV), respectively. Also the Coalspur Formation at 270 ms correlates quite well between the VSPCDP and 3D data.

The occasional mismatch between the two datasets is expected because the test well and north end of the inline profile #58 is offset by ~300 m. Moreover, the Paskapoo Formation is expected to have very complex stratigraphic characteristics at shallow depths because of systems of sand channels that developed as fluvial deposits (L. Bentley, personal communication). Another reason may be due to the different high cut Ormsby filter applied to the two datasets (*i.e.* 110 Hz and 90 Hz for the VSP and 3D reflection data, respectively).

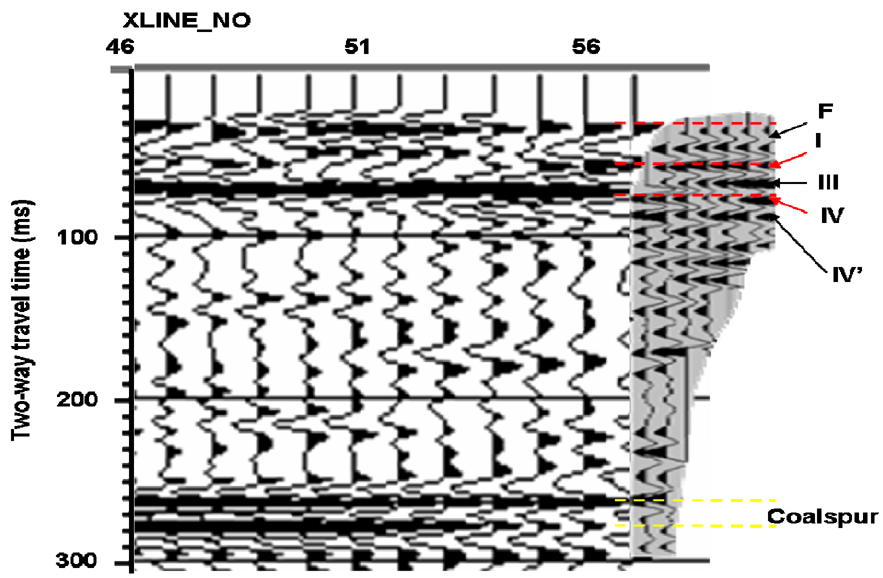

Figure 5.9: Correlation of the VSPCDP map with the Inline #58 3D profile. The x-axis is the crossline (xline) number (with a 5 m interval) and increases from south to north.

5.2.3 2D-3C seismic reflection analysis

The conventional 2D multi-component seismic line consisted of a 200-m planted-geophone line, and a 400 m source line (see red line in Figure 5.6 *a*). Two hundred multi-component planted-geophones were deployed at 1-m intervals. Again, this survey employed an 18,000 lb Envirovibe source with 4 times vertical stack sweeping from 10 to 250 Hz sweep with an 11-second recording time (Suarez et al., 2008).

Comparing the 2D data to the overlapping crossline #20 from the 3D survey, the Coalspur Formation (at 270 ms) is resolved in both datasets (Figure 5.10). Note the constant ~20 ms time delay in the 2D data. However, the 2D data did not image the deeper reflector at 430 ms. The 2D data appears to have imaged the shallow structure better but seems more contaminated with noise. The VSP stack and CDP map were tied to both datasets; although they correlate reasonably well with the 2D data, a better tie is observed with the 3D data. The three shallow structures identified previously are imaged in the 2D data in more-or-less similar positions.

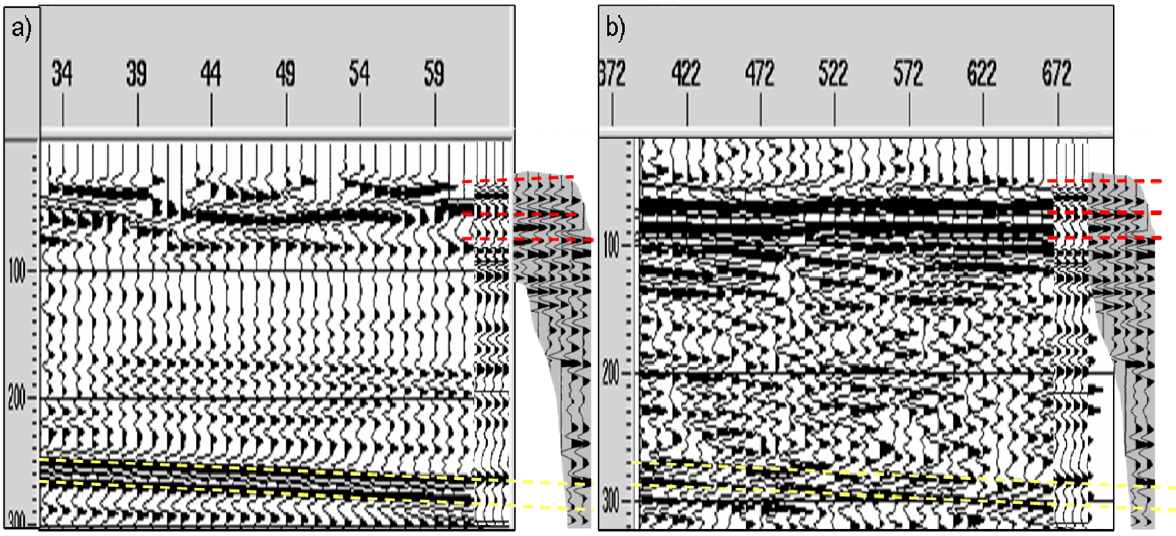

Figure 5.10: Comparison of a) 3D and b) 2D data and their tie to VSP data (15-m offset VSP stack and 30-m offset CDP map). Note that there is ~20 ms time delay in the 2D planted geophone data. These lines overlap one another and are positioned at crossline #20.

5.3 Conclusion

Extensive borehole and surface seismic tests were undertaken near Priddis, Alberta. Well logs, shallow VSP, and 2D and 3D reflection surveys were conducted in the vicinity of the Rothney well (05-13-022-03W5). Analyses of these various datasets provided useful information regarding the near-surface stratigraphy and hydrogeological characteristics of the Paskapoo Formation.

According to the qualitative and quantitative analysis of well logs, a major fracture zone (zone I) and four porous zones (zone II to V) were identified at depths of 28 m, 39 m, 50 m, 61 m and 120 m with porosities ranging from 0.34 to 0.58. Among these zones, there were three water-bearing zones at depths of 28 m, 50 m, 120 m identified by the driller's log description. Another possible water-bearing zone was identified at the thick sandstone unit at 60 m where the temperature log indicated possible downward flowing groundwater. The respective P-wave velocities of clean sandstone and shale zones ranged from 2500-3200 m/s and 1900-2300 m/s after calibrating the P-wave sonic log using the VSP data.

The five zones of interest are imaged in the processed VSP data. Some of these shallow major reflectors imaged in VSP data correlate with various profiles from the 3D and 2D surveys. For example, a major reflection from the zone I, which is a severely fractured zone that is the largest source of groundwater, is imaged at a two-way traveltime of 57 ms (or a depth of 28 m). Further, a possible water-bearing, thick sandstone unit is imaged at 72 ms (or at a depth of 60 m). At greater depths, the easterly dipping base of the Paskapoo Formation or the top of the Coalspur Formation is imaged at 270 ms (an approximate depth of 500 m) by all of the seismic methods implemented in this study.

The collaborative projects demonstrate the efficacy of VSP as well as other seismic reflection survey methods for exploring shallow targets. Applications for these shallow geophysical methods include mapping shallow subsurface features like the distribution of shallow aquifers; delineating coals, and investigating oil sands deposits. Also the shallow velocity information can provide statics information for related seismic processing.

Chapter 6: Conclusions

6.1 Thesis summary

The feasibility of applying VSP techniques for near-surface characterization was tested at two survey sites at the West Castle River area and near Priddis, Alberta. In August 2006, two shallow, multi-offset VSP datasets were acquired in the West Castle River area of southern Alberta. These hydrophone VSP data were rapidly and inexpensively collected. A P-wave velocity model, obtained by simple traveltime inversion, indicated velocities ranging from 670 m/s in the unconsolidated fills to 3500 m/s in the deeper competent shales.

The two velocity models estimated for the Lodge and Duplex wells, which are separated by 200 m, correlate quite well. A synthetic VSP seismogram was generated from the P-wave velocity using the finite-differencing concept. The synthetic seismogram resembled position and character of the major reflections observed from the field data. Also it was used as a guide for interpreting the near-surface hydrophone VSP data. The two-way traveltimes of the seismic reflectors in the VSPCDP stack of the observed VSP data agree reasonably well with positions of the seismic reflector as suggested by the velocity model; especially the tops of three water-bearing gravel layers (32 m, 42 ms and 65 ms in two-way-traveltime) that are resolved by the VSPCDP stack.

With the promising results obtained from the West Castle River area, a more extensive test was carried out in July 2007, near Priddis, Alberta. Well logs, shallow VSP, and 2D and 3D reflection surveys were conducted in the vicinity of the Rothney well (05-13-022-03W5). Analyses of these various datasets provided useful information regarding the near-surface stratigraphy and hydrogeological characteristics of the Paskapoo Formation.

According to the qualitative and quantitative analysis of well logs, a major fracture zone (zone I) and four porous zones (zone II to V) were identified at depths of 28 m, 39 m, 50 m, 61 m and 120 m with porosities ranging from 0.34 to 0.58. Among these zones, there were three water-bearing zones at depths of 28 m, 50 m, 120 m identified by the driller's log description. Another possible water-bearing zone was identified at the thick sandstone unit located at a depth of 60 m where the temperature log indicated possible downward flowing groundwater. The respective P-wave velocities of clean sandstone and shale zones ranged from 2500 m/s-3100 m/s and 1900 m/s-2100 m/s after calibrating the P-wave sonic log using the VSP data.

The five zones of interest are imaged in the VSP result. Some of these shallow major reflectors imaged in the VSP data correlate with various profiles from 3D and 2D surveys. For example, a major reflection from zone I, which is a severely fractured zone that is the largest source of groundwater, is imaged at a two-way traveltime of 57 ms (or a depth of 28 m). Furthermore, a possibly water-bearing thick sandstone unit is imaged at 72 ms (or at a depth of 60 m). At greater depths, the easterly dipping base of the Paskapoo Formation, which might be the top of the Coalspur Formation, is imaged at 270 ms (an approximate depth of 500 m) by all of seismic methods implemented in this study.

The collaborative projects demonstrate the efficacy of VSP as well as other seismic reflection surveys for shallow targets. Applications for these shallow geophysical methods include: mapping shallow subsurface features like the distribution of shallow aquifers; delineating coalbeds, and investigating oil-sand deposits. In addition, the shallow velocity information can provide statics information for related seismic processing.

6.2 Future work

Although the various coherent geophysical datasets may be able to differentiate sand and shale layers, it is extremely difficult to identify water-bearing zones without the aid of various well logs. This is especially true since the Paskapoo Formation is known to have a complex hydrological aquifer system due to the presence of a system of sand channels and fractures. Water saturation depends variously on the inter-connectivity of the sand channels or fractures that potentially provide pathways for groundwater to percolate through (L. Bentley, personal communication, 2008); changes in the water recharge system; precipitation rate; surface temperature changes (drying when hot); and surface vegetation (Majorowicz et al., 2006).

The challenges of imaging more expansive areas can be somewhat overcome by acquiring high-resolution 3D VSP data around the test well. The objective would be to use VSP techniques to image continuities in sand channel or fracture systems and understand them better. VSP data discussed in this thesis can be further migrated to image the dipping structures more accurately.

The interval velocities derived from the first-arrival times picked from the VSP data should be further refined using a more sophisticated traveltime inversion which would take anisotropy or curved rays into account.

Since there could be S- to P-wave conversions occurring at the borehole wall, an elastic-wave modelling algorithm should be used to generate synthetic VSP data rather than the acoustic finite-difference algorithm.

REFERENCES

Al Dulaijan, K. and R.R. Stewart, 2007, Surface-wave analysis for estimating near-surface properties: CREWES Research Report, 19, 12 p.

Agriculture and Agri-Food Canada, 2002, M.D. of Rocky View No. 44; Part of the South Saskatchewan River Basin TP021 to TP029, R25 to R29, W4M & TP023 to TP029, R01to R06, W5M Regional Groundwater Assessment.

Archie, G. E., 1942, The Electrical Resistivity Log as an Aid in Determining Some Reservoir Characteristics: Petroleum Transactions of the AIME, 144-146.

Asquith, G. and D. Krygowski, 2004, Basic Well Log Analysis, second edition: AAPG Methods in Exploration Series, 16, 52-62.

Cardimona, S. J., W.P. Celement, and K. Kadinsky-Cade, 1998, Seismic reflection and ground-penetrating radar imaging of a shallow aquifer: Geophysics, 63, 1310-1317.

Coulombe, C.A., R.R. Stewart, and M.J. Jones, 1996, AVO processing and interpretation of VSP data: Canadian Journal of Exploration Geophysics, 31, 41-62.

Charlesworth, H.A.K., S.T. Johnston, and L.G. Gagnon, 1987, Evolution of the triangle zone in the Rocky Mountain foothills of central Alberta: Can. Journ. Earth Sc., 24, 668-1678.

Dillon, P.B., and R.C. Thomson, 1984, Offset source VSP surveys and their image construction: Geophysical Prospecting, 32, 790-811.

DiSiena, J.P., B.S. Byun, J.E. Fix, and J.E. Gaiser, 1984, F-K analysis and tube wave filtering, in Eds. Tokoz, N.M. and Stewart, R.R., Vertical Seismic Profiling, Part B-Advanced Concepts, Geophys. Press.

Gochioco, L.M., 1998, Shallow VSP work in the U.S. Appalachian coal basin: Geophysics, 63, 795-799.

Goetz, J.F., L. Dupal, J. Bowler, 1979, An investigation into the discrepancies between sonic log and seismic check shot velocities: Austral. Petr. Explor. Assoc., 19, 131-141.

Gordy, P.L., F.R. Frey, and D.K. Norris, 1977, Geological guide for the CSPG and the 1977 Waterton Glacier Park Field Conference: C.S.P.G., Calgary, 93 p.

Grasby, S.E., 2006, Paskapoo Formation – Alberta's most heavily used aquifer: The Fossil Water report, 1; 4, 3 p.

Grasby, S.E., W. Tan, Z. Chen, and A.P. Hamblin, 2007, Paskapoo groundwater study. Part I: Hydrogeological properties of the Paskapoo Formation determined from six continuous cores: Geological Survey of Canada Open File 5392, 9 p.

Gulati, J.S., 1998, Borehole seismic surveying: 3C-3D VSP and land vertical cable analysis: M.Sc. thesis, University of Calgary.

Gulati, J.S., R.R. Stewart, and B.H. Hoffe, 2001, Vertical hydrophone cable acquisition and imaging on land: Geophysics, 66, 1190-1194.

Gulati, J.S., R.R. Stewart, and J.M. Parkin, 2004, Analyzing three-component 3D vertical seismic profiling data: Geophysics, 69, 386-392.

Hamblin, A.P., 2004, Paskapoo-Porcupine Hills formations in western Alberta: synthesis of regional geology and resource potential: Geological Survey of Canada Open File 4679, 31 p.

Hardage , B.A., 1981, An examination of tube wave noise in vertical seismic profiling data: Geophysics, 46, 892-903.

Hardage , B.A., 1992, Crosswell seismology and reverse VSP: Geophysical Press.

Hinds, R., N.L. Anderson, and R. Kuzmiski, 1996, VSP Interpretive Processing: Theory and Practice: Society of Exploration Geophysicists, 283A, 205 p.

Jefferson, R.B., D.W. Steeples, R.A. Black, and T. Carr, 1998, Effects of soil moisture content on shallow-seismic data: Geophysics, 63, 1357-1362.

Jerzykiewicz, T., 1997, Stratigraphic framework of the uppermost Cretaceous to Paleocene strata of the Alberta Basin: Geological Survey of Canada, Bulletin 510, 121 p.

Jones, P.B., 1982, Oil and gas beneath east-dipping underthrust faults in the *A*lberta foothills: in Powers, R.B. (Editor), Geological studies of the Cordilleran thrust belt: Rocky Mountain Association of Geologists Bull, 1, 31-38.

Kappus, M.E., A.J. Harding, and J.A. Orcutt, 1990, A comparison of tau-p transform methods: geophysics, 55, 1202-1215.

Keys, W.S., 1989, Fluid Logging *in* Borehole geophysics applied to ground-water investigations, National Water Well Association, 15, 241-245.

Kim, J.S., W. Moon, G. Lodha, M. Serzu, and N. Soonavvala, 1994, Imaging of reflection seismic energy for mapping shallow fracture zones in crystalline rocks: Geophysics, 59, 753-765.

Lawton, D.C., D.A. Spratt, and J.C. Hopkins, 1994, Asymptotic tectonic wedging beneath the Rocky Mountain Foreland Basin, Geology, 22, 519-522.

Lawton, D.C., R.R. Stewart, and M. Bertram, 2008, 3D seismic surveys for shallow targets: 2008 CSPG CSEG CWLS Convention abstract, 283-286.

Lee, M.W., 1984, Processing of vertical seismic profile data, *in* Simaan, M., Ed., Advances in geophysical data processing: 1, JAI Press Inc., 129-160.

Majorowicz, J., S.E. Grasby, G. Ferguson, J. Safanda, and W. Skinner, 2006, Paleoclimatic reconstructions in western Canada from borehole temperature logs: surface air temperature forcing and groundwater flow: Climate of the past, 2, 10 p.

Manning, P.M. and G.F. Margrave, 2002, The effect of shallow conditions on seismic records, a finite-difference model study: Expanded abstracts for the 2002 SEG conference. pp. 4.

Margrave, G.F., 2007, Methods of Seismic Data Processing. Geophysics 557 Course Lecture Notes, Winter 2007: The CREWES Project, University of Calgary.

McMechan, M.E., 1985, Low-taper triangle-zone geometry: an interpretation for the Rocky Mountain Foothills, Pine Pass - Peace River are, British Columbia, Bull. Can. Petr. Geol., 33, 31-38.

Miller, R.D., D.W. Steeples, and M. Brannan, 1989, Mapping a bedrock surface under dry alluvium with shallow seismic reflections, Geophysics, 54, 1528-1534.

Moran, S.R., 1986, Surficial Geology of the Calgary Urban Area: Terrain Sciences Department, Alberta Research Council, Bulletin No. 53.

Osborn G., and R. Rajewicz, 1998, Urban Geology of Canadian Cities – Urban Geology of Calgary: Geological Association of Canada, Special Paper 42.

Ozoray F.G. and J. Barnes, 1977, Hydrogeology of the Calgary-Golden Area: Alberta Research Council.

Price, R.A., 1986, The southeastern Canadian Cordillera: thrust faulting, tectonic wedging, and delamination of the lithosphere: Jour. Struct. Geol., 8, 239-254.

Sheriff, R.E. and L.P. Geldart, 1995, Exploration Seismology, Second Edition: Cambridge University Press, 277-278.

Stewart, R.R., 1984, VSP interval velocities from travel time inversion: Geophysical Prospecting, 32, 608-628.

Stewart, R.R., 1985, Median filtering: review and a new f/k analogue design: Journal of the Canadian Society of Exploration Geophysics, 21, 54-63.

Stewart, R.R., 1991, Rapid map and inversion of P-SV waves: Geophysics, 56, 859-862.

Stewart, R.R., 2001, VSP: An in-depth seismic understanding: CSEG Recorder, 79, 80-83.

Stewart, R.R., P.D. Huddleston, and T.K. Kan, 1984, Seismic versus sonic velocities: A vertical seismic profiling study: Geophysics, 49, 1153-1168.

Suarez, G.B., S. Miong, J. Wong, R.R. Stewart, A.D. Alcudia, H. Lu, and K. Al Dulaijan, 2008, Well-logging and near-surface seismic methods for aquifer detection, Near Surface 2008 EAGE abstract submission (accepted), 4 p.

Taner, T.M. and F. Koehler, 1969, Velocity spectra-Digital computer derivation and applications of velocity function: Geophysics, 34, 859-881.

Teal, P.R., 1983, The triangle zone at Cabin Creek, Alberta: in Bully, A.W., (Editor), Seismic expression of structural styles: A.A.P.G. Studies in Geology, Series 15, 3, 48-53.

Wong, J., H.C. Bland, K.W. Hall, and R.R. Stewart, 2006, Acquisition and preliminary analysis of the Castle Mountain shallow VSP dataset: CREWES Research Report, 18, 14 p.

Wong, J., S. Miong, L.R. Bentley, R.R. Stewart, 2008, VSP and well logs from a shallow test well, 2008 SAGEEP annual conference abstract, 14 p.

Xia, J., R.D. Miller, and C.B. Park, 1999, Estimation of near-surface shear-wave velocity by inversion of Rayleigh wave: Geophysics, 64, 691-700.

Yilmaz, O., 1987, Seismic data processing. Investigations in Geophysics: 2, Soc. Expl. Geophys.

APPENDIX A: WATER WELL DRILLING REPORTS

a)

Alberta ENVIRONMENT — Water Well Drilling Report

The data contained in this report is supplied by the Driller. The province disclaims responsibility for its accuracy. All information on this report will be retained in a public database.

Well I.D.:
Map verified:
Date report received:

1 Contractor & Well Owner Information

Company Name: [illegible]LLMAN'S WATER WELL DRILLING INC.
Approval No.: 00217500-00-00-17
[illegible]g Address: BOX 345 — City or Town: PINCHER CREEK, AB. — Postal Code: T0K 1W0
[illegible]wner's Name: [illegible]ASTLE MOUNTAIN RESORT — Well Owner has a copy of this report: ☑ Yes ☐ No
Mailing Address: BOX 610 — City or Town: PINCHER CREEK — AB — Postal Code: T0K 1W0

2 Well Location

1/4 or LSD	Sec	Twp	Rge	West of Meridian
NE	24	4	4	5

Location in Quarter: ___ m/ft from ☐ N ☐ S; ___ m/ft from ☐ E ☐ W
Lot / Block / Plan:

3 Drilling Information

Type of Work: ☐ Testhole ☑ New Well ☐ Reconditioned ☐ Deepened ☐ Reclaimed well
Date reclaimed: Yr Mo Day
Materials Used: ☐ Cement ☐ Bentonite Product ☐ Other:
Method of Drilling: ☐ Auger ☑ Rotary ☐ Boring ☐ Combination ☐ Cable tool ☐ Backhoe ☐ Other:
Proposed well use: ☐ Household (up to 1250 m^3 per year with a residence on the property) ☑ Other — Specify: SNOW MAKING

4 Formation Log

☐ metres ☑ feet

Depth from ground level	Lithology Description
0 - 23'	Sand, Gravel
23 - 55	Red Clay, Gravel
55 - 63	Water Bearing Gravel
63 - 69'	Sand Silt
69 - 78'	Gravel Water Bearing
78 - 120	Silt, Sand
120 - 132	Gravel Water Bearing
132 - 140	Red Green Shale

Geophysical Log taken: ☐ Electric ☐ Gamma
Did you encounter: ☐ Mineralized water more than 4000 ppm TDS ☐ Gas
[illegible] depth:
Remedial action taken:

5 Well Completion

Date Started (Yr Mo Day): 05 12 07 — Date Completed (Yr Mo Day): 05 12 08
Are measurements in metric or imperial? imperial
Well Depth: 140 — Borehole diameter: 8
Casing type: Steel — Liner type:
Size OD: 8 5/8 — Size OD:
Wall thickness: .203 — Wall thickness:
Bottom at: 122' — Top: Bottom:
Perforations: from: to: / from: to:
Perforation size: X
Perforated by: ☐ Saw ☐ Machine ☐ Torch ☐ Other:
Seal: ☑ Bentonite product ☐ Cement / Grout ☑ Driven ☐ Other:
Sealed interval: from: 0 to: 122
Screen type: SS — Size OD: 7"
Intervals: from: 117 to: 137 slot size: .030
from: to: slot size:
Installation: ☐ Attached to casing ☑ Telescoped
Fittings: Top ☑ Packer ☐ Coupler — Bottom ☐ Wash-down ☐ Bail ☐ Plug
Pack: ☐ Artificial/Mechanical ☑ Natural
Grain size: — Amount:

6 Well Yield

Test Date (Yr Mo Day): 05 12 08 — Start Time: 1:00 pm
Test method: ☐ Pump ☐ Bailer ☑ Air
Are measurements in metric or imperial? metric
Non pumping static water level: 6.58 m
Rate of water removal: 500 gpm +
Depth of pump intake if pump tested:
Depth bailed or air tested from:
Distance from top of casing to ground level: 3'

Depth to water level

Pumping	Elapsed Time minutes	Recovery
6.58 m	0	140'
	1	
	2	
	3	6.58 m
140'	4	
	5	
	6	
	7	
	8	
	9	
	10	
	12	
	14	
	16	
	20	
	25	
	30	
	35	
	40	
	50	
	60	
	75	
	90	
	105	
	120	

Total Drawdown: 128'
If water removal was less than 2 hr. duration, reason why:
Recommended pumping rate: 300 gpm
Recommended pump intake: 110'
Pump installed ☐ Yes Depth:
Type:
Any further pumptest information? Yes No

7 Contractor Certification

Driller's Name: Sheldon Dillman
Certification No.: 5500 A
This well was constructed in accordance with the *Water (Ministerial) Regulation* of the *Water Act*. All information in this report is true.
Signature: [illegible] — Yr Mo Day: [illegible]

(ENVIR 11/01) — **White copy:** Alberta Environment — **Yellow copy:** Well Owner — **Pink copy:** Contractor b)

ALBERTA ENVIRONMENTAL PROTECTION

COMPUTER GENERATED WATER WELL DRILLER'S REPORT FORM WELL I.D. 339887

THIS DATA MAY NOT BE FULLY CHECKED; THE PROVINCE DISCLAIMS ALL RESPONSIBILITY FOR ITS ACCURACY: Page 1 of 1

CONTRACTOR:

NAME: AARON/INTERPROVINCIAL WATERWELL DRILLING

ADDRESS: Box 28, Site 9, R.R.1 DeWinton, Alberta T0L-0X0

LICENCE NO.: 0892 JOURNEYMAN NO.: VA4996

WELL OWNER:

NAME: DEPT OF GEOLOGY/PHYSICS UOFC

ADDRESS: 2500 UNIVERSITY DR CALGARY

POSTAL CODE: T2N 1N4

WELL LOCATION: IC#:

¼ OR LSD	SEC	TWP	RGE	W. MER
SW	13	022	03	W5

LOCATION VERIFICATION METHOD: FIELD
LOCATION IN QUARTER:

LOT: BLOCK: PLAN:
WELL ELEV: Feet How obtain: SURVEY-AIR

FORMATION LOG DESCRIPTION:

Depth (Feet):	Lithology:
Ground to:	
1	Topsoil
6	Moist Clay
7	Boulders
13	Till & Clay
58	Sandstone
72	Gray Shale
76	Brown Sandstone
78	Gray Shale
93	Sandstone
102	Gray Shale
123	Gray Silty Sandstone
129	Gray Shale
148	Sandstone
152	Gray Shale
164	Sandstone
170	Shale
208	Sandstone
220	Shale
298	Sandstone
300	Shale
307	Sandstone
315	Shale
334	Sandstone
339	Shale
450	Sandstone & Shale Strg's

DRILLING METHOD: ROTARY

TYPE OF WORK: NEW WELL

FLOWING WELL: No **RATE:** L Litres/Min

GAS PRESENT: No OIL PRESENT: No

DATE OF ABANDONMENT:

MATERIAL USED:

PROPOSED USE: MONITORING

WELL COMPLETION DATA:

WELL FINISH: CASING/PERFORATED LINER

TOTAL HOLE DEPTH: 450 Feet

CASING TYPE: STEEL

SIZE OD: 6.62 Inch WALL THICKNESS: 0.188 Inch

BOTTOM AT: 18 Feet

PERFORATED CASING/LINER:

TYPE: PLASTIC

SIZE OD: 4.50 Inch ID: Inch

WALL THICKNESS: 0.250 Inch

TOP AT: 2 Feet BOTTOM AT: 415 Feet

PERFORATED FROM: Feet TO: Feet
Feet TO: Feet
Feet TO: Feet

SIZE OF PERFORATIONS: Inch X Inch

HOW PERFORATED:

SEAL TYPE: CEMENT/GROUT

INTERVAL TOP: Feet TO: 415 Feet

GEOPHYSICAL LOG TAKEN:

RETAINED ON FILE:

SCREEN:

MATERIAL:

SIZE ID (CLEAR): Inch SLOT SIZE: Inch

INTERVAL TOP: Feet TO: Feet
Feet TO: Feet

INSTALLATION METHOD:

TOP FITTINGS:

BOTTOM FITTINGS:

PACK TYPE:

GRAIN SIZE: AMOUNT:

PITLESS ADAPTER TYPE:

DROP PIPE TYPE: LENGTH: Feet
DIAMETER: Inch

ADDITIONAL PUMP INFORMATION:

PRODUCTION TEST:

TEST DATE: August 17, 1907 START TIME: 15:00

Elapsed Time in Min:Sec	Depth to Water Level During Pumping	Depth to Water Level During Recovery

WATER REMOVAL RATE DURING TEST: 20 Gal/Min

TEST DURATION: 2 Hours 0 Minutes

TESTING METHOD: AIR

DEPTH OF PUMP/DRILL STEM: 450 Feet

WATER LEVEL AT END OF TEST: 450 Feet

NON-PUMPING(STATIC) WATER LEVEL: 130.0 FEET

TOTAL DRAWDOWN: 320 Feet

RECOMMENDED PUMPING RATE: Gal/Min

RECOMMENDED PUMP INTAKE AT: Feet

TYPE OF PUMP INSTALLED:

MODEL: H.P.:

DATE WORK STARTED: April 14, 1907

COMMENTS: WELL DRILLED TO 450' OVER NIGHT COLLASPED TO 415' SO WELL WAS COMPLETED AT 415' WATER BEARING ZONES AT 78-93' 170-208' 380-400'
(Maximum of 9 lines printed)

DATE WORK COMPLETED: April 17, 1907

ADDITIONAL TEST AND/OR PUMP DATA:

CHEMISTRIES HELD: DOCUMENTS HELD: 1

WELL OWNER'S ANTICIPATED WATER REQUIREMENTS PER DAY: 500 Gallons

DATE FORM PRINTED: August 21, 2007 12:31:19 **DATE DATA KEYED:** August 21, 2007 GIC5 DC

Figure A.1: Water well drilling report for a) Lodge well in Castle Mountain Ski Resort and b) Rothney well.near Priddis, Alberta.

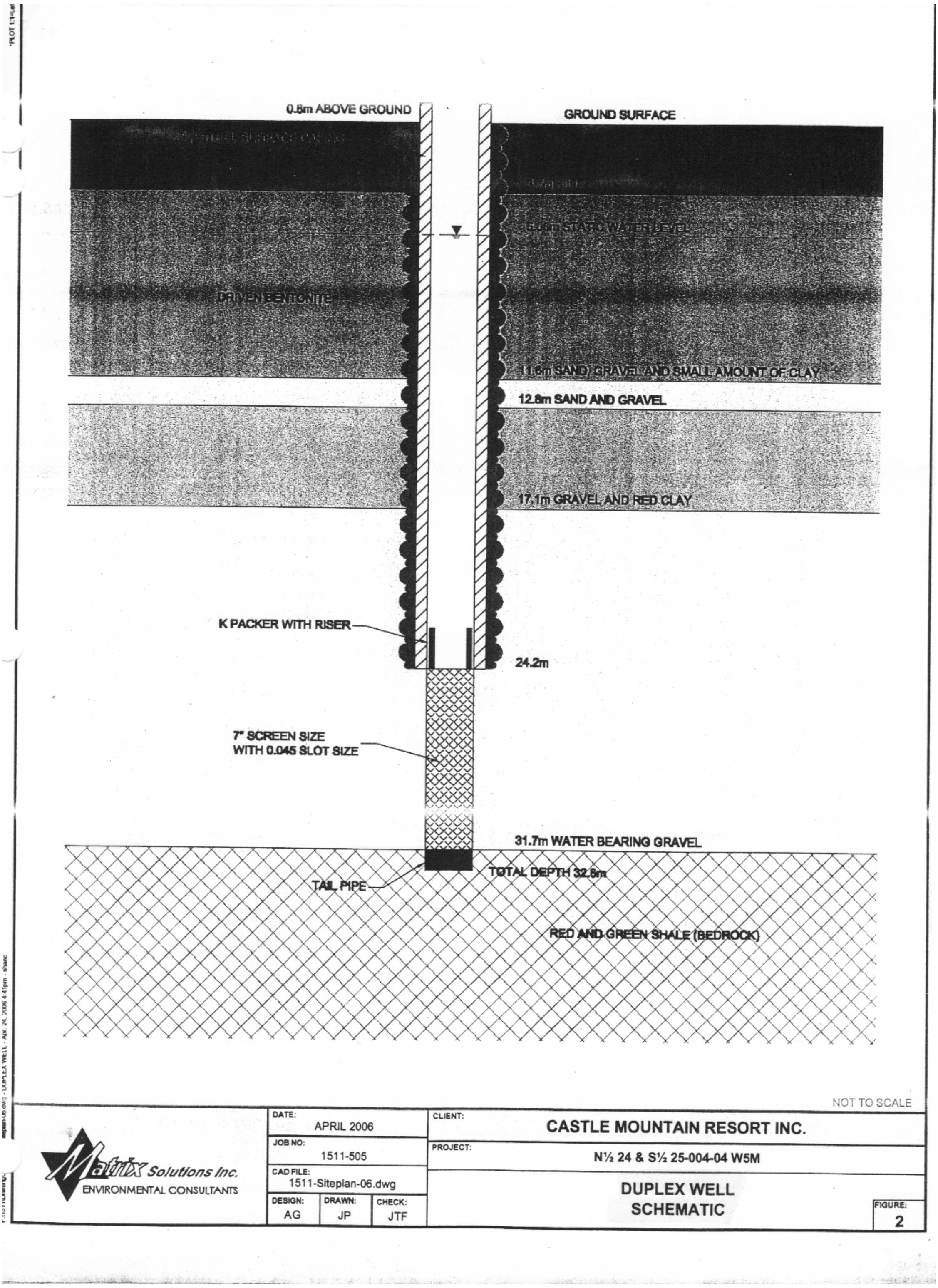

Figure A.2: Schematic drawing of Duplex Well in Castle Mountain Ski Resort.

APPENDIX B: VSP PROCESSING THEORY

B.1. *f-k* filtering

The separation of VSP wave modes by *f-k* filtering is accomplished by transforming the VSP data (recorded in the time-depth domain) to the frequency-wavenumber domain, by forward Fourier transform. It takes advantage of the apparent velocity exhibited by different wave modes and works in the frequency domain, as illustrated in Figure B.1. Excellent overviews of *f-k* domain processing are presented in Yilmaz (1987) and Hardage (1992).

Downgoing VSP modes exhibit positive apparent velocities and the Fourier transform places them in the negative wavenumber half-plane. Conversely, upgoing VSP modes exhibit negative apparent velocities and the Fourier transform places them in the positive wavenumber half-plane. Once the data are transformed into the *f-k* domain, multiplying unwanted wave modes (usually the downgoing waves) by a value that is much less than unity will attenuate the downgoing wavefield and enhance the upgoing wavefield. The transformed data are converted back in the time-space domain by an inverse Fourier transform.

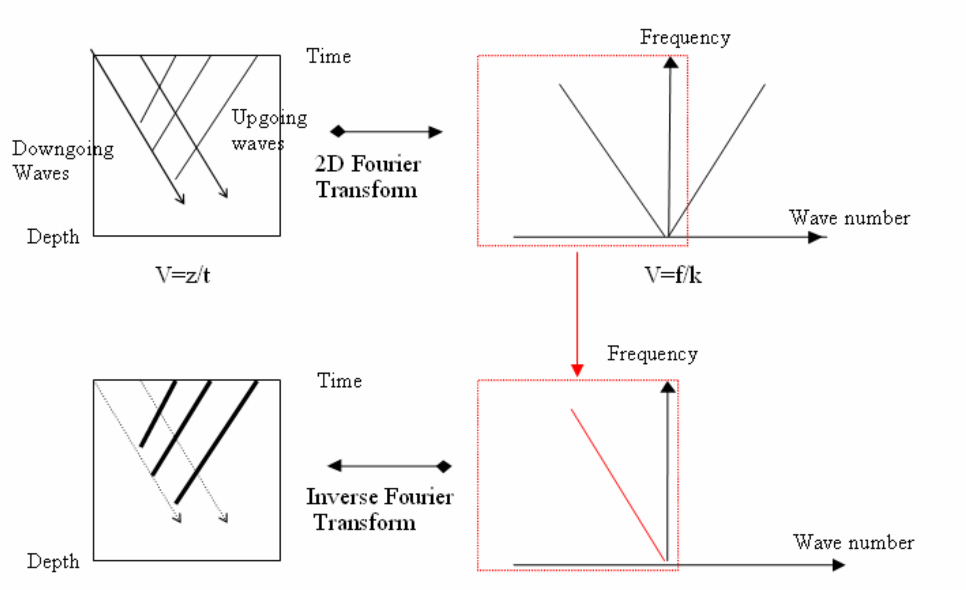

Figure B.1: Principle of wavefield separation by *f-k* filtering.

This separation of VSP wave modes in *f-k* space provides a convenient way by which downgoing events can be attenuated without suppressing upgoing events. However, a feature of Fourier transform pairs is that a narrow function in one Fourier domain transforms into a wide function in the other Fourier domain. Then, when the bandpass becomes narrow, the consequence is a spatial mixing, commonly called Rieber mixing, and it constitutes the main negative aspect of the *f-k* filter (Hinds et al., 1996).

B.2. Median filtering

Median filtering is a signal enhancement technique (Stewart, 1985) that can operate at a constant time (zero moveout) across the dataset. The filter length N refers to the number of consecutive traces over which the filter is applied. At each time sample, the array of N samples is arranged in order of increasing amplitudes (Figure B.2). The median value occupies the (N+1)/2 positions in the array. An N point median filter will generate one output trace by taking this median value from N samples at each time array point. The output trace will be assigned to the position occupied by the centre trace of the filter.

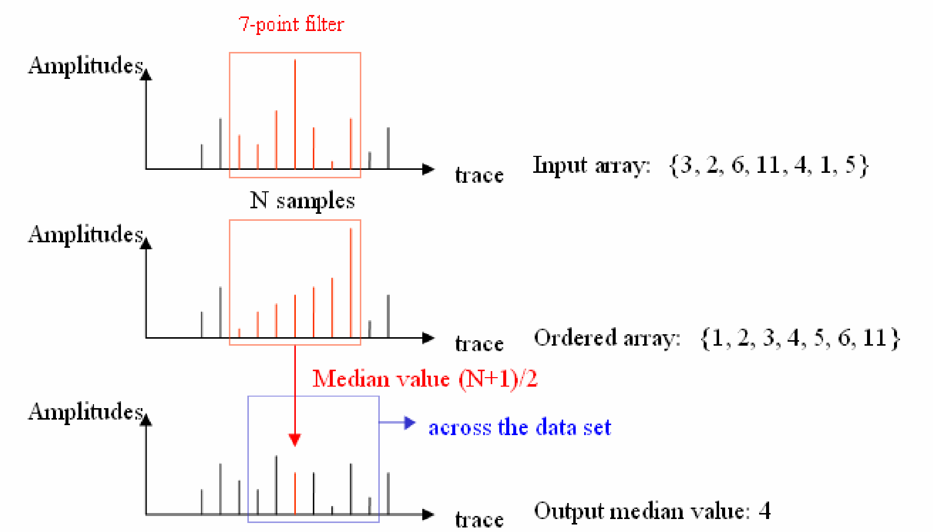

Figure B.2: Principle of median filtering.

The properties that make median filter attractive in VSP data processing are: (1) it rejects noise spikes (because the data are ordered according to amplitudes values, a spike will almost always occupy a position other than the median value, and as such, will be rejected) and (2) it passes step functions without altering them; therefore amplitude of the original data are preserved after filtering. However, abuse of the smoothing property of the median filter may cause reflection events to appear artificially smooth. Hence, the filter length for wavefield separation must be carefully chosen as it is data dependent.

B.3. Principles of corridor stacks

A major reason for producing the corridor stack is to enhance the primary upgoing events (near the first breaks). Upgoing multiples are recorded later in time at sonde locations above the bottom generating interface because of the traveltime delay due to the surface-generated or interbedded multiples. In the NMO-corrected, upgoing wavefield data (plotted in two-way traveltime) (Figure B.3), the multiple of a primary reflection is recorded later in time than the primary event. Therefore, by defining a corridor width (in time) near the first break and stacking them, reflector positions can be estimated with reduced risk of interpreting multiples as major reflectors.

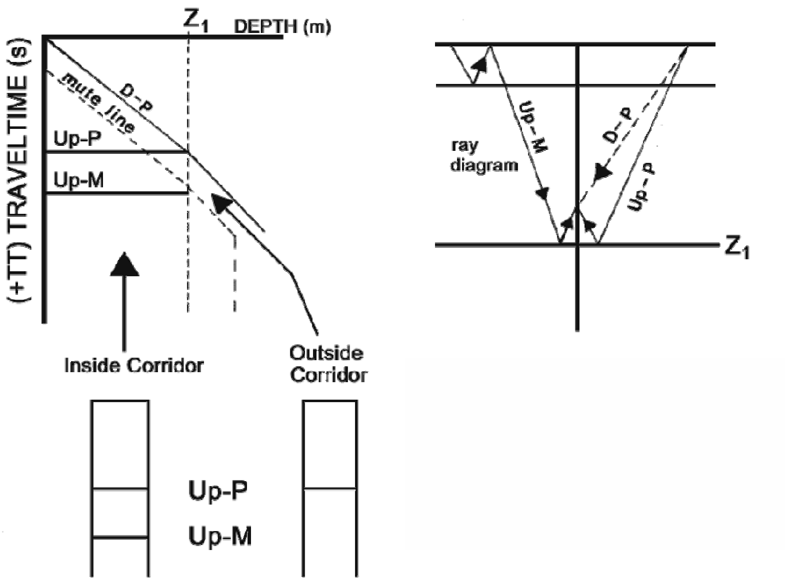

Figure B.3: The schematic definition of the outside and inside corridor stack. The depth versus two-way traveltime plot shows the downgoing primary (D-P), upgoing primary (Up-P), and upgoing multiple (Up-M) events with corresponding raypaths shown in the raypath diagram. Only the primary event (Up-P) is seen in the outside the corridor stack after the summing the events (Hinds and Kuzmuski, 2006).

B.4. Hodogram analysis

An objective of geophone orientation is to isolate upgoing P-waves from the three-component geophone data, X, Y, and Z. There are three geophone rotations necessary to accomplish this objective. The first rotation is of the two horizontal geophones, channels X and Y, to orient one horizontal component toward to source (Hmax) and the other 90 degrees away from it (Hmin): This step is required as the two horizontal channels (X and Y) of the 3C geophone tend to “twirl” within the borehole before they are clamped to the wall. Given the polarization angle (or rotation angle), θ, from the hodogram analysis, the data on horizontal components are converted as follows:

$$Hmax(t)=Y(t)\cos\theta + X\sin\theta \qquad \text{B.1)}$$

$$Hmin(t)=-Y(t)\sin\theta + X\cos\theta \qquad \text{B.2)}$$

Here, θ is the polarization angle, measured clockwise from Y towards X, and (Z, Hmax, Hmin) is the new coordinate system (Figure B.4).

Using the same concept, a second rotation takes place on the plane of the well and source using the previously oriented horizontal data (Hmax) and Z (vertical component). This maximizes the downgoing P-wave energy onto one channel (Hmax') with the downgoing Sv on the other (Z'). The schematic definition of these sensor orientations are shown in Figure B.4. The enhanced P-wave in Hmax' also enables more accurate first-arrival picking.

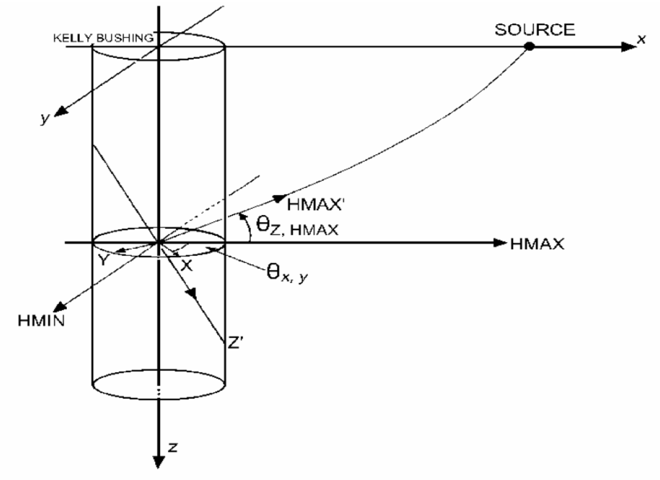

Figure B.4: The schematic definition of time-invariant 3C geophone orientation (Hinds et al., 1996).

The sensor orientations that are introduced so far are time-invariant processes where an incident angle of a ray is assumed to be invariant with increasing depth: Hence, it was assumed that the downgoing P wave is always perpendicular to the upgoing P wave. However, as illustrated in Figure B.5, with increasing shot-offset this assumption is not valid anymore and the change in the polarization angle with time must be accounted for via time-variant rotation: this technique is the third hodogram analysis that is required to complete the sensor orientation.

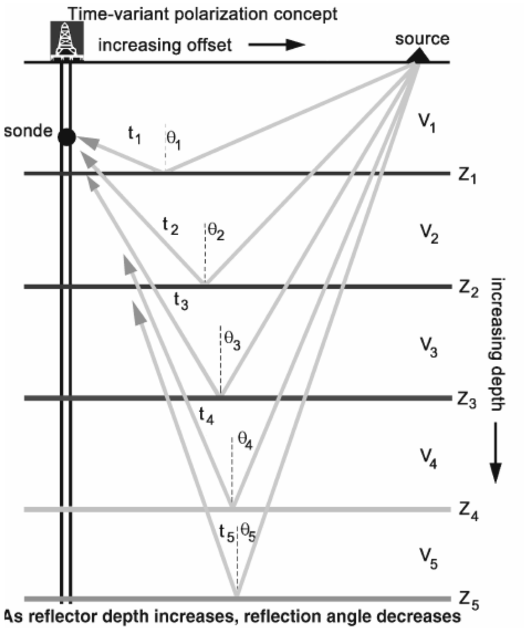

Figure B.5: Schematic drawing of varying polarization angle with increasing offset (Hinds et al., 1996).

B.5. Deconvolution

A primary objective of VSP processing is to enhance primary reflections as the best estimate of reflection coefficients. In VSP processing, the downgoing wave deconvolution is routinely used to enhance the primary reflections and it is used to transform the wavelets from the field data to zero-phase wavelets while suppressing the multiple reflections.

An important assumption of VSP downgoing wave deconvolution is that the waves propagate vertically. This implies a zero offset from the well head, flat layers and a vertical borehole. This technique can also be useful for moderately far-offset VSP deconvolution (Kuzmiski, personal communication, 2008). In this way, the upcoming wavefield equals to the convolution between the downgoing wavefield and the reflectivity series of the earth as follows:

$$U = D * R \qquad \text{B.3)}$$

Here **D** is the downgoing wavefield (Figure B.0.6) composed of the direct arrival and the multiples generated above the receivers; **U** is the upcoming wavefield, composed of the primary reflections and the reflections generated by the downgoing multiples; **R** is the reflectivity response of the earth (Lee, 1984). Only the direct arrival wavelet on the downgoing wavetrain will generate a primary reflection. All subsequent downgoing multiples, constitute redundant information about the reflectors and obstruct primary reflections from deeper reflectors.

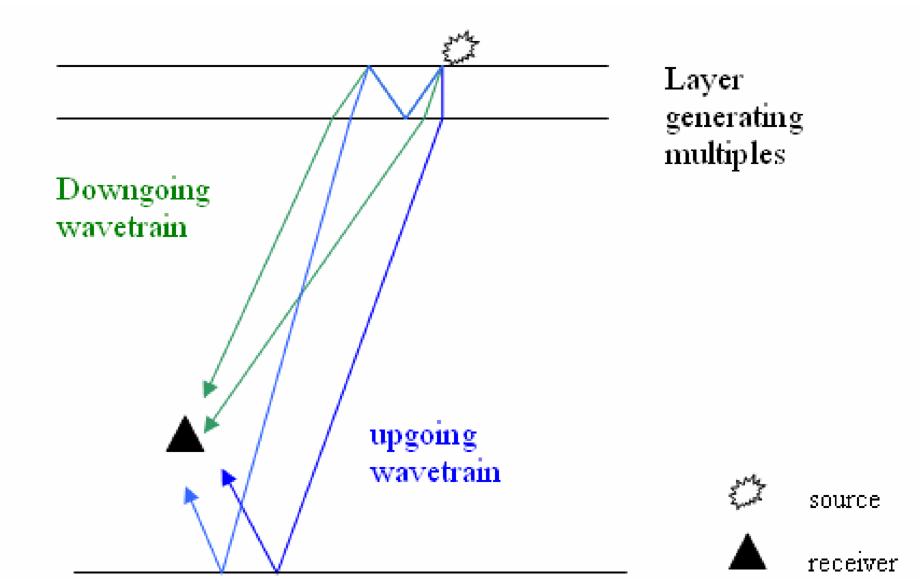

Figure B.0.6: Downgoing and upgoing waves as seen in VSP survey (for clarity of the picture, the zero offset is not represented).

VSP downgoing wave deconvolution is composed of two major steps: (1) inverse operator estimation and (2) upgoing waves deconvolution. An inverse operator is designed from the downgoing wavefield. This operator, called $\mathbf{D}^{-1}$, removes multiples and compresses the downgoing wavetrain to a desired output wavelet (usually a spike called δ) as follows:

$$D * D^{-1} = \delta \qquad B.4)$$

This step is unique to VSP, where the downgoing wavefield (Direct arrival + Multiples) is easily separable from the total wavefield (Hinds and Kuzmuski, 2006). This is in direct contrast to surface seismic data, where surface geophones record only upgoing waves.

This inverse operator, then, is convolved to the upcoming wavefield as

$$R = D^{-1} * U \qquad B.5)$$

where **R** is the deconvolved upcoming wavefield that is removed from the reflections generated by the downgoing multiples.